The Pennsylvania State University

The Graduate School

Department of Chemistry

ADVANCING ToF-SIMS WITH A BUCKMINSTERFULLERENE ION SOURCE

A Thesis in

Chemistry

by

Christopher Wayne Szakal

Submitted in Partial Fulfillment
of the Requirements
for the Degree of

Doctor of Philosophy

December 2006

The thesis of Christopher Wayne Szakal was reviewed and approved* by the following:

Nicholas Winograd
Evan Pugh Professor of Chemistry
Thesis Advisor
Chair of Committee

Andrew G. Ewing
Professor of Chemistry
Professor of Neural and Behavioral Science
J. Lloyd Huck Chair in Natural Sciences

Stephen J. Benkovic
Evan Pugh Professor of Chemistry
Eberly Chair in Chemistry

Carlo G. Pantano
Distinguished Professor of Materials Science and Engineering
Director of the Materials Research Institute

Ayusman Sen
Professor of Chemistry
Head of the Department of Chemistry

*Signatures are on file in the Graduate School

ABSTRACT

The implementation and characterization of a prototype 20 keV C_{60}^{+} ion source from Ionoptika, Ltd. is described. A variety of sample systems, including atomic solids, molecular films, and water ice are examined to elucidate the sputtering and ionization characteristics of this new ion source. Sputter yield increases of two to three orders of magnitude in relation to traditionally employed atomic projectiles are reported. These high sputter yields, along with unique physical properties of the cluster ion sputtering process, are examined in detail. The resulting investigation depicts the C_{60}^{+} projectile as a highly surface-sensitive primary ion that can provide three-dimensional chemical information for a variety of samples. New applications are presented that are in part responsible for a paradigm shift within the Secondary Ion Mass Spectrometry (SIMS) community to a rapidly expanding use of polyatomic primary ions such as C_{60}^{+}.

TABLE OF CONTENTS

LIST OF FIGURES

LIST OF TABLES

ACKNOWLEDGEMENTS

This dissertation would not be possible without the help, support, and/or guidance of the many people that have influenced me throughout my educational career.

I first thank my teachers and professors for imparting their knowledge and for their guidance. At Pittston Area, I especially thank Mrs. Salidas for encouraging me to pursue a career in science instead of instrumental music and Mrs. Roberts for instilling in me a sound fundamental knowledge of chemistry and the persistence needed to fight for my beliefs. At Muhlenberg, I especially thank Dr. Bruce Anderson and Dr. Christine Ingersoll for being inspiring instructors and research advisors, as well as good friends. I also thank my saxophone instructor Tony Simons and band director Al Neumeyer, as their guidance in my musical career have made immeasurable impacts on my life.

In my experiments, I am a large proponent of the "two heads think better than one" philosophy, as long as both people trust each other. At Penn State, I have been extremely fortunate to work directly with people that I trust so that our collective goals can be reached more expeditiously. For their collaboration and friendship, I thank Dr. Andreas Wucher, Dr. Chad Meserole, Dr. Brendan Haynie, Dr. Shixin Sun, Dr. Sara Ostrowski, Dr. Edward Smiley, Joseph Kozole, Anthony Carado, Michael Kurczy, and Melissa Passarelli.

I thank Dr. Barbara Garrison and Dr. Andrew Ewing for their assistance in scientific discussions, but I am even more thankful to them for their help in allowing me to believe that I could attain a post-secondary degree.

I thank my committee members Dr. Andrew Ewing, Dr. Stephen Benkovic, Dr. John Golbeck, and Dr. Carlo Pantano for being helpful in the completion of my goals here at Penn State.

I thank Dr. Nicholas Winograd more than any other in science. I came to work at Penn State because of him and I was allowed to continue studying here because of him. I spent my last three years here trying to make Nick proud, and in the process, he helped me think more globally about science instead of getting trapped within the details. I certainly would not be able to work for anyone else, and I treasure the type of relationship that we have.

I finally thank my family members for their support, especially during the last five years when I needed it most. My parents, Joan and Wayne, and my wife's parents, Deborah and Anthony, have been very encouraging of my endeavors, and helped to convince me that I could indeed obtain a Ph.D. I thank my wife Andrea, whom I love more than anything, for all that she means to me. We have been together for almost a third of our lifetimes, and it is impossible to place into words how she has impacted my life. My career goals only exist so that our life together can be even more special.

Chapter 1

Introduction

1.1 ToF-SIMS Background

Secondary ion mass spectrometry (SIMS) involves the study of ejected material from a surface susbsequent to the impact of a focused energetic primary ion beam. As illustrated in Figure **1-1**, an incident particle sputters material for analysis from a zone of impact close to the surface. The sputtered material generally consists of >98 % neutral species, with the remaining particles being positive and negative ions, and electrons. Since mass spectrometric detection relies on mass analysis of charged species, a femtosecond laser pulse can be directed parallel to the surface so as to intercept the plume of sputtered material. This pulse efficiently ionizes neutral species that are not ionized during the desorption process.

Once secondary ions fly beyond the area just above the target surface, mass separation is accomplished in SIMS with a quadrupole, magnetic sector, or time-of-flight mass analyzer. Typically, magnetic sectors are used for applications requiring the highest mass resolution, as well as for relatively low-mass, inorganic trace analyses. For molecular signals, and applications requiring mass analysis of larger molecular weight materials, time-of-flight (ToF) mass analyzers are utilized. The ability of the ToF analyzer to produce an entire mass spectrum for each ion pulse without scanning is an additional advantage than can be exploited in SIMS instruments.

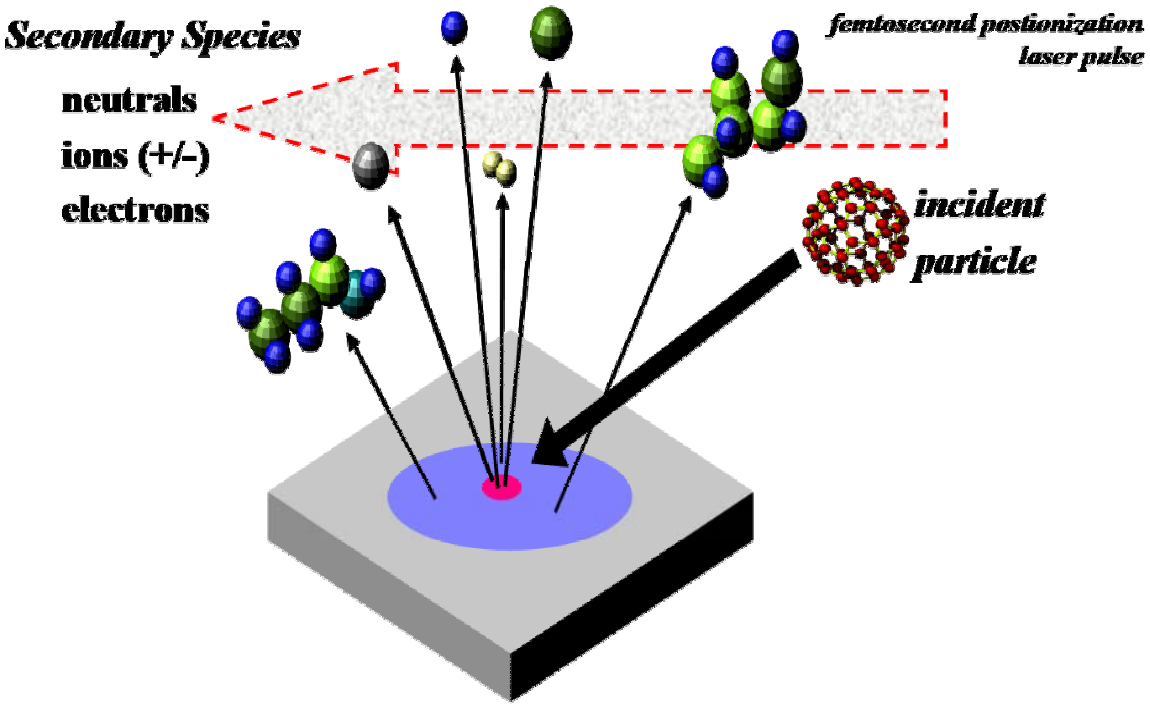

Figure **1-1**: Diagram of typical SIMS event, including a C_{60} incident projectile, the possible secondary species formed, and the orientation of an optional postionization pulse. Figure not drawn to scale. *Note: This diagram is modified from an original version that has been used for lab purposes for several years, and whose original authorship is unknown.*

Historically, the applications of SIMS first emphasized the study of samples related to the semiconductor industry, such as doped atom implants in silicon. Gradually, the use of SIMS in the past couple of decades has extended beyond inorganic surfaces to organic films and small molecule analysis, including biological samples with complex arrays of molecule mixtures. A fundamental limitation in studying molecules in SIMS, however, lies in the use of traditionally employed atomic ion sources. Atomic projectiles such as Ga^+, Cs^+, and In^+ impart a large amount of incident energy into the bulk of the sample – leading to a relatively small amount of desorbed material. The result of this behavior for molecular targets is that many surface and subsurface molecules are

damaged. Since sputtering yields are generally quite low, the damaged molecules accumulate, layers of molecules mix around, and the surface tends to develop topographic roughening. Additionally, bombardment of molecular samples by atomic projectiles often leads to an accumulation of charge at the surface. Theoretically, this charging can build as high as the primary projectile energy, which not only deflects the ion beam and reduces the success of imaging experiments, but hinders the ejection of the ionized species of interest. All of these bombardment-induced developments decrease molecular ion signals further, and often eliminate the original low secondary ion signals. Several experimental adjustments have been made to alleviate some of these drawbacks of atomic projectile bombardment, including reducing the primary projectile energy and utilizing charge compensation systems, but significant sensitivity issues remain.

1.2 Polyatomic (Cluster) Ion Sources

Over the past two decades, several studies have been conducted on the properties of polyatomic projectile bombardment, ranging from simple multiples of inorganic atoms (such as Au_n^+, where n = 1-13),[1-2] to heterogeneous clusters with small total numbers of atoms (such as [Cs_2I^+, $Cs_3I_2^+$] and SF_5^+),[3,4] and large projectiles like [C_{60}^+][5], [Au_{400}^{4+}][6], and glycerol droplets.[7] The collective summaries of the prior work with cluster ion sources include the observations that both inorganic and organic secondary ion signals and yields increase for polyatomic projectiles at rates greater than those from individual atomic ion bombardment. For example, the enhancements observed for Au_n^+ with respect to Au^+ are much greater than nAu^+.[1-2] These deviations from linear cascade

theory are based on several different physical properties that are unique to cluster ion bombardment. The drawbacks of the above sources, however, involve difficulties with integrating the beams into ToF-SIMS instruments, poor focusing abilities, and/or poor source lifetimes.

Buckminsterfullerene is a molecule whose size is especially appropriate for SIMS experiments. Since cluster ions distribute their incident energies among their constituent atoms upon surface impact, each carbon atom carries $^1/_{60}$ of the total energy. This allows the total energy to be deposited into a dense region close to the surface where it is efficiently transferred into sputtering. Additionally, since the impacting energy per molecule is high, the C_{60}^+ molecules can be well-focused.

Ionoptika, Ltd. is the first company to effectively focus and commercially develop a C_{60}^+ source at an incident energy of 10 keV. Preliminary experiments have shown that there are substantial increases in secondary ion yields for organic targets with a probe size in the 10-50 μm range.[8] Although large compared to the sub-μm beam sizes used for atomic projectiles, this source represents a significant step in the recent shift in SIMS to using cluster sources. This thesis work involves the implementation and characterization of a prototype 20 keV C_{60}^+ source, also from Ionoptika, Ltd. The higher energy allows for increased lateral resolution while keeping the energy per atom sufficiently low to benefit from increased yields with little subsurface damage. The radically different physical properties associated with C_{60}^+ bombardment compared to traditionally employed atomic projectiles are examined in detail, and the application of exploiting these properties for SIMS bioimaging is presented.

1.3 Research Overview

In order to conduct experiments that study the physical properties of C_{60}^+ and related applications, it is necessary to understand, operate, and adequately maintain the prototype 20 keV C_{60}^+ ion source properly. In Chapter 2, the implementation and performance characterization of the 20 keV C_{60}^+ ion source (Ionoptika, Ltd.), installed on an existing ToF-SIMS instrument, is described. The ionization region, the primary focusing region, and the final focusing region are described in detail.

Operation of the 20 keV C_{60}^+ ion source requires balance of the intensity of the SIMS signals with source lifetime. A reference-guide approach is used for presenting the nuances of a detailed maintenance regimen, including routine upkeep such as source cleaning, the best methods for source assembly/disassembly, and information on troubleshooting and alleviating difficulties.

In chapter 3, the ion/solid interaction for C_{60}^+ with a polycrystalline Ag target is examined. This system is a valuable model for understanding the new physical properties associated with cluster ion bombardment. The results show that the enhanced secondary ion yields observed for this system are predominantly caused by enhancements of the respective partial sputter yields, (or the number of removed atoms per incident projectile), as measured by quartz crystal microbalance (QCM) experiments. More specifically, the neutral Ag yield is increased about 6-fold under bombardment with 15-kev C_{60}^+ as compared to isoenergetic Ga^+ projectiles. For sputtered neutral Ag_2 and Ag_3, the yield enhancements are even larger, in qualitative agreement with molecular dynamics (MD) calculations.

In chapter 4, the 20 keV C_{60}^+ source is utilized to characterize three additional model systems, all important to present applications of SIMS. These include a Ni:Cr multilayer stack, a relatively thin film of poly(methyl methacrylate) (PMMA), and frozen histamine in water ice. Controllable sputter-erosion of the three sample systems introduces the notion that C_{60}^+ can be used for SIMS depth profiling experiments. Specifically, prolonged C_{60}^+ bombardment is not found to create significant molecular damage accumulation, interlayer mixing, or topographic roughening. Depth resolution of several nm is achieved, which is comparable to the best depth resolution possible with low-energy atomic projectiles for inorganic multilayer samples. Additionally, the C_{60}^+ projectile offers the additional benefit of a well-focused beam for imaging applications while sputter-eroding. These data show that the new physical properties of the cluster source sputtering process can lead to new applications for SIMS, including the ability to create a three-dimensional chemical map of species in a biological material.

In chapter 5, the issue of ionization in cluster ion SIMS is examined using frozen samples of group I salts. This model allows for the study of the relation of ionic charge, size, and concentration to the emission of secondary ions. The results show that significantly more cations than anions are observed in the spectra for low initial concentration of ions. Molecular dynamics calculations show that anions do not disrupt the hydrogen bond network in water, leaving them trapped inside the matrix. The cations, on the other hand, establish a preformed complex that breaks down the hydrogen-bonded network, allowing clusters of solvated ions to eject more easily. The concept that ions (or other species) can destabilize the original matrix and thus alter the ejection properties in SIMS experiments is new and has potential general applicability to

other matrices besides water ice. In addition, it is shown that SIMS spectral intensities are not proportional to salt concentration, due to cation-anion recombination events that form undetected neutral species.

Understanding the physical properties of cluster ion bombardment is essential to determining which SIMS applications can benefit from ion sources such as C_{60}^+. The early data suggest an interesting dichotomy exists between the degree of surface damage/interlayer mixing and the depth of primary energy deposition. Specifically, C_{60} penetrates 3-4x less than an isoenergetic projectile such as Ga into hard inorganic solids such as Ag, but ejects material from more layers beneath the surface.[9] To elucidate the basis for this apparently contradictory behavior, a model system of water ice on Ag is chosen to systematically study the sputtering properties of several different projectiles and is discussed in chapter 6. The water ice system is used because it has a low cohesive energy comparable to many molecular solids of practical interest in SIMS, and is the matrix within and surrounding targeted biological cells in bioimaging experiments.

The results show that C_{60}^+ deposits considerably more incident energy closest to the surface than any of the other projectiles studied. This efficient deposition of energy within a dense region beneath the surface leads to removal of material from just the top few layers, but also removal of the most material. The result is a highly surface-sensitive projectile that provides maximum sputtering yields while significantly reducing sub-surface damage accumulation. The key to a successful depth profile is to have the total sputtering yield much greater than the residual damage accumulation (i.e., sputtering away damage as fast as it is created). Therefore, these data help to solidify the

understanding of the physical properties responsible for the observed ability of C_{60}^+ to depth profile through a variety of sample systems.

Finally, the application of C_{60}^+ to bioimaging experiments is explored in a preliminary fashion in chapter 7. Two different types of systems are examined: lipid films in picoliter-volume vials, and individual freeze-dried *Tetrahymena* and *Spirostomum* cells. In each case, strong enhancements are observed in the secondary ion signals, resulting in improved lateral resolution in comparison to that following bombardment by In^+ and Au^+. Although the images are greatly improved, expected signals from other molecules within the cells are still not observed, making it necessary for further work to be conducted in this area.

1.4 Conclusions

This thesis work has focused on the study of the physical properties and related applications of a newly implemented 20 keV C_{60}^+ ion source. The examination of a variety of inorganic and organic materials and model systems has elucidated several physical properties associated with C_{60}^+ bombardment and has identified how these findings impact the field of SIMS. Preliminary depth profile imaging of single biological cells with C_{60}^+ has laid the groundwork for future studies and is representative of how this thesis work has contributed to expanding the scope of SIMS studies.

1.5 References

1. Andersen, H.H., Brunelle, A., Della-Negra, S., Depauw, J., Jacquet, D., and Le Beyec, Y., *Phys. Rev. Lett.*, **1998**, *80*, 5433.

2. Bouneau, S., Brunelle, A., Della-Negra, S., Depauw, J., Jacquet, D., Le Beyec, Y., Pautrat, M., Fallavier, M., Poizat, J.C., Andersen, H.H., *Phys. Rev. B*, **2002**, *65*, 144106.

3. Blain, M.G., Della-Negra, S., Joret, H., Le Beyec, Y., Schweikert, E.A., *Phys. Rev. Lett.*, **1989**, *63*, 1625.

4. Gillen, G., Roberson, S., *Rapid Commun. Mass Spectrom.*, **1998**, *12*, 1303.

5. Diehnelt, C.W., Van Stipdonk, M.J., Schweikert, E.A., *Phys. Rev. A*, **1999**, *59*, 4470.

6. Novikov, A., Caroff, M., Della-Negra, S., Depauw, J., Fallavier, M., Le Beyec, Y., Pautrat, M., Schultz, J.A., Tempez, A., Woods, A.S., *Rapid Commun. Mass Spectrom.*, **2005**, *19*, 1851.

7. Cornett, D., Lee, T., Mahoney, J., *Rapid Commun. Mass Spectrom*., **1994**, 8, 996.

8. Weibel, D., Wong, S., Lockyer, N., Blenkinsopp, P., Hill, R., Vickerman, J.C., *Anal. Chem.*, **2003**, *75*, 1754.

9. Postawa, Z., Czerwinski, B., Szewczyk, M., Smiley, E.J., Winograd, N., Garrison, B.J., *J. Phys. Chem. B*, **2004**, *108*, 7831.

Chapter 2

Implementation of a 20 keV Buckminsterfullerene Ion Source

2.1 Introduction

The 20 keV C_{60}^+ source from Ionoptika, Ltd. is essential to the experiments conducted in this thesis. Upkeep of an ion source in SIMS is critical to having a successful research program. Having arrived as a prototype source, the operational details, troubleshooting, and maintenance procedures have developed over time. The operational principles of the carbon cluster ion source are described in detail in this chapter. Optimum operational procedures are outlined to ensure that a balance is present for the quality of SIMS data and the lifetime of the ion source components. Several years of expertise are integrated into the troubleshooting and maintenance sections, including information that is experience-related. The information provided here is designed to leave future experimentalists with the knowledge needed to effectively understand, operate, and service this robust ion source.

2.2 Operational Principles of 20 keV C_{60}^+ Ion Source

The prototype 20 keV C_{60}^+ ion source has three main areas of operation, identified as the ionization region (1), the initial focusing region (2), and the final focusing region (3), as illustrated in Figure **2-1**. The most critical region involves the actual ionization of C_{60}, and a detailed schematic of this area is shown in Figure **2-2**. A standard 24 V Philips halogen bulb, located on the back flange of the source, is centered within the copper holder. The process of applying current though the bulb filament heats the source to 400ºC, and by thermal contact, heats a reservoir of pure C_{60} powder. After thermal equilibrium is reached, a constant vapor of C_{60} forms and exits the reservoir through a small tube, which just touches the entrance to the grid. The vapor

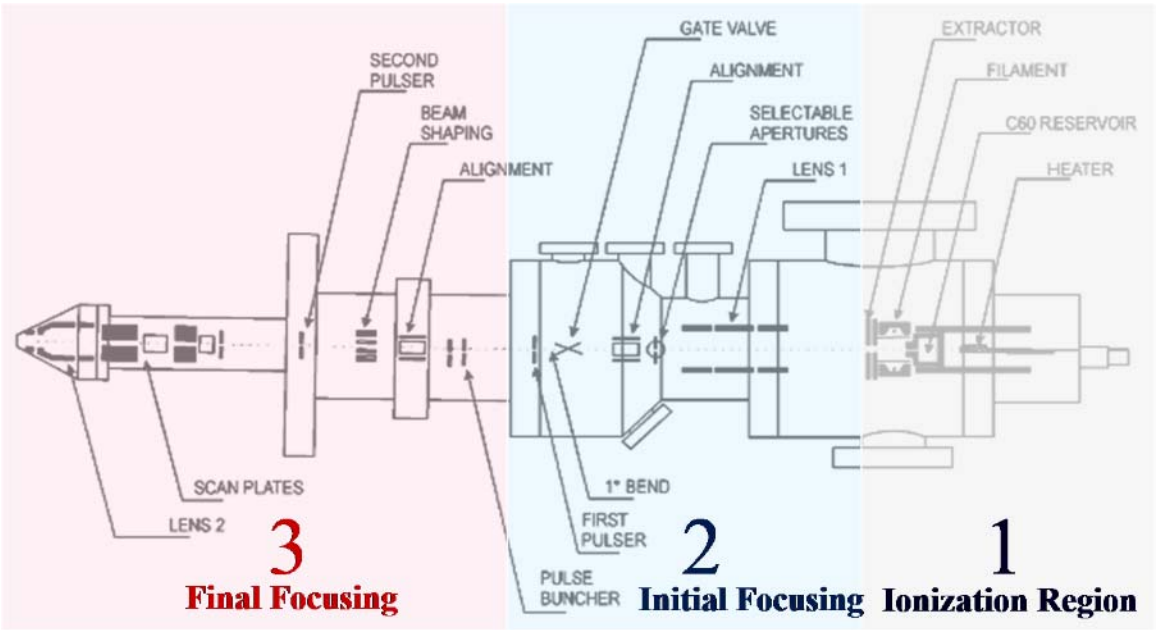

Figure **2-1:** 20 keV C_{60}^+ ion source schematic, modified from the original version provided by Ionoptika, Ltd.

congregates in this region, which is surrounded by a filament and repeller. Current is applied to the filament, which then emits electrons, and these electrons are used to ionize the C_{60} to either C_{60}^{+} or C_{60}^{++}.

The ionized C_{60} is born at a kinetic energy equal to the applied anode voltage, which in this source ranges from 5 to 20 keV. The copper holder, reservoir/exit tube, top grid plate, filament, repeller, and grid are all floated at the anode potential. However, to efficiently ionize the C_{60} vapor, the electrons must strike the carbon cluster molecules with enough bombarding energy to overcome the ionization barriers of C_{60}^{+} and C_{60}^{++}. The ionization barrier for C_{60} » C_{60}^{+} is about 7.6 eV,[1] with the C_{60}^{+} » C_{60}^{++} barrier being about 12 eV.[2] To achieve this potential difference for ionization, the grid is adjusted above the anode potential by up to 120 eV. The larger the voltage, the faster the electrons are attracted to the grid where the difference in energy is imparted to the electron. This relatively low electron energy is used to ionize the C_{60} molecules by means of an electronic excitation in the C_{60} molecule. Since the ions are born within the grid field, the grid energy is the actual kinetic energy that the ions will retain throughout the source column (ex. 20.04 keV). To ensure that the maximum number of electrons formed by the cylindrical filament is used for ionization, the repeller voltage is adjusted below the anode potential by up to 40 eV to direct as many electrons as possible towards the grid.

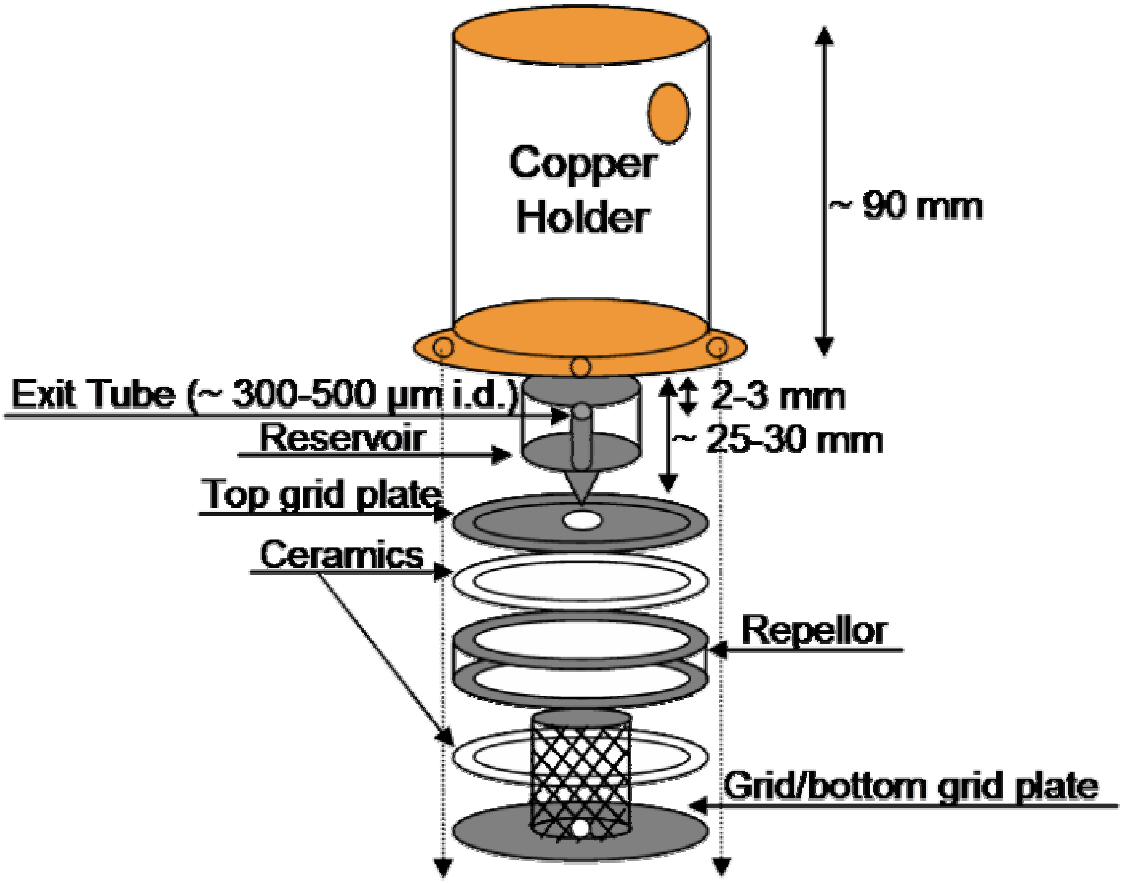

Figure **2-2:** Schematic representation of the ionization region of the 20 keV C_{60}^{+} ion source. Components are approximately drawn to scale, and each component sits flush on the one beneath it.

After exiting the grid, the ionized C_{60} travels through an extractor, which is also floated at the anode potential. A large ceramic insulator separates the extractor electrode with the bottom extract plate, which sits at ground potential. In theory, the extractor electrode potential can be adjusted below the anode potential by up to 2.5 keV to enhance acceleration of the newly formed ions through the column. However, in this source, best performance results from no adjustment to the extractor potential, as the acceleration from 20 keV to ground across the extractor insulator is enough of a driving force to propel the C_{60} ions through the ion column.

The initial focusing region begins at the exit of the bottom extract plate and the entrance of the first electostatic lens (Lens 1). A high voltage, which is anode-dependent, is applied to focus the ions through the selectable apertures. These apertures define beam size by eliminating portions of the beam from passing through, and allowing for subsequent focusing later in the ion column. The general arrangement of the five aperture slots includes 1 mm, 0.3 mm, 0.1 mm, 30 μm, and 10 μm apertures, with the best beam size being achieved with the smallest apertures. However, as a general rule for this source, the final C_{60}^{+} current at the sample drops by a factor of three for each drop in aperture size. If 1 nA is produced using the largest aperture, a maximum of about 10 pA are produced at the sample using the smallest aperture installed.

The Lens 1 focal point exists just beyond a 1º ion column axis bend, which serves as a way of eliminating neutrals from the final ion beam, and at the mid-point of the primary pulser. To adjust this focal point, two sets of plates (x and y orientations) provide low-voltage ion beam steering between Lens 1 and the bend. The pulser system consists of two plates, one of which is permanently at ground, and the other which can be connected via BNC to a pulsing apparatus. If both plates are at ground, both charged and neutral beam particles hit the wall of the column near the axis bend. If a positive potential equal to approximately 1% of the anode potential is applied to one plate, positive particles are steered around the bend to continue down the ion column, with neutrals still hitting the wall. The pulsing process works differently in a liquid metal ion source (LMIS), where there is no axis bend, and one plate always has a voltage equal to 1% of the anode potential. The beam is then constantly deflected off of the central ion column axis until pulsed back to the center by an equal and opposite potential on the

other plate. If no potential is applied to the first plate, the beam travels "unblanked" straight through the source, which explains the potential on the first plate being termed a "blanking voltage".

The final focusing region begins after the primary pulser, and the C_{60} ions travel through a brief flight region before a second set of x and y alignment plates steer the beam. At this point in the source, the beam is spreading into a more collimated shape, as it gradually diverges from the Lens 1 focal point. An octupole can shape the beam after being adjusted with the second set of alignment plates, and the exit of the source consists of a set of x and y raster (scan) plates and the final focusing lens (Lens 2). As shown in Figure **2-1**, the y scan plates are √2 longer than the x scan plates to accommodate for the mounting angle of the ion source. The beam can be deflected a maximum of 1.25 mm in each direction for a maximum raster area of 2.5 mm x 2.5 mm. Lens 2 operates in identical fashion to Lens 1 and has a focal point at the sample, provided that the working distance is between 20 and 25 mm, or preferably 22 mm.

Two optional and seldom-used portions of the source involve bunching and chopping the ion beam. Shortly after the primary pulser, and into the final focusing region of the source, is a pulse buncher, where up to 3 keV can be used to reduce the length of the beam pulse along the column axis. Due to energy dispersions of ± several eV, chromatic aberrations give the beam a Gaussian shape. This broadening can be undesirable for the best mass resolution because primary ions will be hitting at different times and initiating sputtering events at different times. The other optional beam adjustment involves a secondary pulser, termed the "chopper", and located between the octupole beam shaping and the scan plates. A pulse of approximately the same voltage as

that on the primary pulser can be applied to separate the C_{60}^{+} and C_{60}^{++}. Since the doubly charged cluster has effectively twice the kinetic energy but the same mass, it travels at $\sqrt{2}$ of the velocity and can be separated based on flight time through the ion column. If both species are allowed to hit the sample, two sets of overlapping spectra can appear, with identically sputtered species separated in the spectra by the flight time difference of the two carbon cluster species to the sample. Both optional features are seldom used in this lab because we employ a delayed extraction system, whereby ions are not accelerated from the sample until after the primary ions bombard the surface. If the acceleration potential is on before the primary ions arrive, then all sputtered species from both C_{60}^{+} and C_{60}^{++} events are included in the mass spectra. Likewise, if the beam hits the sample without being bunched, the shape of the mass spectral peaks will be directly representative of the primary beam shape, including the broadening that occurs due to chromatic aberrations.

2.3 Operational Details of 20 keV C_{60}^{+} Ion Source

The manner in which the source is operated has a direct effect on the quality of SIMS data and of ion source lifetime. An optimizing procedure each time the source is used ensures that all is working correctly.

2.3.1 Source Heating and Cooling

The proper order of electronic startup involves turning on the ion source controller (generally left on overnight since this controls source temperature), followed by the ion gun controller, and finally the high voltage power supply unit. Failure to use this order may cause long-term circuitry failures. Once all units are on and in standby, the source is heated.

In addition to the source needing to reach an equilibrium temperature for a stable beam current, the ionizing filament also needs heating to generate a steady stream of electrons. If the source is cold, and time permits, the voltage to the bulb (reservoir heater) is placed at 7 V, with a corresponding readout current of about 2.7 A, for about 12 hours. This procedure warms the source to a "standby" state, where it can be heated to operational temperature relatively quickly. In practice, an ion beam can be achieved with the heater as low as 9 V, but is generally unstable as the source isn't quite hot enough to constantly vaporize C_{60}. Initial Ionoptika settings called for 14 V to be applied to the heater, which generates a temperature estimated to be near 500ºC, providing up to 10 nA of C_{60}^{+} ion current. However, this operating mode is ill-advised for the long-term stability of the source, as only a temperature of 400ºC is needed to maintain C_{60} vapor, and constant operation of an overheated source leads to C_{60} coating the insulating ceramics in less than one month. To prevent this premature breakdown of the source, a value of 10 V on the heater, at about 3.4 A, provides a stable maximum beam current of approximately 1 nA of C_{60}^{+}. This current is generally more than adequate for studying

most sample systems, as the high sputter yields give large SIMS secondary ion signals, as will be explained in subsequent chapters.

The transition from standby temperature to operational temperature (7 » 10 V) generally takes 1.5 – 2 hours. Heating the filament to temperature equilibrium occurs more quickly. However, heating to the typical operating filament current of 2-2.2 A is best accomplished in a stepwise manner, and at pace with the heater warming, since that is the limiting step in the warmup procedure. Increasing the filament current by 0.5 A each half hour of the warming procedure ensures that it is at 2 A for approximately 30 minutes by the time the source is hot enough to constantly vaporize C_{60}. Since the electrons are drawn to the positive grid bias, the grid current readout, in mA, displays the current of electrons striking the grid. Generally, a constant grid current at an equilibrium temperature of C_{60} vaporization gives a constant beam current at the sample. The grid current is the primary readout to monitor when constant-current studies are needed. If it drifts to a lower value, then a slight increase of the filament current will return the grid current to a constant value and keep the final beam current constant. If the filament current is at a maximum before/during heating, the grid current will reach a steady value, and then decrease once C_{60} vaporizes and begins ionizing. With the outlined method above, however, this effect will not be observed.

For cooling of the source, and for standby overnight, the heater is returned to 7 V, and the filament current dropped to zero. Once the current is lowered, depressing the filament "heater" button on the ion gun controller disconnects the filament heating circuit from the high voltage. When the high voltage power supply is turned off, and the filament heater is still technically "on", a current spike can run through the filament,

causing premature breakage. Proper order of shutting down the electronics involves first shutting off the high voltage power supply unit. On the ion gun controller, a bleeding of the high voltage can be observed on several of the readouts. After all high voltage readouts return to zero, the ion gun controller can be turned off, and as mentioned earlier, the ion source controller remains on to maintain standby temperature. If maintenance is required, this unit will also be turned off, and the source will need approximately 8 hours to cool enough for disassembly of the ion source column.

2.3.2 Obtaining and Optimizing a Beam

Once temperature equilibrium has been reached, the gate valve can be opened to allow ions to fly through the source column and into the sample analysis chamber. (At least 60 psi of nitrogen gas are needed to open the pressurized gate valve). To obtain a dc ion beam, an external power supply is used to apply a dc voltage equal in amplitude to the pulsing voltage to the primary pulser. Starting with the largest beam aperture, beam current is monitored with a picoammeter at the sample stage by directing the beam into a Faraday cup. The Faraday Cup traps secondary species so that measured current is influenced only by arriving C_{60}^{+} or C_{60}^{++} ions, instead of being influenced by secondary particle emission. Based on several experiments, the Faraday cup embedded within a copper block is about 90 % efficient at trapping secondary species. The net consequence is that the true dc ion beam current is subtracted by 10 % from what is measured in the Faraday cup. The resulting value will be approximately ½ the value of ion current

measured if the beam bombards the copper block surface and reaches a steady state current value.

Approximate potentials can be set for Lens 1 and Lens 2 at 16.4 and 13.5 keV, respectively, for a 20 keV anode potential. If other anode potentials are desired, the Lens voltages will scale while lowering the anode voltage. Current is maximized for a particular grid voltage. A typical value is 40 V, with lower voltages increasing the C_{60}^{+}/C_{60}^{++} ratio while decreasing overall current, and higher voltages decreasing this ratio while increasing overall current. The beam current is maximized by varying the repeller voltage (typically under -10 V), and the first set of x and y alignment plates (x1 and y1) using the ion source controller, along with Lens 1 and the second set of alignment plates (x2 and y2) using the ion gun controller. If the source was previously misaligned, it may be necessary to repeat this procedure. Lens 2 is adjusted for final focusing, with the most accurate focusing achieved by using a smaller aperture first (providing there is enough beam current to do so), at a specific sample height. If, for example, a film on silicon is being studied, imaging a copper grid on the corner of the silicon piece ensures optimum focusing for that sample. Additionally, a well-focused beam at one aperture does not imply that the beam will be well-focused when using a different aperture. Depending on the orientation and age of each aperture, the first and second sets of alignment plates and Lens 1 may need to be adjusted in addition to Lens 2 to obtain the highest lateral resolution. The 300 μm aperture is generally the best starting point for focusing the ion beam. For the smallest apertures, the stigmator values on the ion gun controller can be adjusted to improve beam shape, and thereby improve lateral resolution. For the stigmator angle function to have an effect, the amplitude must be a non-zero number.

In the event that no beam current is hitting the sample, but everything in the source is working correctly, a 17 mm wrench can be used to adjust the equipped bellows assembly, as shown in Figure **2-3**. By loosening one of the nuts on a particular leg, the other nuts can be adjusted to move the bellows in the desired direction. The source nosecone inside the sample analysis chamber is moved several mm in each direction using this method, and care is needed to not strike the spectrometer extraction optics with the tip of the nose cone. This procedure is generally only needed when the source has been completely removed from the instrument, or if the beam target is being aligned to overlap with another ion source. The source position should be adjusted for maximum SIMS signals occurring at the median positions of the spectrometer octupoles.

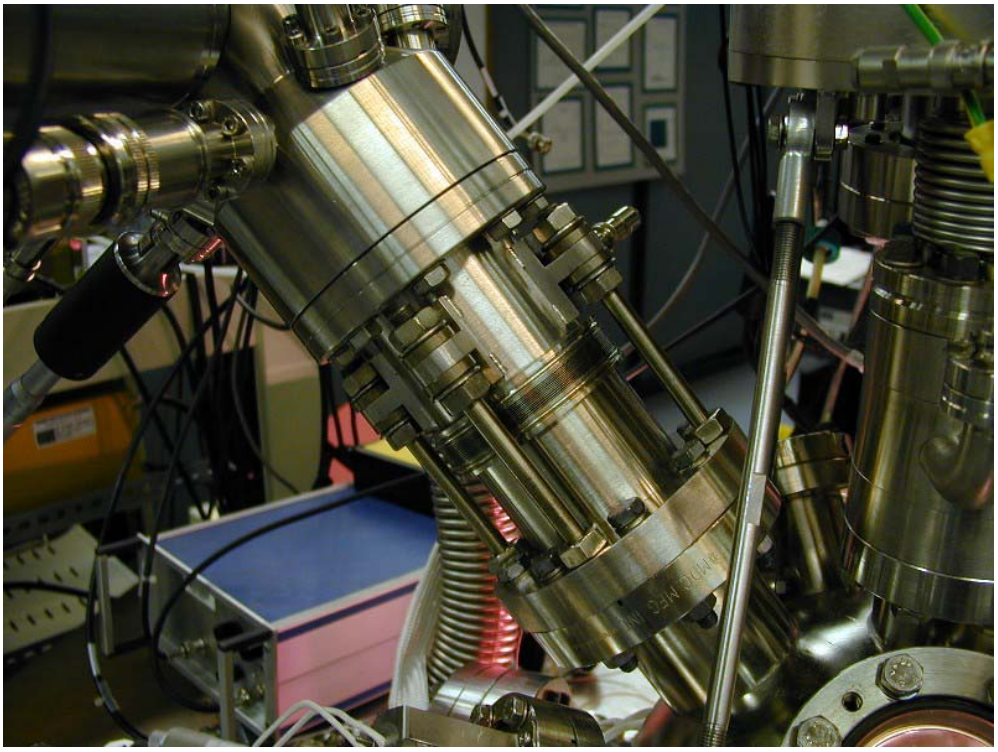

Figure **2-3**: Front view of the 20 keV C_{60}^{+} ion source, emphasizing the adjustable bellows assembly.

2.3.3 Source Pressures

The vacuum line between the source pumping port and the turbomolecular pump contains a hot filament ion gauge for monitoring source pressure. Positioning of the gauge is closer to the pump than to the source to avoid carbon coating of the filaments, thus ensuring longer filament gauge lifetime.

If the source is pumped down from atmosphere, the pressure is typically 10^{-5} torr when the turbo pump first reaches maximum rotation speed. Within ½ to one hour, the pressure drops by about an order of magnitude. The pressure will eventually reach 10^{-8} torr at room temperature. When the source is first heated after exposure to atmosphere, the pressure can increase to the high 10^{-5} torr due to the presence of adsorbed water on the internal components. This pressure will drop to near 10^{-7} torr during operation and 10^{-9} torr in standby mode. A newly conditioned filament will also outgas considerably until all of the impurities are removed.

2.4 Troubleshooting

2.4.1 Source Leakage

The main cause of source "breakdown" is the buildup of carbonaceous deposits on the source insulators. The carbon coating creates a path for current between adjacent components. The leakage of these currents across an insulator can approach 400 μA until the power supply cannot drive enough high voltage. The insulators are designed to

separate adjacent components in the source with GΩ resistance while at 20 keV, but the source can operate well until these values drop below 50 MΩ. At this point, the measured current from leakage across the source components begins to rise from a nominal value of 0.1 μA. At proper operating conditions, this value is generally between 3 and 30 μA. The value increases gradually over time and if above 100 μA, is an indication that the source will soon need to be serviced to clean the insulators. If there is an electrical arc in the source, and the high voltages shut down, the cumulative leakage has met or exceeded 400 μA. As the value increases over time, it is important to monitor the leakage current of the lenses and extractor as one particular component insulator can coat with carbon faster than others. Typical leakage values are <10 μA for the lenses and -20 μA for the extractor. If these electrodes reach leakage values of >20 μA, source cleaning will need to ensue with particular attention to the component insulator causing the highest leakage. The anode leakage readout is the sum of the lens and extractor readouts, plus any additional leakage to ground in the feedthrough, the high voltage leads, etc., and often is high when the other readouts appear normal.

For each source leakage issue, the problem may exist with the source, a high voltage cable, or the power supply. After turning all high voltages to zero, the deemed problematic component lead can be disconnected from the ion gun, and placed into an insulating material such as a foam nitrogen dewar. Potential can be applied slowly, and manually, up to 15 keV in this manner. If the problem persists, the cause is outside of vacuum, and vice versa. A similar test can be performed to isolate the cable from the power supply.

2.4.2 Filament Issues

Often when the filament is in the normal operating range of current (>2 A), and particularly after filament replacement, the grid current appears low, and may even be under 1 mA when the current applied to the filament is 2.5 A. The grid current should generally increase with heating time as the source reaches temperature and pressure equilibrium. A reduced grid current can also be observed after many hours of source operation if carbon deposits onto the filament. If carbon deposition occurs, it is often difficult to attain higher grid current values again without changing the filament. An additional observation that is related to the filament not being hot enough to emit electrons is the maximum current that can be applied. The supply can provide up to 4 A, but it is possible to see the maximum applied current fall to just over 2.4 A. This occurs because the circuit cannot apply more than 10 V. If the filament is not emitting electrons, the circuit temperature increases, the resistance of the circuit increases, and the maximum possible current falls accordingly. Under typical operation conditions, the applied current is not more than 2.6 A.

If the filament is not working properly, and other testing methods do not pinpoint the problem, the filament circuit board in the high voltage power supply may not be operating normally. To attribute a problem to the power supply board, a 1 Ω, 50 W resistor (available from the electronics shop), is placed into the filament leads A and F of the 6-pin high voltage cable to simulate the filament circuit in vacuum. With a multimeter measuring across the resistor, 1 V should be observed when 1 A on the

current readout of the ion gun controller is being applied using a correctly working filament circuit board. Up to 2 A can be applied using this method.

Damage and apparent damage to the filament require venting of the source for repair. If the filament current readout cannot surpass 0.24 A, the filament is likely broken. However, if the filament readout cannot surpass 0.48 A of current, the filament is likely misshapen and touching the grid or repeller. The heating and cooling of the filament leads to misshaping, and occasionally the filament touches the grid or repeller, leading to a high current reading and/or peculiar voltage activity on the readouts for the grid or repeller. This problem can often be rectified by returning the filament current to zero, and cooling the entire source by reducing the reservoir heater to 8 V for one hour. The source will cool enough to change the filament shape again, and the source can be subsequently reheated to operating temperature with a correctly working filament.

2.4.3 External High Voltage Pin Testing

Problems inside of the source can be pinpointed outside of vacuum with both continuity and resistance measurements of the high voltage pins. A 6-pin Amphenol connector is used to apply the floated high voltages to the source, and is pictured in Figure **2-4**. The six pins are labeled A-F and are assigned as follows: A – anode/filament, B – open, C – repellor, D – grid, E – extractor, and F – filament. As a point of reference, pin F is located directly underneath the notch in the Amphenol connector. For a properly working source assembly, pins A and F should be shorted, indicating that the filament is connected. All other pins are isolated. The resistance

between pins A-F is that of the filament wire, or 0.2 to 0.4 Ω. All other pin combinations are open loop on the 2000 MΩ scale of a digital multimeter, and open loop to ground (the source casing). Lower resistance measurements between pins indicate problem areas, and may include carbon coating on the ceramics or a filament issue. Generally, once the isolation between components dips below 100 MΩ, service is in the imminent future. Additionally, the source is not reassembled with resistance readings between components that are below 40 to 50 MΩ.

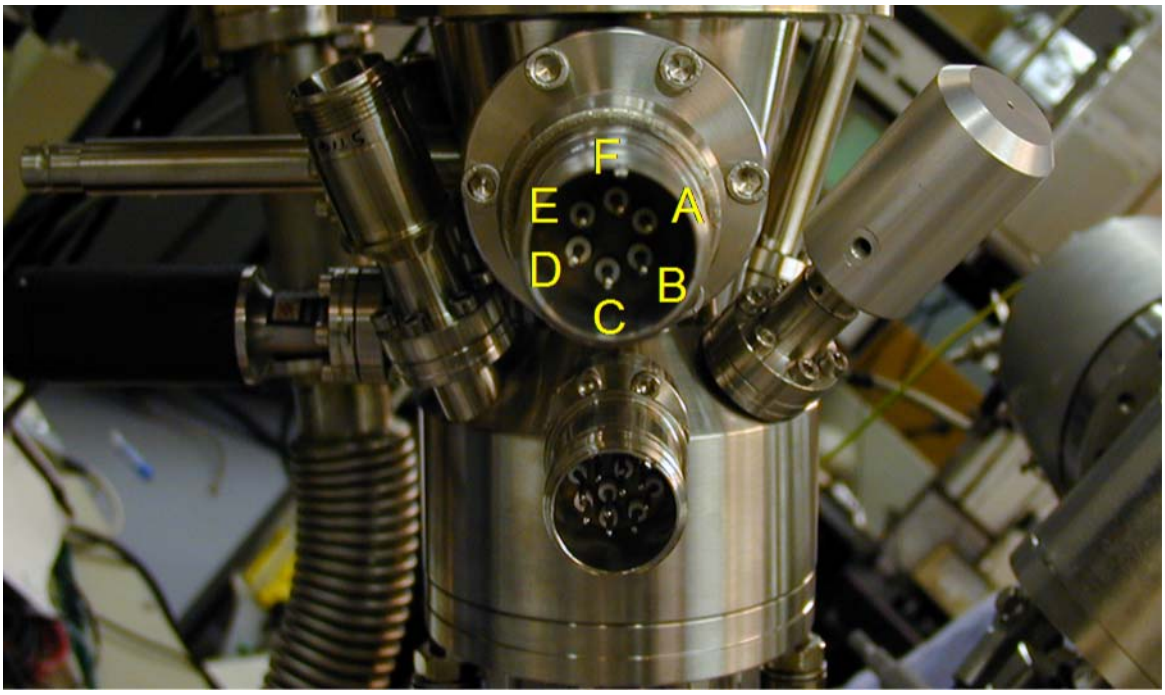

Figure **2-4**: 20 keV C_{60}^{+} ion source high voltage feedthrough with labeled 6-pin Amphenol connector.

2.5 Maintenance

2.5.1 Source Disassembly

Once a problem is diagnosed to be inside of the source vacuum, the source needs to be disassembled. All electronics units should be turned off properly, and all cables removed and positioned away from the source. A set of metric allen wrenches and nut drivers, a digital multimeter capable of measuring up to 2 GΩ resistance, fine-tipped tweezers, methanol/ethanol, lint-free wipes, and spare C_{60} materials are required. If the source is vented to atmosphere, the back flange, shown in Figure **2-5**, is removed from the source by releasing the 16 socket-head bolts with a 6 mm allen wrench. The flange is removed slowly and evenly along the ion column axis, as there is only a 3 mm clearance between the ground shield and the high voltage leads. In the event that the halogen bulb ceases operation, the smaller 2.75" flange located on the top of the source is removed, and the bulb replaced. The flange is replaced so that the bulb is centered perfectly within the housing. The bulb must be centered in the copper holder to prevent an electrical arc from forming between the two components.

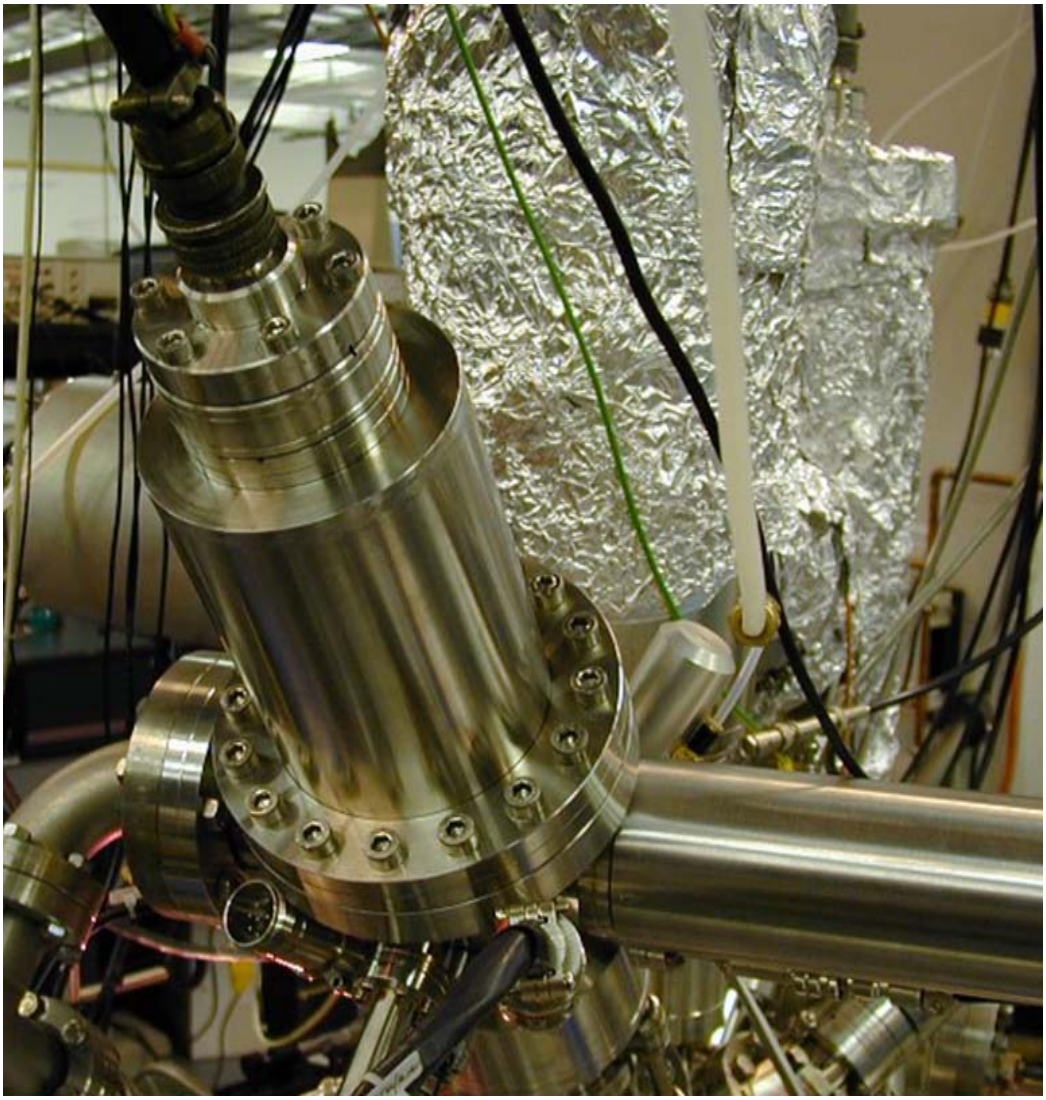

Figure **2-5**: Rear view of 20 keV C_{60}^{+} ion source emphasizing the back flange and bulb flange.

After the back flange is removed, disassembly proceeds as depicted in Figure **2-6**, with only gloved hands used to touch the interior components. The upper left picture shows the source after removing the back flange. Within visibility are the copper holder, repeller, bottom grid plate, and the extractor assembly. The corresponding leads from Figure **2-4** extend through the high voltage feedthrough and make a right angle to the

components on the central column. The two copper leads connect to the filament legs, which are anchored within the repeller, and isolated by t-shaped insulators. Each of the two copper leads is disconnected from the filament/repellor assembly with a correctly sized nut driver. The extractor lead, which is positioned the most left among the leads, connects to the top extract plate by being coiled under a nut. This nut is threaded and held in place on the closest top grid plate screw and is removed with a pair of needle-nosed pliers. Towards the rear of the image are the leads for the grid and repeller. The grid lead connects to a post that extends from the bottom grid plate, and coils around a socket head screw and the post. An allen wrench is used to loosen the screw and release the lead. The repeller lead coils underneath a nut directly attached to the repellor and can be removed with a nut driver that is just slightly larger than that used to remove the filament leads.

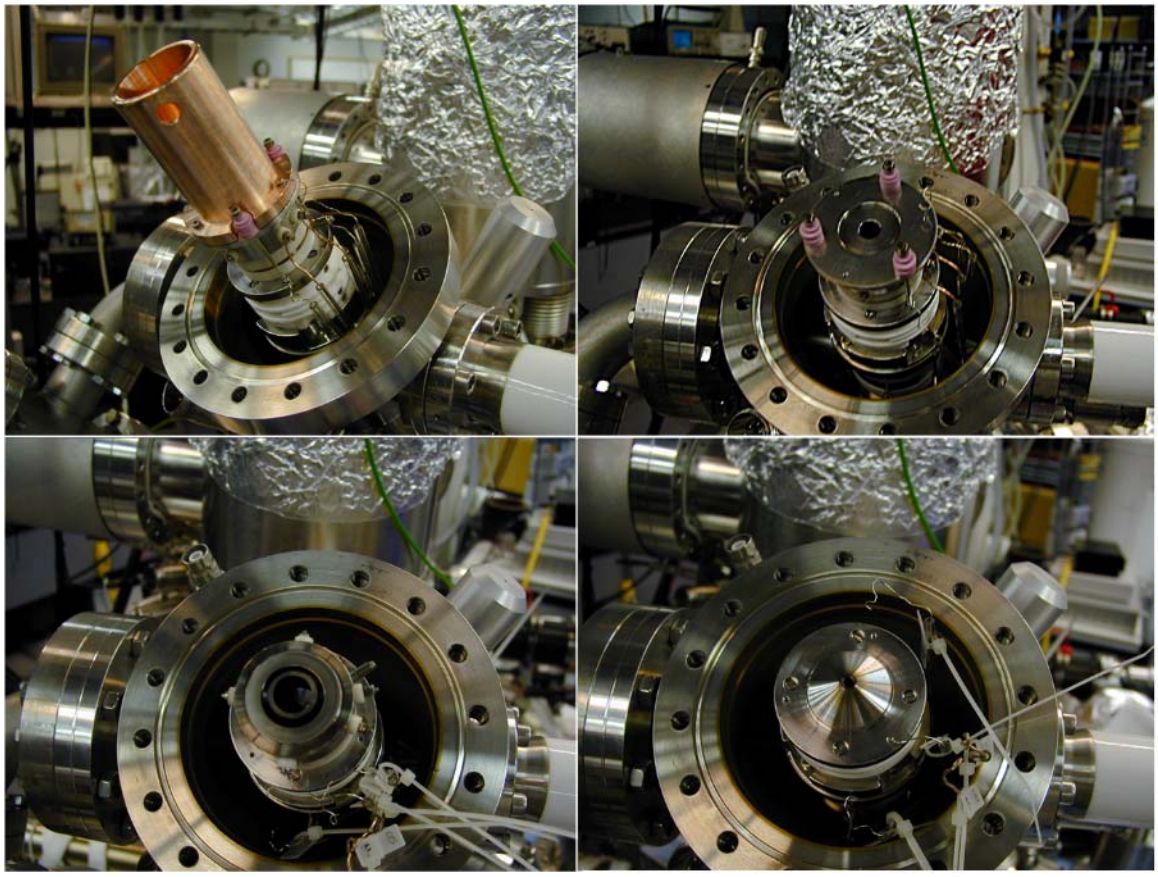

Figure **2-6**: Iterations of disassembly pictures for the 20 keV C_{60}^{+} ion source. Upper left shows the ion column after the back flange is removed, upper right after the copper holder is removed, lower left after the top grid plate is removed, and lower right after the grid/filament/repeller assembly is removed. The lower right picture shows the top of the extractor assembly.

The upper right image in Figure **2-6** shows the source column after the copper holder is removed. To remove the copper holder, three straight-head screws are removed that fasten it to the top grid plate. One screw has a piece of wire coiled underneath the head, connecting the copper holder to the bottom grid plate post. This screw is removed first to allow an easy removal of this wire from the copper holder. The wire can remain fastened to the bottom grid plate post. Once these three screws anchoring the copper holder are removed, the copper holder is slowly removed with fingers placed in the

vacating space to catch the C_{60} reservoir, which often remains attached to the copper holder. The back end of the C_{60} reservoir is open, and if toppled will spill C_{60} powder into all areas of the source, resulting in a never-ending cleanup. The C_{60} reservoir is secured while servicing the column, by placing onto a scintillation vial, wrapping the entire unit in foil, and placing in a cupboard to avoid accidental spilling of its contents.

Three long screws with pink insulators hold the top grid plate, filament/repeller assembly, and grid to the top extractor plate. An allen wrench is used to loosen these screws in order to remove the top grid plate. (The nut holding the extractor lead from one of the screws has already been removed). Slowly removing the top grid plate allows for the top-heavy repeller and grid entity to stay in place until removal is desired. The lower left picture in Figure **2-6** shows the repeller and grid after the top grid plate is removed. At the time of the picture, zip ties were used to label the individual leads, but this action is unnecessary given the external pin assignments of the high voltage feedthrough. A multimeter is easily used to determine lead assignment. Removing the repeller, grid, and the two ring-shaped ceramic insulators is performed in one gentle upwards lifting motion, with support being given to the bottom insulator while lifting. The lower right picture of Figure **2-6** shows the top extractor plate after the repeller and grid components are removed.

The extractor assembly, consisting of the top extractor plate, bottom extractor plate, and large extractor isolator is removed from Lens 1 by loosening the four socket head cap screws on the bottom extractor plate. To prevent the loss of these screws to the source chamber, a pair of curved-tip tweezers is used to hold each screw while a long allen wrench at a slight angle is used for loosening of each screw.

The top left picture in Figure **2-7** shows the remaining serviceable portion of the source column after the extractor assembly is removed. The extractor exit/Lens 1 entrance is clearly shown. This area becomes extensively coated with carbon, but the coating does not adversely affect source performance. However, a lint-free wipe is used with a low molecular weight alcohol such as methanol or ethanol to remove residual carbon buildup. The wipe will appear brown in color after removing the residue, and this brown color is characteristic of some of the carbon-coated stainless steel components.

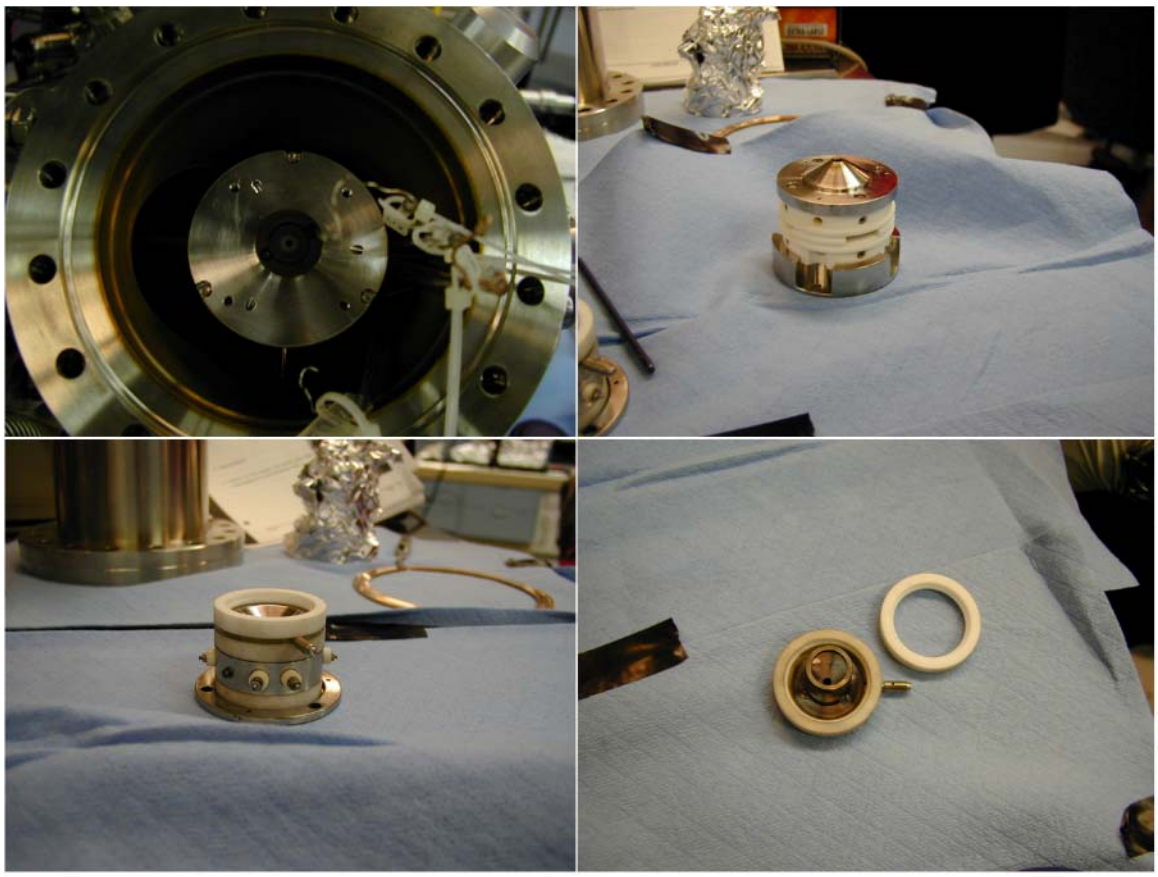

Figure **2-7**: Pictures of 20 keV C_{60}^{+} ion source components. Upper left shows the Lens 1 assembly after the extractor assembly is removed, upper right shows the extractor assembly, lower left shows an inverted view of the top grid plate, filament/repeller assembly, and bottom grid plate with insulators, and bottom right shows grid/bottom grid plate, a dirty insulator, and freshly cleaned ring insulator.

The remaining images in Figure **2-7** depict the extractor assembly, the filament/repeller/grid assembly, and the grid after being removed from the source. As is seen in the image, the contour of the top extractor plate forms a flush fit into the bottom grid plate. The lower right image shows one of the alumina ring insulators after removal from the source adjacent to a clean white ring insulator for comparison. Alumina is used in this part of the source for insulators instead of the material Macor that is used for the extractor isolator since the area closest to the ionization region reaches higher temperatures and suffers more stress than those insulators situated further down the column. The alumina is harder and more durable than Macor, but is also more expensive to make because only a diamond cutter can shape the materials.

Generally, each servicing will involve removing up to and including the extractor assembly. However, if the Lens 1 insulator is coated with carbon, this electrode must also be removed. Three long screws, visible in the top left image of Figure **2-7**, are loosened, and the Lens 1 assembly, similar in appearance to the extractor assembly, is removed.

2.5.2 Source Cleaning

All insulator components develop a sub-surface presence of carbon. The constant heating and cooling of the source on a daily basis seems to embed the carbon within the outer layers of the ceramics. Because of this effect, chemical treatments have little influence on alleviating the carbon buildup. The fastest and most efficient means of cleaning the insulators is to use a sandblaster. Glass beads of 50 μm diameter are placed

in the bottom of the sandblaster and compressed air is used to power the sandblaster gun. The stream of beads is directed toward the insulators, with a few seconds on each discolored area being sufficient to clean the carbon-coated areas without eroding significant amounts of material. However, prolonged sandblasting of one area can cause pock-marking, especially for the softer Macor insulators. To remove the excess bead particles, each insulator piece is sonicated for ten minutes in methanol or ethanol, followed by an oven bake at about 80ºC for 20-30 minutes. An aluminum foil "boat" is used to protect the insulators from scratching on the grates of the oven. The details of this procedure are essential to attaining long lifetimes with the source.

The small ceramics that insulate the screws and filament legs in the source can be cleaned using the same method as the larger ceramics by sliding them onto a threaded rod, placing a nut onto both ends, and continuing with the outlined procedure.

Depending on the metallic component and its function, different cleaning methods are used. The copper holder, top grid plate, repeller, grid/bottom grid plate and top extractor plate are cleaned of carbon buildup using Scotch-Brite, or a similar abrasive sanding material. The underside of the top extractor plate, the bottom extractor electrode, and the Lens 1 electrode are lightly sanded with 400 or 600 grit sandpaper. The 400 grit is used first to loosen most of the material, and the 600 grit is used to retain the smooth nature of these stainless steel pieces. Circular motions are most effective for retaining optimum smoothness. Both methods are followed with a methanol or ethanol rinse and subsequent nitrogen gas drying.

After several servicing cycles, some of the screws are heavily coated with carbon, become brittle, and should be replaced. The most commonly replaced screws are the three that hold the copper holder to the top grid plate.

2.5.3 Source Assembly

Before the cleaned components are re-assembled to form the source column, the filament will need to be replaced. Once the filament has been used and encounters atmosphere, it becomes extremely brittle and breaks easily. The filament is completely removed by using tweezers to pull the broken pieces through the two threaded filament support legs where the anode potential is applied. The two nuts that secure the filament legs in place need to be loosened, and the ceramic insulators cleaned if the resistance between filament legs and repeller has become unacceptable. About three to four inches of fresh 0.15 mm diameter, 1 % thoriated tungsten wire is used to replace the filament.

The filament wire is threaded through the small holes in the center of the two filament legs and guided through the loops on two other support legs within the repeller assembly. A few mm of filament should extend past the filament legs in front to be snipped off once the entire column is assembled. The filament should be shaped evenly enough to maintain a few mm distance away from the grid, while not forming right angles at the entries to the filament legs. Sharp angles cause weak points in the filament, and premature breakage. The filament legs are tightened and perfectly centered within the insulated repeller holes with the two front nuts. If not properly centered, a high voltage arc is likely between filament and repeller. Additionally, the filament should be

resting in contact on the other support legs, with resistance from each support leg to repeller being equal – indicating that all are in contact via the filament. In the event that the filament is not secure in one of the filament legs, the hole in the center of the leg has likely opened too much, and the leg should be replaced.

The assembly of the source column is completed in the reverse order of disassembly, with Lens 1 being the most tedious to replace. The three long screws that hold the Lens 1 assembly to its mount need to be tightened *equally*. The best method for doing this is to finger-tighten each screw, and use an allen wrench to turn each of the three screws progressively tighter with fractions of a twist during each iteration. If Lens 1 is not centered on its mount, the electrode may not function properly, and the source may never be aligned correctly for optimum focusing since the focal point through the axis bend may not be centered with the ion column axis.

With Lens 1 securely in place, the extractor assembly is fastened to the top plate of the Lens 1 assembly. Using tweezers to hold each screw in place, an allen wrench at a slight angle is used to secure the extractor to the lens. The delicate insulator/grid/insulator/repeller assembly is next on the column and should be held in place before and during the fastening of the three long screws and the top grid plate. Orientation of this assembly is critical for equal spacing of the high voltage leads. Two sets of three equally spaced screw holes are present in the top grid plate. The three long screws are placed through the larger diameter holes. With the top grid plate held in place before tightening, the repeller and grid are rotated such that the two filament legs point perpendicularly to the column axis, with the grid post equally spaced between these legs and the closest top grid plate screw. The resulting positioning leaves enough space for

the repeller high voltage lead to be attached without being close enough to arc to the top grid plate screw. The coiled extractor high voltage lead is affixed around the appropriate screw before completely tightening the top grid plate.

The top grid plate screws are tightened equally to secure the column components and to provide a level surface for the C_{60} reservoir. If the screws are not properly centered in the holes of the top grid plate and/or the pink insulators shift when tightening, an arc can form between the copper holder/grid and the top extractor plate. If needed, fresh C_{60} powder is added to the reservoir until $^2/_3$ full. The reservoir is placed in its groove in the top grid plate and securely held in place while the copper holder is attached. The holder and reservoir have little tolerance in their fit and may need to be adjusted to ensure a flush fit with the top grid plate. The two screws that hold the copper holder in place but are not connected to the grid wire are tightened about $^2/_3$ before tightening the wire underneath the other screw. All screws are tightened evenly to ensure equal spacing between copper holder and top grid plate, as well as between copper holder and the back flange bulb.

Before affixing the high voltage leads, a multimeter test is performed to check all resistances and continuity between the filament leads. The leads are spaced in the proper order as follows, from rear to front of source, to prevent overlap of the paths from the high voltage feedthrough: extractor, filament leads, grid, and repeller. The previously connected extractor lead is tightened with needle-nosed pliers. The copper leads are secured to the filament legs with a nut driver. Over-tightening of these leads can cause the filament legs to become within arc distance of the repeller. A resistance check between filament and repellor is performed to ensure the spacing between each filament

leg and repeller is proper. The extended filament distance on each leg is cut to prevent the formation of an arc between filament wire and ground shield. An allen wrench is used to tighten the grid high voltage lead to the grid post while simultaneously tightening the wire to the copper holder. Over-tightening this screw will cause the grid post to snap. The final high voltage lead to the repellor is tightened with a nut driver.

The five high voltage leads are spaced equally between the ion column components and the back flange grid shield to prevent an arc from developing. While adjusting the high voltage leads, an inspection of the quartz tube insulators should show no cracks or chips where high voltage can escape and arc to the ground shield. If broken, these need to be replaced. The high voltage leads should be equally spaced between the source casing and ground shield, but the movement of the leads can lead to shifting in the high voltage feedthrough. A long, sturdy pair of tweezers is used to individually push each lead from the right angle towards the feedthrough to maintain a flush connection with the Amphenol connector. If an arc develops between leads in the high voltage feedthrough, the leads are disconnected from the column components and placed on the top (front) side of the source column in order to be collectively removed through the right angle in the source casing. The feedthrough is removed along with the leads, and the connection of each lead to the Amphenol connector is verified. The leads are guided by two pieces of ceramic insulator, which are pushed together to prevent an arc from developing. Re-assembly is the inverse of disassembly for the high voltage leads in the feedthrough after a new gasket has been placed in the knife edge groove.

Once a new gasket is placed in the knife edge groove, the back flange of the source is lowered into place in a level manner to prevent hitting source components. The

flange bolts are of two different lengths, and are installed in a short-long-short pattern for an even seal. After fastening the bolts, the source is pumped and the pressure monitored after the turbo pump has reached maximum rotation speed.

2.6 Testing the Source after Service

Pressures are monitored as described in section **2.3.3**. With source pressure of 5 x 10^{-6} or lower, the electronics units are turned on properly and the high voltages manually increased to 20 keV, in a rather deliberate manner. A potential of 20 keV can be applied to each electrode when the source is cold. The leakage currents of the anode, Lens 1, Lens 2, and extractor are monitored. The anode leakage should not be more than 20 μA for a cold source at 20 keV. Some fluctuations in pressure are expected, but should gradually decrease. The filament is slowly turned to 0.5 A, and then 1.0 A to outgas. Large increases in pressure will be observed. If the filament does not reach 0.5 A, the information to rectify this problem is described in section **2.4.2**.

The high voltage is returned to zero manually, and the heater reservoir voltage turned to 7.0 V to begin heating the source while leaving the filament at 1.0 A. The source will reach an equilibrium temperature and continue to pump down to 10^{-7} torr within 12 hours. The high voltage is slowly raised to 10 keV while monitoring the leakage currents. At 10 keV and with a warm source, the leakage should be about 2 μA or less. The anode potential is gradually raised, along with the lenses by 1 keV iterations as long as the source components do not arc. Once at 20 keV, the anode leakage can be as high as 30 to 40 μA, but will decrease with further pumping and the heating/cooling

cycles of normal gun operation. This procedure is duplicated for the source reservoir heater at 10.0 V (operating temperature). Upon completion of voltage "training", the source should operate properly, with the source pressure and anode leakage decreasing with time.

2.7 Conclusions

A comprehensive overview has been provided of the operational principles of the 20 keV C_{60}^{+} ion source, its operational procedures, and service regimen. When the guidelines of this chapter are followed closely, the source will operate for greater than 1,000 hours, or at least six months, between servicing periods, where an hour of operation is defined as one hour that the source is at operating temperature. These lifetimes have improved from the two to four weeks between servicing upon arrival of the prototype.

2.8 References

1. Hertel, I.V., Steger, H., de Vries, J., Weisser, B., Menzel, C., Kamke, B., Kamke, W., *Phys. Rev. Lett.*, **1992**, *68*, 784.

2. Volpel, R., Hofmann, G., Steidl, M., Stenke, M., Schlapp, M., Trassl, R., Salzborn, E., *Phys. Rev. Lett.*, **1993**, *71*, 3439.

Chapter 3

C_{60}^+ and Ga^+ Bombardment of Ag Surfaces

This chapter is adapted from: Sun, S., Szakal, C., Wucher, A., Winograd, N., *J. Amer. Soc. Mass Spectrom.*, **2005**, *16*, 1677, with permission.

3.1 Introduction

The elucidation of the mechanism of interaction of energetic polyatomic or cluster ions with surfaces is of current interest since these projectiles are now being extensively employed as desorption probes in SIMS experiments.[1,2] Because of their propensity to produce higher molecular ion signals than corresponding atomic ions and the emergence of commercially available [C_{60}^+] [3,4] and [Au_3^+] [5,6] ion guns, applications have expanded dramatically. For example, these sources can be focused onto the sample with a probe size on the order of 1 micron, allowing greatly improved molecule-specific imaging experiments. The high secondary ion yield associated with the cluster/solid interaction also allows for molecular depth profiling studies without the accompanying damage accumulation normally associated with atomic bombardment.[7-17]

The mechanisms associated with the observed secondary ion yield enhancement are not yet clear, although details are emerging quickly. A basic question that must be resolved is to determine whether the yield enhancement occurs as a consequence of

increased ionization efficiency, or is due to more effective sputtering in the neutral desorption channel. There is mixed information about this point. For In and Ag surfaces, for example, it has been shown that the enhanced secondary ion yield under SF_m^+ bombardment (m = 1-5) largely arises from the enhanced ionization efficiency due to implanted F atoms.[18] For organic systems, however, very high removal rates of neutral species have been reported,[2] obviating the need to invoke enhancement of the secondary ionization probability. Most recently, yields and velocity distributions were measured for In and In_2 sputtered from In surfaces bombarded with Au^+, Au_2^+ and Au_3^+.[19] Although these experiments do not address the issue of enhanced ionization, they do show that there are enhancements in the sputtering yield that cannot be explained by either collision cascade theory or by thermal spikes. The spike model has traditionally been employed to interpret the response of metallic targets to cluster bombardment.[20] Instead, the emission mechanism is proposed to involve the quasi-free expansion of a supercritically heated subsurface volume.

Recent molecular dynamics (MD) computer simulations show a largely different desorption process for isoenergetic Ga and C_{60} bombardment.[21,22] For 15 keV Ga bombardment of Ag{111}, atomic motion is described by a classical collision cascade with a desorption yield of about 20 Ag atoms per incident Ga^+ ion. For 15 keV C_{60} bombardment, however, crater formation with minimal subsurface damage has been reported and there is virtually no evidence for the formation of traditional collision cascades. The desorption yield of Ag is predicted on the order of 300 atoms per C_{60} impact, suggesting an enhancement factor of about 15-fold. Even larger enhancements are observed for small sputtered clusters of Ag. These recent calculations of neutral C_{60}

bombardment produce results consistent with earlier MD calculations for the C_{60} bombardment of graphite.[23-25] Crater formation has also been observed using other systems as well.[24-27] None of these calculations address the issue of enhancements in the ionization channel, of course, but they do provide basic information about how the atoms move under these novel circumstances.

In this chapter, experiments comparing the bombardment of Ag{111} with energetic Ga^+ and C_{60}^+ projectiles are conducted in order to make direct comparisons with published MD calculations. The results show that the enhanced secondary ion yields observed for this system are predominantly caused by enhancements of the respective partial sputter yields, as measured by quartz crystal microbalance (QCM) experiments. More specifically, we find that the neutral Ag yield is increased about 6-fold under bombardment with 15-kev C_{60}^+ as compared to isoenergetic Ga^+ projectiles. For sputtered neutral Ag_2 and Ag_3, the yield enhancements are even larger, in qualitative agreement with the calculations. Moreover, velocity distributions of neutral atoms and clusters are found to exhibit pronounced differences between Ga^+ and C_{60}^+ bombardment. These results also agree with the predictions of the MD calculations and further support the recently proposed notion that cluster bombardment produces a response that is reminiscent of a quasi-free expansion of desorbing particles.

3.2 Experimental

3.2.1 ToF Spectrometer

Experiments were performed on a BioTof time-of-flight secondary ion mass spectrometer (ToF-SIMS), which has been described elsewhere.[28] In this study, 20 keV C_{60}^+ ions from the ion source described in chapter 2 as well as 15 keV Ga^+ ions are employed. Both ion beams are carefully overlapped, and either the Ga^+ or the C_{60}^+ ions are used to bombard the investigated surface to release secondary ions and neutral particles. The primary ion bombardment is operated in a pulsed mode with pulse durations ranging from about 1 μs down to 50 ns. During the primary ion pulse, the sample is kept at ground potential to ensure that the impinging beam is not deflected by the ion extraction field.

While the secondary ions are directly accessible to mass analysis, the sputtered neutral particles are intercepted by a pulsed laser beam for postionization. Both secondary ions and photoions are then extracted into a time-of-flight (ToF) mass analyzer by applying a pulsed positive potential of 2.5 kV to the sample stage. The extraction pulse was delayed with respect to the end of the primary ion pulse by a variable time which will in the following be called "stage delay". For postionization experiments, the ionizing laser beam is guided parallel to the sample surface at a distance of approximately 1 mm. The firing time of the laser pulse is delayed with respect to the ion extraction pulse by a variable time interval ("laser delay").

The Ti:Sapphire femtosecond laser system (Clark-MXR, Inc. MI, U.S.A) employed here has been described elsewhere.[29] The system is based on an Ar ion laser-

pumped, self-mode-locked Ti:Sapphire oscillator that generates 800 nm pulses with 50 fs pulse width and 300 nJ/pulse energy. The pulses go through two stages of amplification to reach a final output of up to 3.5 mJ/pulse at a wavelength of 800 nm and a repetition rate of 1 kHz.[30] The laser beam is coupled into the vacuum chamber via a CaF_2 lens with 25 cm focal length. The focal conditions are chosen such as to produce a beam cross section of 150 μm diameter in the interaction region above the sample surface.

During the measurements determining the partial sputtering yield of sputtered atoms and clusters, a relatively long projectile ion pulse of about 1 μs duration is chosen. This ensures that particles of all relevant emission velocities are present in the ionization volume and interact with the ionizing laser. In order to determine the emission velocity distributions of sputtered neutral particles, on the other hand, the primary ion pulse width is reduced to 100 ns, and a controlled time delay between the projectile ion and the ionizing laser pulse is introduced as the sum of stage and laser delay. This operation mode selects the emission velocity of the detected neutral particles via their flight time between the surface and the ionization volume.

The velocity distribution *f(v)* of the sputtered neutrals is evaluated from the measured delay time distribution *s(t)* of the detected photoion signals by [31]

$$f(v) \propto \frac{s(t) \cdot t}{\Delta r + {}^{r}\!/_{t}\, \Delta t} \tag{1}$$

where r denotes the distance between the sample surface and the laser ionization volume, Δr is the spatial extension of the laser beam in the direction along the surface normal (570 μm) and Δt is the laser pulse width. Due to the ultrashort laser pulse duration of about 100 fs, the second term in the dominator of eq. (1) is far smaller than the first term and

may safely be omitted. The emission velocity v is given by r/t, requiring an accurate measurement of r. This is done by translating the laser beam towards the sample surface until ablation occurs, indicated by large corresponding ion signals shown in the spectrum.

The mass selected ions are detected by means of a Chevron stack of two microchannel plates (MCP) that are operated with 18 keV postacceleration. During registration of neutral atoms and small clusters, a flight time peak may be composed of many ions, and therefore an analog detection scheme is employed in which the charge produced by the MCP is directly digitized by means of a fast transient recorder. In order to avoid detector saturation, the gain voltage across the MCP is reduced such as to ensure that the maximum recorded signal does not exceed a height of about 100 mV at 50 Ohm termination.

The Ag sample used for measuring postionized neutrals was purchased from Aldrich. A small piece of polycrystalline silver foil is etched for 30 s in 30% HNO_3, then rinsed with water and methanol and nitrogen-dried. After introduction into the UHV system (base pressure $1x10^{-9}$ mbar), the surface is sputter-cleaned using C_{60}^+ ion bombardment until all peaks in the mass spectra reach a steady state value, usually after an ion fluence of 10^{15}-10^{16} cm^{-2}.

3.2.2 Quartz Crystal Microbalance

The total yield of Ag is measured using a quartz crystal microbalance (QCM, Maxtek TM-400). For that purpose, a standard AT-cut quartz crystal with a resonance frequency of 6 MHz is mounted in a specially modified sample holder. The crystal is

coated with a finely polished Au top contact electrode which covers the entire crystal area of 13 mm diameter. The bottom electrode has a smaller diameter of 6.6 mm. A polycrystalline Ag layer of about 500 nm thickness is vapor-deposited onto the top electrode, forming the target surface for the ion bombardment experiments. A Cr barrier layer of 50 nm thickness was introduced between the Ag and Au films in order to prevent the formation of an Ag-Au alloy. Upon introduction into the UHV system, a stable situation is reached within a few minutes with a displayed deposition rate of zero. If the dc ion bombardment is switched on, a negative deposition rate is displayed, indicating the sputter removal of surface material. The removal rate is measured by integrating the total thickness variation displayed by the controller over a time period of 60 s (C_{60}) or 300 s (Ga). In order to ensure that the measured data is not influenced by thermal drift, it is verified that the displayed removal rate value returns to zero after the ion bombardment is switched off.

For a homogeneous deposition or removal of an aerial mass density Δm_a (g/cm^2) at the top electrode of the quartz, the frequency change Δf is described by [32]

$$\Delta m_a = D_\infty \cdot \Delta f \ , \qquad (2)$$

provided the total change is sufficiently small (< 2%) compared to the nominal resonance frequency f (6 MHz).[33]

The QCM controller used here has been designed as a film thickness monitor and therefore displays a thickness change Δd (nm) instead of the frequency change. Apart from a minor correction for differences in the acoustic impedance of quartz and coating

material (which is only important for large frequency changes and therefore always negligible in our experiments), the displayed value of Δd is internally calculated as

$$\Delta d = F_t \cdot \frac{\rho_q}{\rho_f} \cdot N_q \cdot \Delta\tau \ , \tag{3}$$

where ρ_q denotes the density of the quartz, $N_q = 1.668\text{x}10^5$ (Hz·cm) is the quartz constant permanently programmed into the controller, and $\Delta\tau$ is the measured change of the quartz oscillation period $\tau = 1/f$. In order to correct for the density ρ_f of the coating film, an assumed value is input into the controller by the user. The displayed values of Δd were corrected for the user selectable tooling factor F_t to correspond to $F_t = 1$.

From eqs. (2) and (3), the proportionality constant D_∞ can be calculated from $\Delta m_a = \Delta d \cdot \rho_f$ as

$$D_\infty = \frac{\rho_q N_q}{f^2} \ , \tag{4}$$

which for a quartz density of 2.65 g/cm^3 results in D_∞ = 12.28 ng/(cm^2·Hz). This value refers to a situation where the deposition or removal of material is uniformly distributed over the entire quartz surface. If only a section of the surface is influenced by the ion bombardment, the spatial sensitivity of the induced frequency change becomes important. It is well known that the latter is described in good approximation by a Gaussian,[34,35]

$$\Delta f = \Delta f_0 \exp\left(- a \frac{r^2}{r_0^2} \right), \tag{5}$$

where r is the distance from the center of the quartz surface and r_0 is the radius of the bottom electrode deposited on the quartz crystal (3.3 mm).

In order to determine the shape constant *a* for the quartz crystal used here, we have measured the removal rate for different values of *r* by translating the sample under the impinging ion beam. The C_{60}^{+} ion beam is rastered across an area of about 100 x 100 μm^2. A typical result is shown in Figure **3-1**. From the least square fit of eq. (5) to the measured data (solid curves), we obtain a value of $a = 9.7$.

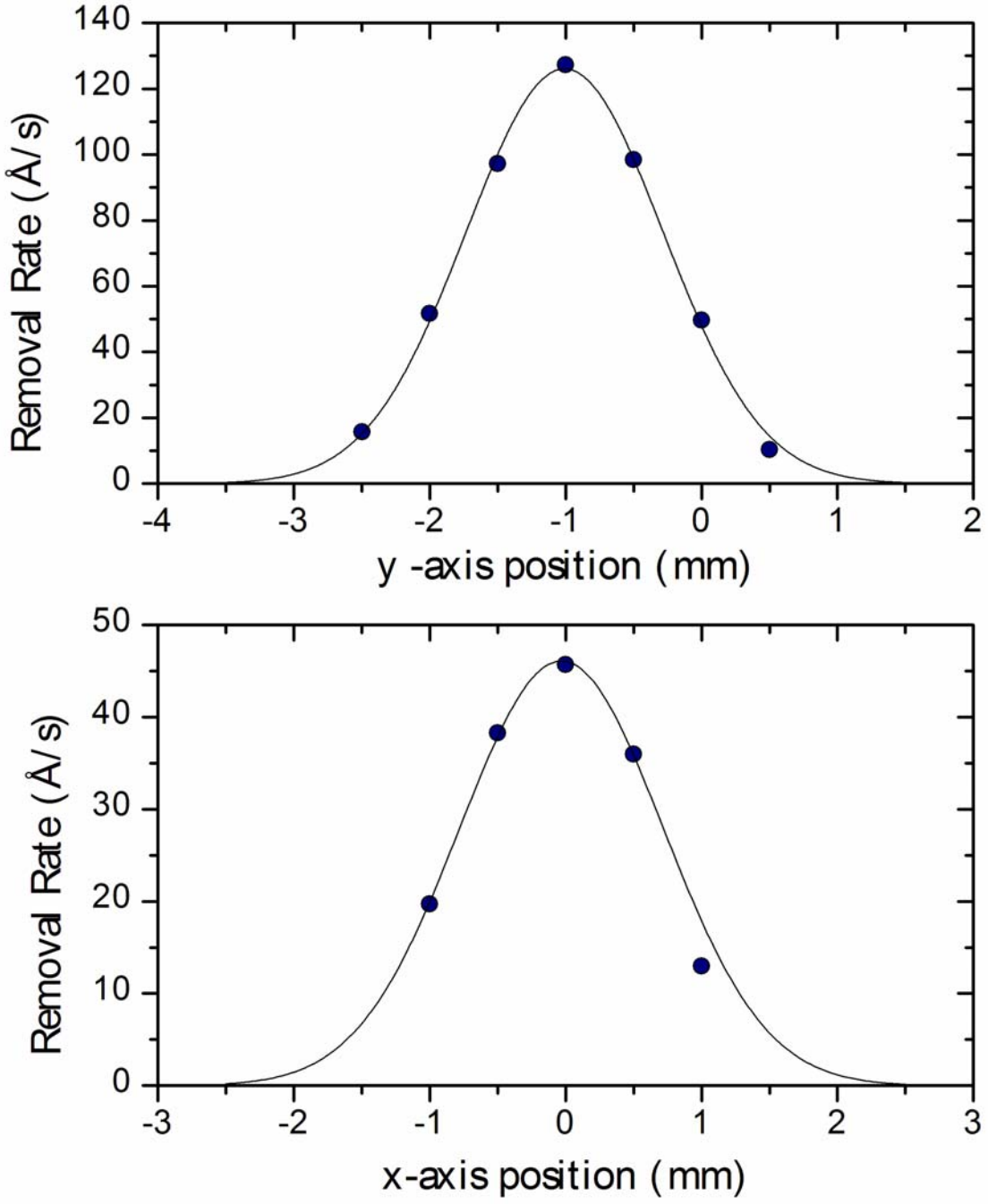

Figure **3-1**: Lateral dependence of the removal rate measured on a 500 nm silver film deposited on a quartz crystal bombarded by 20 keV C_{60}^{+} ions. The projectile ion beam was rastered across a surface area of 100 x 100 μm^2. The solid curve displays a Gaussian least square fit to the measured data.

If only a fraction of the quartz crystal surface is exposed to the impinging primary ion beam, the proportionality constant D in eq. (2) varies. Assuming, for simplicity, a radially symmetric beam profile of radius R centered on the surface, the resulting value D_R is determined by [35]

$$D_R = D_\infty \left[1 - \exp\left(- a \frac{R^2}{r_o^2} \right) \right]^{-1} . \tag{6}$$

To determine the yield, we are interested in the total mass loss Δm instead of changes in the areal mass density $\Delta m_a = \Delta m / \pi R^2$. Combining eqs. (2), (3) , and (6), we obtain

$$\Delta m = \Delta d \cdot \rho_f \cdot \frac{\pi R^2}{1 - \exp\left(- a \frac{R^2}{r_0^2} \right)} . \tag{7}$$

If the exposed surface area is kept small enough to ensure that $a R^2 / r_0^2 \le 1$, eq. (7) results in

$$\Delta m \cong \Delta d \cdot \rho_f \cdot \frac{\pi r_0^2}{a} , \tag{8}$$

where Δd is the removed layer thickness displayed by the QCM controller and ρ_f is the set film density value. The quantity $\pi r_0^2 / a$ depicts the sensitive surface area of the quartz crystal which in our case has a diameter of approximately 2 mm. The removal rate displayed by the QCM controller is therefore independent of the ion beam raster area as long as i) the total ion current delivered to the surface remains constant, ii) the raster area

is centered on the crystal and iii) the dimension of the exposed surface area does not exceed approximately 2 mm.

The resulting mass removal rate is then related to the flux of primary ions determined from the measured primary ion current. In order to obtain accurate results, the primary ion current must be corrected for ion bombardment-induced emission of charged secondary particles (ions and electrons) and is therefore independently measured using a Faraday cup. The total sputter yield is evaluated as the total number of atoms removed per impinging primary ion according to

$$Y_{tot} = \frac{\Delta m}{\Delta t} \cdot \frac{\cdot e \cdot N_A}{I_p \cdot m} = \frac{\Delta d}{\Delta t} \cdot \rho_f \cdot \frac{\pi r_0^2}{a} \cdot \frac{\cdot eN_A}{I_p m} \ , \tag{9}$$

where $\Delta d/\Delta t$ denotes the removal rate displayed by the QCM controller, e is the elementary charge, N_A is Avogradro's number, m is the atomic mass of the target material (here: silver) and I_p is the primary ion current.

3.3 Results and Discussion

3.3.1 Total Yields

The total number of silver atoms released per C_{60}^+ projectile impact onto the polycrystalline Ag surface with kinetic energies of 10, 15 and 20 keV is depicted in Table **3-1**. For comparison, corresponding data measured under bombardment with 15-keV Ga^+ are also included. It is seen that the yield induced by 15-keV C_{60}^+ is about 5-fold higher than that induced by Ga^+ projectiles of the same impact energy. The yield

measured under C_{60}^+ bombardment is found to depend linearly (R^2 of 0.9991) on the impact energy. At 20 keV, about 150 Ag atoms are released per C_{60} projectile, a value which is significantly larger than those typically achievable with atomic projectiles.

Table **3-1**: Total sputter yield of a polycrystalline Ag film deposited onto a quartz crystal under bombardment with C_{60}^+ and Ga^+ ions, respectively. The projectiles impinge onto the surface under an angle of 40 degrees with respect to the surface normal. Absolute values are given in atoms/projectile. For comparison, data obtained from molecular dynamics simulations of neutral C_{60} and Ga impact onto a (111) single crystal Ag surface have been included.[21] The accuracy of the experimental data is estimated to be of the order of ± 10 %, while the statistical uncertainty of the MD results is between 10 to 20 %.

		10-keV C_{60}^+	**15-keV C_{60}^+**	**20-keV C_{60}^+**	**15-keV Ga^+**
Experiment	absolute	47	98	144	20
	relative	1	2.1	3.1	0.42
MD Simulation	absolute	174	327 (0º) 218 (45º)	482	21
	relative	1	1.9	2.8	0.12

For comparison with recent MD computer simulations performed for the same projectiles impinging onto a (111) surface of an ideal Ag single crystal,[21] the MD data have been included in Table **3-1**. First, it is observed that the measured yield variations are in qualitative agreement with the simulation. This is particularly true for the impact energy dependence observed under C_{60} bombardment, where the experiment detects almost identical ratios as predicted from the simulations.[22] Comparing the absolute yield

values, we find the experimental C_{60} data to be about a factor of 3 lower than predicted, whereas the value measured for Ga is almost exactly reproduced by the simulation.

The observed difference between measured and calculated yields of Ag after C_{60}^{+} bombardment is not unexpected. The experiments were performed at an angle of incidence of 40º with respect to the surface normal while the calculations were performed at normal incidence. As shown in Table **3-1**, the yield is expected to be smaller for off-normal angles. Moreover, there is preliminary XPS evidence[36] and results from MD simulations[21] that suggest there is ~5% carbon incorporation into the surface region. This modification would have an unknown effect on the measured yield. Finally, we expect that intrinsic surface roughness associated with the evaporated Ag film will produce a lower yield than the perfectly flat {111} surface. For example, yield measurements from an Ag film deposited on a roughened Au QCM target (data not shown) were about 50% lower than those found for Ag deposited on a smooth Au QCM target (Table **3-1**). Some of these experimental uncertainties also apply to the Ga yield measurements, and we therefore view the close agreement between calculation and experiment in this case to be fortuitous. Hence, although there is uncertainty in the absolute sputtering yield, we believe the relative values reported in Table **3-1** as a function of incident energy are reliable.

3.3.2 Partial Yields

The partial yields of Ag atoms and Ag_n clusters are investigated using laser postionization of the respective sputtered neutral particles. More specifically, the average number of neutral species X desorbed per projectile impact is given by

$$Y\left(X^0\right) = Y_X \cdot \left(1 - \alpha_X^+ - \alpha_X^-\right), \tag{10}$$

where $\alpha_X^{+,-}$ denote the probability that the particle is emitted as a positive or negative secondary ion, respectively. For a clean Ag surface bombarded with various atomic projectile ions, it has been established[37-41] that these ionization probabilities are small compared to unity, thus making the neutral yield representative of the partial yield Y_X. If postionization conditions such as laser geometry and intensity are kept constant, the signal of a particular postionized species can be taken to represent the behavior of the partial yield of that species upon impact of different projectiles with different kinetic energies.

Laser postionization mass spectra of a polycrystalline Ag surface bombarded with 15 keV Ga^+ and 10, 15 and 20 keV C_{60}^+ ions are shown in Figure **3-2**. The vertical axis representing the signal intensity is plotted in arbitrary units which correspond to the digitized MCP output. In order to compare the partial yields of the different ejected species, the spectra have been normalized to the primary ion current, which is different depending upon the projectile and impact kinetic energy. In all four cases, neutral Ag, Ag_2 and Ag_3 particles are readily observed. In accordance with published literature data,[40,42] the cluster intensities are found to decrease by roughly one order of magnitude with each additional Ag atom. Note, however, that the postionization probabilities of the

different species are largely unknown, and the depicted intensities may not correctly reflect the yield ratio between different ejected species. The data are nevertheless useful to determine the yield variation of one particular species upon changing between different projectiles and impact kinetic energies.

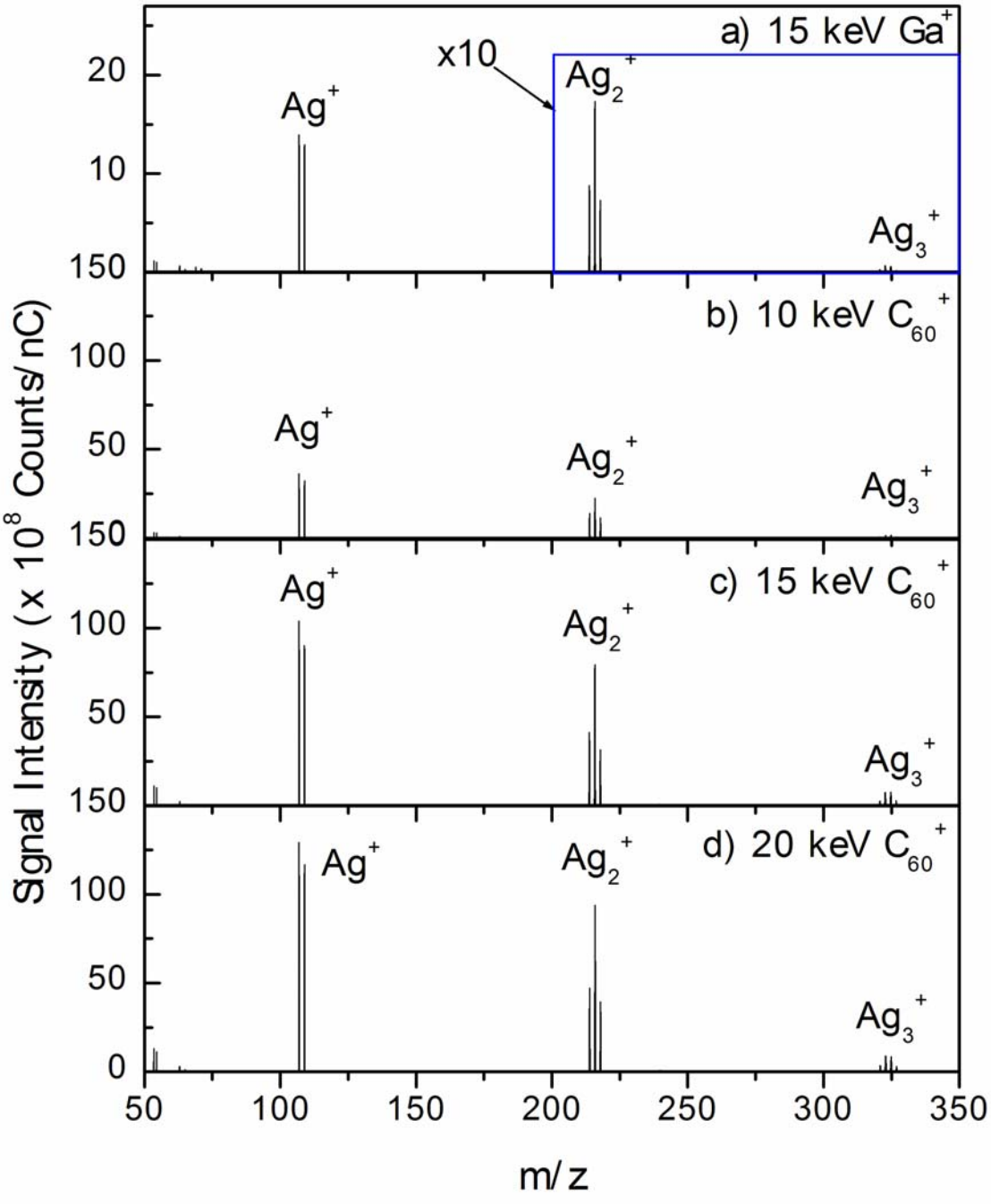

Figure **3-2**: Laser postionization spectra of neutral Ag atoms and clusters produced by a) 15 keV Ga^+ and b-d) 10, 15 and 20 keV C_{60}^+. The laser pulses used are 800 nm pulses at a peak power density of 3.0×10^{12} W/cm^2. The signal intensity has been normalized to the primary ion current.

From Figure **3-2**, it is obvious that the Ag monomer neutral yields from C_{60}^+ bombardment are significantly larger than those from Ga^+ bombardment and increase with increasing impact kinetic energy. This finding is expected in view of the total yield changes determined earlier. To quantitatively compare the enhancements, we examine relative changes in the Ag_n neutral and secondary ion yields obtained under C_{60}^+ bombardment as compared to those obtained under 15 keV Ga^+ bombardment. More specifically, the respective peaks in the ToF mass spectra are integrated over the entire isotopic abundance pattern, normalized to the primary ion current, and the ratio between the data obtained from C_{60}^+ and Ga^+ bombardment is calculated as an enhancement factor. The results are listed in Table **3-2** for 10, 15 and 20 keV impact energy. For comparison, the respective data obtained from the MD simulations[22] are also presented. As can be seen from the table, we find a qualitative agreement between the measured data and the prediction from the simulations. For instance, a 5.6-fold enhancement is measured for neutral Ag monomers between 15 keV C_{60}^+ and Ga^+ bombardment, whereas the predicted partial yield enhancement is 7-fold. Note that this value is also in very good agreement with the variation of the total sputter yield between 15 keV C_{60}^+ and 15 keV Ga^+ bombardment (Table **3-1**), verifying that the majority of the desorbed material is ejected in the form of neutral monomers.

Table **3-2**: Partial sputtering yield ratio of Ag_n^+ secondary ions (SIMS) and Ag_n secondary neutral particles (SNMS) emitted from a polycrystalline silver surface under irradiation with 10, 15 and 20 keV C_{60}^+ and 15 keV Ga^+ bombardment at 40º incidence. For comparison, data obtained from molecular dynamics simulations of neutral C_{60} and Ga normally incident onto a (111) single crystal silver surface have been included.[21] The uncertainty of the reported values is estimated to be of the order of 10 % for monomers, increasing to about a factor of two for trimers.

10 keV		Enhancement factor (Y_{C60}^+/Y_{Ga}^+)		
		Ag	Ag_2	Ag_3
Experiment (40°)	SIMS	0.7	3.5	11.9
	SNMS	2.0	2.7	5.1
MD Simulation (normal)		4.4	14	7

15 keV		Enhancement factor (Y_{C60}^+/Y_{Ga}^+)		
		Ag	Ag_2	Ag_3
Experiment (40°)	SIMS	3.8	10.5	25.1
	SNMS	5.6	9.1	23.5
MD Simulation (normal)		7	28	40

20 keV		Enhancement factor (Y_{C60}^+/Y_{Ga}^+)		
		Ag	Ag_2	Ag_3
Experiment (40°)	SIMS	4.5	18.9	48.7
	SNMS	7.9	10.6	28.5

The enhancements are more pronounced for ejected dimers and trimers, a finding which also agrees with the simulation results. The fact that the measured yield enhancement appears to be consistently smaller than that predicted by the simulation may in part be attributed to the relatively large statistical error of the simulated multimer yields (particularly for Ga^+ projectiles). On the other hand, it may also relate to the fact that the experiment detects only a narrow solid angle interval centered around the surface normal, while – again for statistical reasons – the simulation data refer to all ejected particles regardless of emission angle. The observed differences would therefore indicate a more forward-peaked angular distribution of sputtered multimers for Ga^+ than for C_{60}^+ projectiles. At present, the statistics of the simulations are not sufficient to allow a more elaborate discussion of that point.

An important observation in Table **3-2** is that the yield variations measured for neutral Ag_n species are almost identical to those obtained for Ag_n^+ secondary .ions. This finding indicates that the ionization probability α^+ of sputtered atoms and clusters is not significantly (i.e., by more than a factor of two) changed by the transition from Ga^+ to C_{60}^+ projectiles. The observed enhancements are therefore predominantly caused by a more efficient sputter removal of material which reflects both in increased total and partial sputtering yields obtained under C_{60}^+ cluster ion bombardment. This finding contrasts the results of a similar study performed for SF_5^+ projectile ions,[18] where the yield enhancement of Ag_n^+ secondary ions was found to be almost entirely due to an increased ionization probability. Apparently, the effect of the polyatomic nature of the projectile ion impinging onto an Ag surface is large for C_{60}^+ but smaller for SF_5^+ projectile ions.

3.3.3 Velocity Spectra

The velocity distributions of neutral particles are derived from their flight time between the sample surface and the laser postionization volume. The measured flight time distributions of Ag and Ag_2 emitted by bombardment with a) 15-keV Ga^+, b) 10-keV C_{60}^+ c) 15-keV C_{60}^+ and d) 20-keV C_{60}^+ projectile ions are displayed in Figure **3-3**. The data have been integrated over the entire isotope abundance distribution in the mass spectra. Due to the geometric setup, the distributions contain neutral species desorbing from the target over a wide polar angle interval extending up to ±30°.

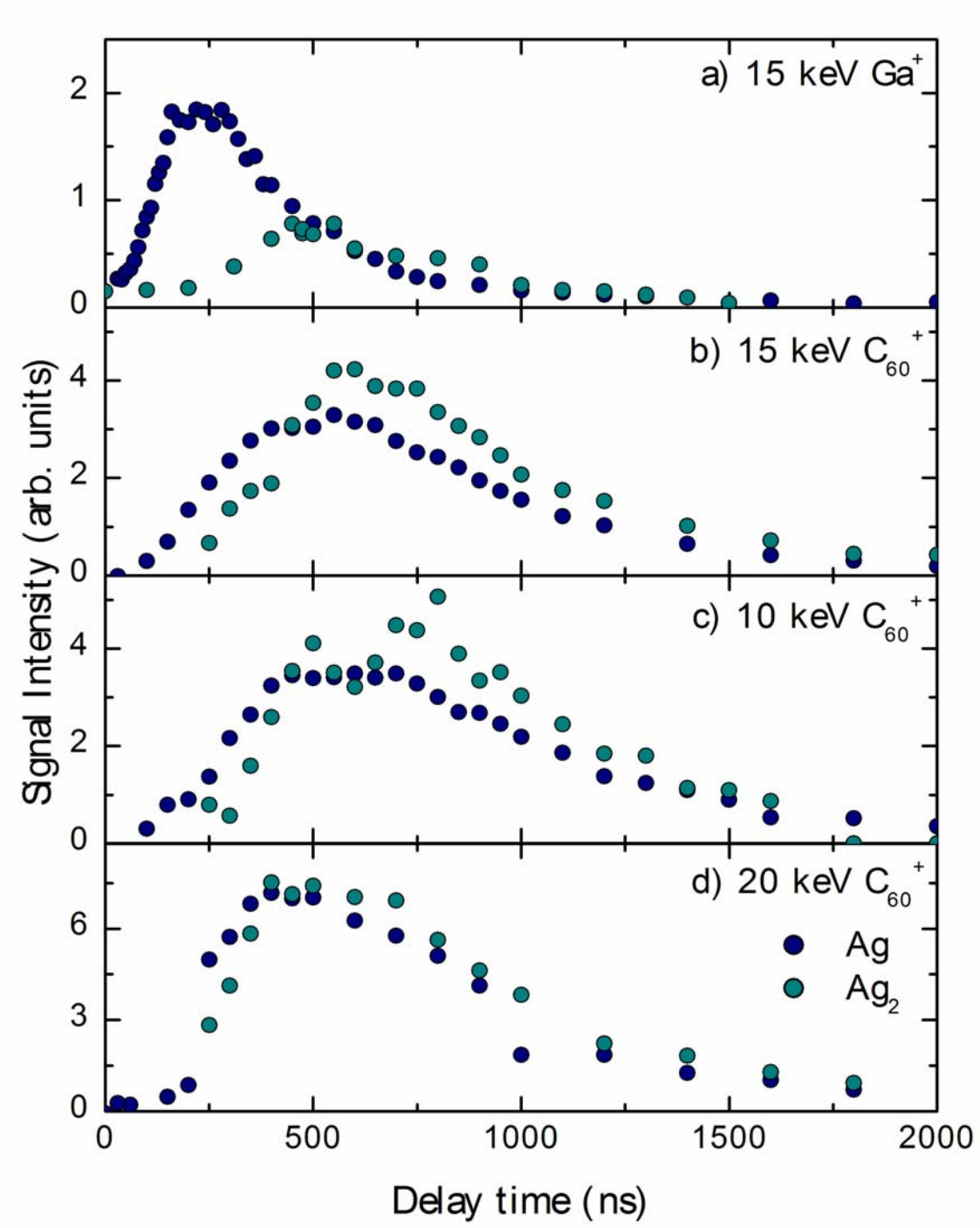

Figure **3-3**: Flight time distributions of neutral Ag atoms and Ag_2 dimers between the target surface and the postionization volume. The particles are desorbed from a polycrystalline Ag surface under a) 15 keV Ga^+ b) 15 keV C_{60}^+ c) 10 keV C_{60}^+ and d) 20 keV C_{60}^+ bombardment.

It is obvious that pronounced differences are found between atomic and cluster bombardment. Converting the data into emission velocity distributions by means of eq. (1), we obtain the results displayed in Figure **3-4**. The corresponding kinetic energy distributions are shown in Figure **3-5**. There are several interesting observations. The energy distributions of neutral Ag monomers induced by C_{60}^+ bombardment peak at lower values than those observed under Ga^+ bombardment. A similar shift towards lower kinetic energies under cluster impact has been reported earlier[20,43] and is well reproduced by the MD simulation.[22] This effect is qualitatively predicted by a simple thermal spike model of non linear sputtering originally published by *Sigmund and Claussen*.[44] However, the experimental data cannot be fitted to the prediction of ref. 44 as shown, for instance, as a solid line in Figure **3-5d**. Note that all kinetic energy distributions obtained under C_{60}^+ impact appear to be similar, indicating that the ejection process is largely independent of the primary ion impact energy.

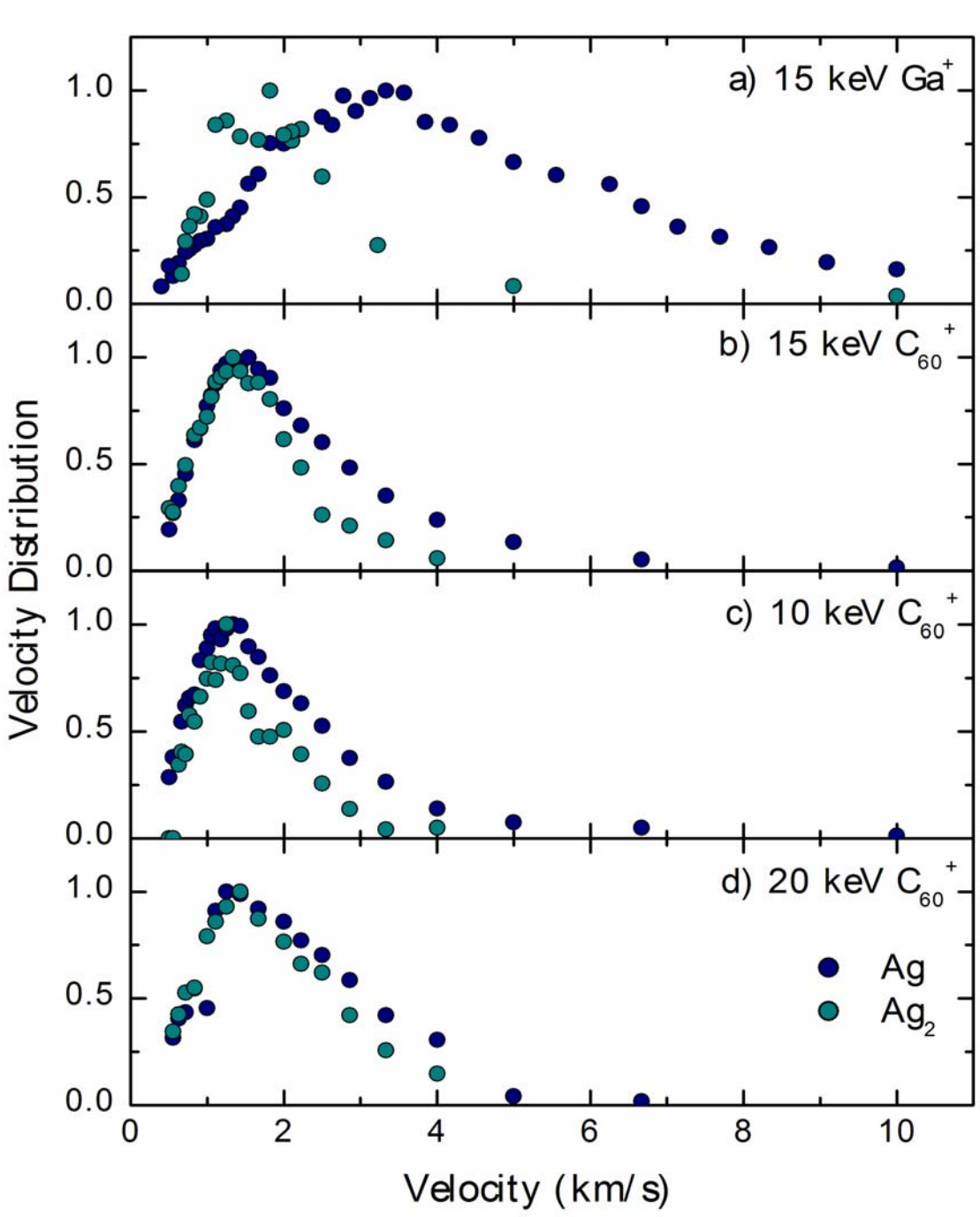

Figure **3-4**: Emission velocity distributions of neutral Ag atoms and Ag_2 dimers emitted from a polycrystalline Ag surface under a) 15 keV Ga^+ b) 15 keV C_{60}^+ c) 10 keV C_{60}^+ and d) 20 keV C_{60}^+ bombardment.

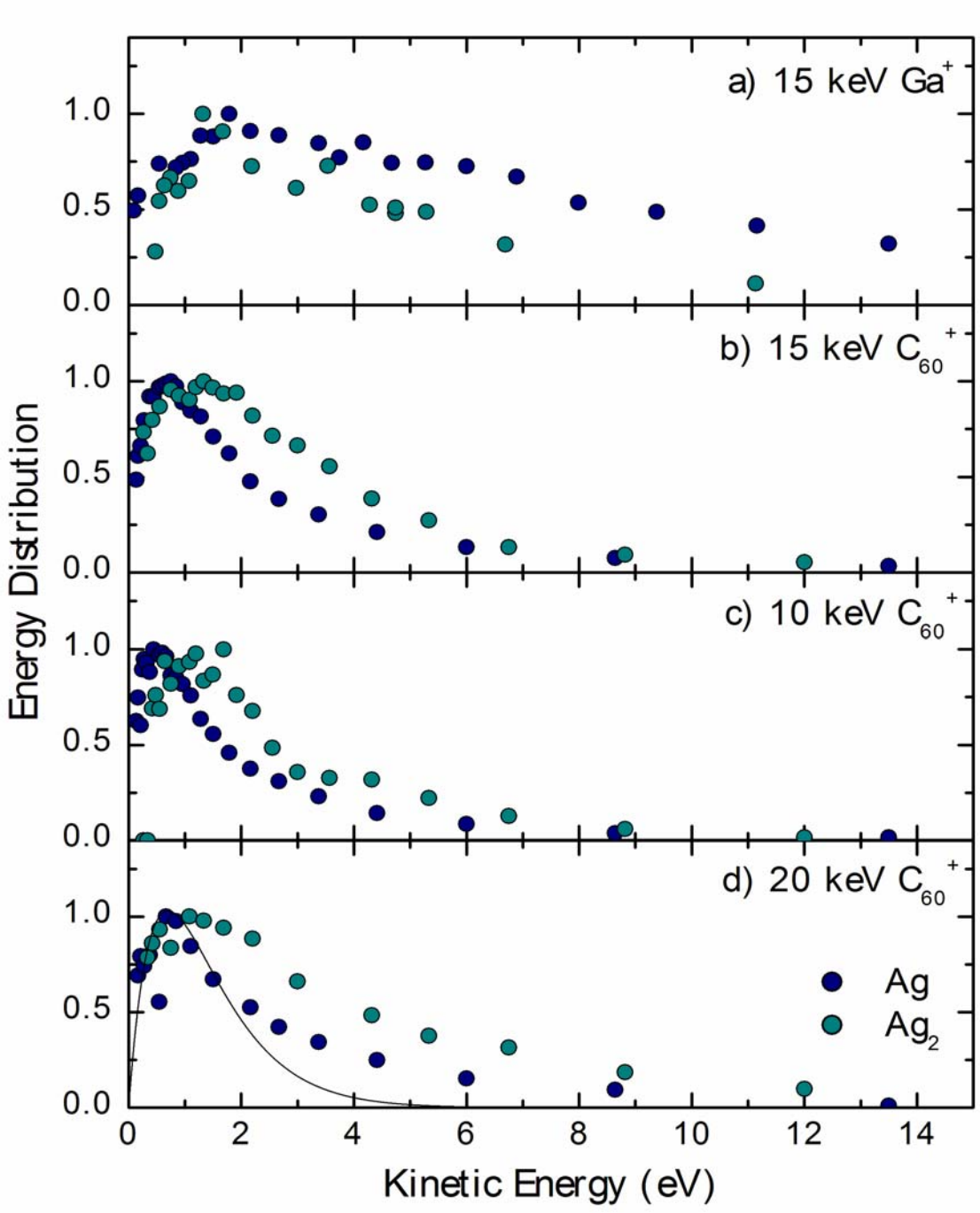

Figure **3-5**: Emission energy distributions of neutral Ag and Ag_2 emitted from a polycrystalline silver surface under a) 15 keV Ga^+ b) 15 keV C_{60}^+ c) 10 keV C_{60}^+ and d) 20 keV C_{60}^+ bombardment. The solid curve in d) depicts a Maxwell-Boltzmann energy distribution at T ~ 8000 K.

Probably the most interesting observation in Figure **3-5** concerns the emission energy spectrum of sputtered Ag_2. It is seen that the most probable kinetic energy is *higher* than that of Ag when bombarding with C_{60}. This finding is in pronounced contrast to the atomic projectile case, where the energy distributions of sputtered clusters peak at a lower emission energy than those of the monomers.[40,45-49] Since the effect is found both in the experiments and in the MD simulations, it appear to represent a unique, new feature of the sputtering processes initiated by cluster impact.

To elucidate the cause of the observed differences, we return to the data displayed in Figure **3-4**. Here, it is seen that the emission *velocity* distributions of Ag and Ag_2 observed under C_{60}^+ bombardment are surprisingly similar. A similar observation has been reported recently for the emission of In and In_2 from an In surface bombarded with Au atoms and clusters.[19] As discussed in ref. 19, the situation under cluster projectile bombardment appears to resemble the case of an adiabatic gas expansion from a pressurized volume through a nozzle. In this scenario, all emitted particles would have the same velocity, regardless of their mass. The particle ejection mechanism might then be viewed as a jet-like expansion of a superheated and super-dense gas being formed in the volume of the cascade induced by C_{60} impact. Due to the large pressure built up in the core of the impact zone, the surface is disrupted and material starts to expand quasi-freely into the vacuum. In fact, a similar picture has been used by *Urbassek* et al.[50,51] describing the particle emission in spikes induced by keV-atom bombardment of condensed rare gases. By analyzing the emission velocity field in the cascade volume and in the vicinity of the surface, their simulations clearly demonstrate a correlated, jet-like motion of ejected particles which would be consistent with a gas flow model[52] of the

ejection process. Comparing their visualization of impact events induced by 1-keV Ar impinging onto solid Ar (figures 1 and 5 in refs. 51 and 50, respectively) with those induced by 15-keV C_{60} impinging onto Ag{111} (figures 2 and 1 in refs. 22 and 21, respectively), it is probable that the nature of the emission mechanism must be similar in both cases. This notion is consistent with the fact that the kinetic energy spectrum of emitted atoms peaks at lower energies than predicted by linear cascade theory, but on the other hand cannot be fitted to a simple Maxwellian distribution.

3.4 Conclusions

Our results show that if C_{60}^+ projectiles are used to bombard a metal surface instead of isoenergetic Ga^+ ions, the yields of sputtered neutral species are enhanced by about the same amount as those of secondary ions. Moreover, the measured total sputter yield exhibits similar enhancement to that of sputtered neutral monomers. As a consequence, the secondary ion signal enhancement must be caused by a more efficient particle emission process rather than by a more efficient ionization of the ejected species. Moreover, neutral cluster species experience more enhancement than their corresponding monomers in a fashion also found for the secondary ions. The experimental results show that the neutral Ag species produced by C_{60}^+ bombardment leave the surface with kinetic energy distributions that maximize at much lower values than those observed under Ga^+ bombardment. In pronounced contrast to published data for atomic ion bombardment, we find that under C_{60} impact the emission *velocity* distributions of sputtered monomers and clusters are nearly identical.

The experimental findings are in at least qualitative agreement with recent MD simulations of the emission kinetics induced by C_{60} and Ga impact onto an Ag{111} surface. In total, the data indicate that the particle emission mechanism induced by the cluster projectile impact is significantly different from linear cascade sputtering typically encountered for atomic projectiles. Evaporation from thermal spikes, on the other hand, would lead to similar kinetic *energy* distributions of the emitted monomers and dimers and can therefore be ruled out as the predominant mechanism. The data seem to best be described by a jet expansion mechanism where a superheated, gasified volume of material in the core of the collision cascade builds up enough pressure to disrupt the surface and expand quasi-freely into the vacuum.

3.5 References

1. Castner, D.G., *Nature*, **2003,** *422***,** 129.

2. Winograd, N., *Anal.Chem.*, **2005,** *77***,** 142A.

3. Weibel, D., Wong, S., Lockyer, N., Blenkinsopp, P., Hill, R., Vickerman, J.C., *Anal. Chem.*, **2003,** *75***,** 1754.

4. Wong, S.C., Hill, R., Blenkinsopp, P., Lockyer, N.P., Weibel, D.E., Vickerman, J.C., *Appl. Surf. Sci.*, **2003,** *203-204***,** 219.

5. Davies, N., Weibel, D.E., Blenkinsopp, P., Lockyer, N., Hill, R., Vickerman, J.C., *Appl. Surf. Sci.*, **2003,** *203-204***,** 223.

6. Kersting, R., Hagenhoff, B., Kollmer, F., Mollers, R., Niehuis, E., *Appl. Surf. Sci.*, **2004,** *231-232***,** 261.

7. Cornett, D.S., Lee, T.D., Mahoney, J.F., *Rapid Commun. Mass Spectrom.*, **1994,** *8***,** 996.

8. Wagner, M. S., *Anal. Chem*, **2004,** *76***,** 1264.

9. Mahoney, C.M., Roberson, S., Gillen, G., *Anal. Chem.*, **2004,** *76***,** 3199.

10. Gillen, G., Fahey, A., *Appl. Surf. Sci.*, **2003,** *203-204***,** 209.

11. Wucher, A., Sun, S., Szakal, C., Winograd, N., *Anal. Chem.*, **2004,** *76***,** 7234.

12. Sostarecz, A.G., Sun, S., Szakal, C., Wucher, A., Winograd, N., *Appl. Surf. Sci.*, **2004,** *231-232***,** 179.

13. Sun, S., Wucher, A., Szakal, C., Winograd, N., *Appl. Phys. Lett.*, **2004,** *84***,** 5177.

14. Sun, S., Szakal, C., Roll, T., Mazarov, P., Wucher, A., Winograd, N., *Surf. Interface Anal.*, **2004,** *36***,** 1367.

15. Wucher, A., Sun, S., Szakal, C., Winograd, N., *Appl. Surf. Sci.*, **2004,** *231-232***,** 68.

16. Szakal, C., Sun, S., Wucher, A., Winograd, N., *Appl. Surf. Sci.*, **2004,** *231-232***,** 183.

17. Sostarecz, A. G., McQuaw, C. M., Wucher, A., Winograd, N., *Anal. Chem.*, **2004,** *76***,** 6651.

18. Ghalab, S., Staudt, C., Maksimov, S.E., Mazarov, P., Tugushev, V.I., Dzhemilev, N.Kh., Wucher, A., *Nucl. Instr. and Meth. B*, **2002,** *197***,** 43.

19. Samartsev, A.V., Duvenbeck, A., Wucher, A., *Phys. Rev. B* **2005,** 115147**.**

20. Andersen, H. H., In *Fundamental Processes in Sputtering of Atoms and Molecules (SPUT 92)*, 43 ed., Sigmund, P., Ed.; Det Kongelige Danske Videnskabernes Selskab: Copenhagen, **1993**; p. 127.

21. Postawa, Z., Czerwinsky, B., Szewczyk, M., Smiley, E.J., Winograd, N., Garrison, B.J., *J. Phys. Chem. B*, **2004,** *108***,** 7831.

22. Postawa, Z., Czerwinski, B., Szewczyk, M., Smiley, E.J., Winograd, N., Garrison, B.J., *Anal. Chem.*, **2003,** *75***,** 4402.

23. Kerford, M., Webb, R.P., *Nucl. Instr. and Meth. B*, **1999,** *153***,** 270.

24. Aoki, T. Seki, T., Matsuo, J., Insepov, Z., Yamada, I., *Mater. Chem. and Phys.*, **1998,** *54***,** 139.

25. Seki, T., Aoki, T., Tanomura, M., Matsuo, J., Yamada, I., *Mater. Chem. and Phys.*, **1998,** *54***,** 143.

26. Aderjan, R., Urbassek, H.M., *Nucl. Instr. and Meth. B*, **2000,** *164-165***,** 697.

27. Webb, R., Kerford, M., Way, A., Wilson, I., *Nucl. Instr. and Meth. B*, **1999,** *153***,** 284.

28. Braun, R.M., Blenkinsopp, P., Mullock, S.J., Corlett, C., Willey, K.F., Vickerman, J.C., Winograd, N., *Rapid Commun. Mass Spectrom.*, **1998,** *12***,** 1246.

29. Brummel, C.L., Willey, K.F., Vickerman, J.C., Winograd, N., *Int. J. Mass Spectrom. Ion Proc.*, **1995,** *143***,** 257.

30. Willey, K.F., Brummel, C.L., Winograd, N., *Chem. Phys. Lett.*, **1997,** *267***,** 359.

31. Wucher, A., Wahl, M., Oechsner, H., *Nucl. Instr. and Meth. B*, **1993,** *82***,** 337.

32. Sauerbrey, G. Zeitschrift für Physikalische Chemie, **1959,** 155**,** 206.

33. Kanazawa, K.K. Melroy, O.R., IBM Journal of Research and Development, **1993,** 37**,** 157.

34. Martin, B.A., Hager, H.E., J. Appl. Phys., **1989,** 65**,** 2630.

35. Doemling, M.F., Lin, B., Rueger, N.R., Oehrlein, G.S., Haring, R., Lee, Y.H., *J. Vac. Sci. Technol. A*, **2000,** *18***,** 232.

36. Preliminary data acquired by ULVAC-PHI Inc. using 10-keV C60+ projectiles (published at: http://www.phi.com)

37. Yu, M. L., In *Sputtering by Particle Bombardment III*, Behrisch, R., Wittmaack, K., Eds.; Springer: Berlin, **1991**; p. 91.

38. Meyer, S., Staudt, C., Wucher, A., *Appl. Surf. Sci.*, **2003,** *203-204***,** 48.

39. A. Wucher, R. Heinrich, C. Staudt, In *Secondary Ion Mass Spectrometry (SIMS XII),* Benninghoven, A., Bertrand, P., Migeon, N., Werner, H.W., Eds.; Elsevier Science: Amsterdam, **2000**; p. 143.

40. Wahl, M., Wucher, A., *Nucl. Instr. and Meth. B*, **1994,** *94***,** 36.

41. A. Wucher, W. Berthold, H. Oechsner, In *The Charge State of Sputtered Metal Clusters*, Benninghoven, A., Nihei, Y., Shimizu, R., Werner, H.W., Eds.; Wiley & Sons: **1994**; p. 100.

42. Franzreb, K., Fine, J., *Nucl. Instr. and Meth. B*, **1993,** *83***,** 266.

43. Szymonski, M., Bhattacharya, R.S., Overeijnder, H., de Vries, A.E., *J. Phys. D*, **1978,** *11***,** 751.

44. Sigmund, P., Claussen, C., *J. Appl. Phys.*, **1981,** *52***,** 990.

45. Bernhardt, F., Oechsner, H., Stumpe, E., *Nucl. Instr. and Meth. B*, **1976,** *132***,** 329.

46. Dembowski, J., Oechsner, H., Yamamura, Y., Urbassek, H.M., *Nucl. Instr. and Meth. B*, **1987,** *18***,** 464.

47. Brizzolara, R.A., Cooper, C.B., *Nucl. Instr. and Meth. B*, **1989,** *43***,** 136.

48. Cooper, C.B., Hamed, H.A., *Surf. Sci.*, **1984,** *143***,** 215.

49. Coon, S.R., Calaway, W.F., Burnett, J.W., Pellin, M.J., Gruen, D.M., Spiegel, D.R., White, J.M., *Surf. Sci.*, **1991,** *259***,** 275.

50. Waldeer, K.T., Urbassek, H.M., *Nucl. Instr. and Meth. B*, **1993,** *73***,** 14.

51. Urbassek, H.M., Waldeer, K.T., *Phys. Rev. Lett.*, **1991,** *67***,** 105.

52. Urbassek, H.M., *J. Phys. B*, **1987,** *20***,** 3105.

Chapter 4

Depth Profiling with a C_{60}^+ Ion Source

This chapter is adapted from: Sun, S., Szakal, C., Wucher, A., Winograd, N., *Appl. Phys. Lett.*, **2004**, *84*, 5177, with permission. Copyright is retained by the American Institute of Physics; Sun, S., Szakal, C., Roll, T., Mazarov, P., Wucher, A., Winograd, N., *Surf. Interf. Anal.*, **2004**, *36*, 1367, with permission. Copyright is retained by John Wiley and Sons Ltd.; Szakal, C., Sun, S., Wucher, A., Winograd, N., *Appl. Surf. Sci.*, **2004**, *231-232*, 183, and Wucher, A., Sun, S., Szakal, C., Winograd, N., *Appl. Surf. Sci*, **2004**, *231-232*, 68, with permission. Copyright is retained by Elsevier, B.V.; and Wucher, A., Sun, S., Szakal, C., Winograd, N., *Anal. Chem.*, **2004**, *76*, 7234, with permission. Copyright is retained by the American Chemical Society.

4.1 Introduction

We employ the 20 keV Buckminsterfullerene (C_{60}^+) ion source described in Chapter 2 to a series of fundamental experiments aimed toward elucidating the response of various sample types to bombardment by this projectile. Previous data using a 10 keV C_{60}^+ source showed that secondary ion intensities relative to those using atomic sources could be enhanced by two orders of magnitude, and that there was a propensity for the largest enhancements to be observed for the higher molecular weight species, especially from organic targets.

The sputtering of surfaces by C_{60}^+ is leading to new phenomena in SIMS. For example, topographic roughening and beam-induced sample charging are greatly reduced when compared to atomic bombardment. These attributes of the cluster source open the possibility of controllably eroding materials to produce a profile of chemical species with respect to depth within a sample. To examine the extent of the potential impact C_{60}^+ ion bombardment could have in this area of work, three sample systems of different types, all important to the present applications of SIMS, will be studied here in detail.

The first of these systems is a multilayer stack of alternating layers of 53 nm of Ni and 66 nm of Cr. To resolve these individual layers, interlayer resolution on the order of several nanometers is obviously required. Additionally, the underlying substrate should be reached, with minimal or no degradation in the interlayer resolving power. The results show that these conditions can be met using C_{60}^+ bombardment, largely because of the lack of formation of topographic features associated with atomic bombardment.

The second sample system utilizes a model polymer, poly (methyl methacrylate), PMMA, to determine if sputter depth profiling can be achieved for a molecular system with minimal or no fragmentation of targeted ions. Polymeric samples are less dense than metallic samples like Ni:Cr, and the ion/solid interactions are expected to be considerably different. Moreover, SIMS analysis often exhibits sample charging and primary beam-induced damage accumulation at the surface. The results show that there is reduced chemical damage from cluster sources and that depth resolution of polymer/substrate interfaces of about 14 nm can be attained.

The third sample system is a model biological compound, histamine, embedded within a water ice matrix to simulate the possibilities of depth profiling through freeze-

fractured single cells. Atomic sources damage biological molecules in these applications, and ion detection is problematic because of sample charging. Also, if depth profiling is possible for a model biological compound in a water ice matrix, it opens the door for obtaining three-dimensional chemical maps of cellular constituents – a natural extension from the two-dimensional imaging that is possible with atomic ion sources.

The analysis of each of these three different systems is now presented in detail.

4.2 Ni:Cr Depth Profiling System

4.2.1 Ni:Cr Background

The concept of sputter depth profiling with an ion beam has previously been used for monitoring the distributions of chemical signals from the surface into the bulk of the sample.[1] The depth resolution depends upon the nature of the ion beam utilized for eroding the sample, its incident energy, and the physical properties of the target. Atomic ion beams have several drawbacks that can limit the value of acquired depth profile data: 1) accumulation of chemical damage, 2) interlayer mixing, 3) topographic roughening, and 4) a sample orientation effect for crystalline metallic samples. Any combination of the above can lead to rapidly decreasing depth resolution as more material is eroded. Some of these effects of atomic bombardment can be alleviated by significantly reducing the incident energy, and/or using sample rotation and oxygen flooding. The latter strategies increase the difficulty of the experiment and their implementation would not be possible to integrate into molecular depth profiling of biological cells, where there can be

lateral heterogeneity. Additionally, ion beams with lower kinetic energies exhibit reduced erosion rates and are difficult to focus, rendering the beams non-practical for 2-D and eventual 3-D mass spectrometric imaging applications.

4.2.2 Ni:Cr Experimental

Details of this experiment can be found elsewhere.[2,3] Briefly, all experiments are performed on the BioTof time-of-flight secondary ion mass spectrometer.[4] The BioTof is fitted with a Ga^+ ion source[5] and the C_{60}^+ source described in Chapter 2. Secondary neutral mass spectrometry (SNMS), which involves postionization of sputtered neutrals by an 800 nm femtosecond Ti:sapphire laser system,[6] is utilized to eliminate the well-known SIMS matrix effect. Additionally, since greater than 98 % of sputtered particles are neutrals, and the postionization probability is high, this method results in a noticeable enhancement of signals at the detector.

A diagram of the Ni:Cr multilayer stack is provided in Figure **4-1**. Nine alternating layers of 53 nm Ni and 66 nm Cr are deposited onto a silicon substrate.[7] The outermost Ni layer is rinsed in hexane and methanol, and then nitrogen-dried. Depth profiling is carried out by a series of alternating data acquisition cycles and sputter erosion cycles, starting with data acquisition of the pre-bombarded surface. The same ion source is used for a particular acquisition/erosion cycle combination, with dc ion bombardment from an area of 400 x 400 μm^2 and data acquisition from a zoomed area of 50 x 50 μm^2 at the center of the larger crater. Recording spectra at considerably smaller areas than the erosion area yields data that is not influenced by crater edge effects.

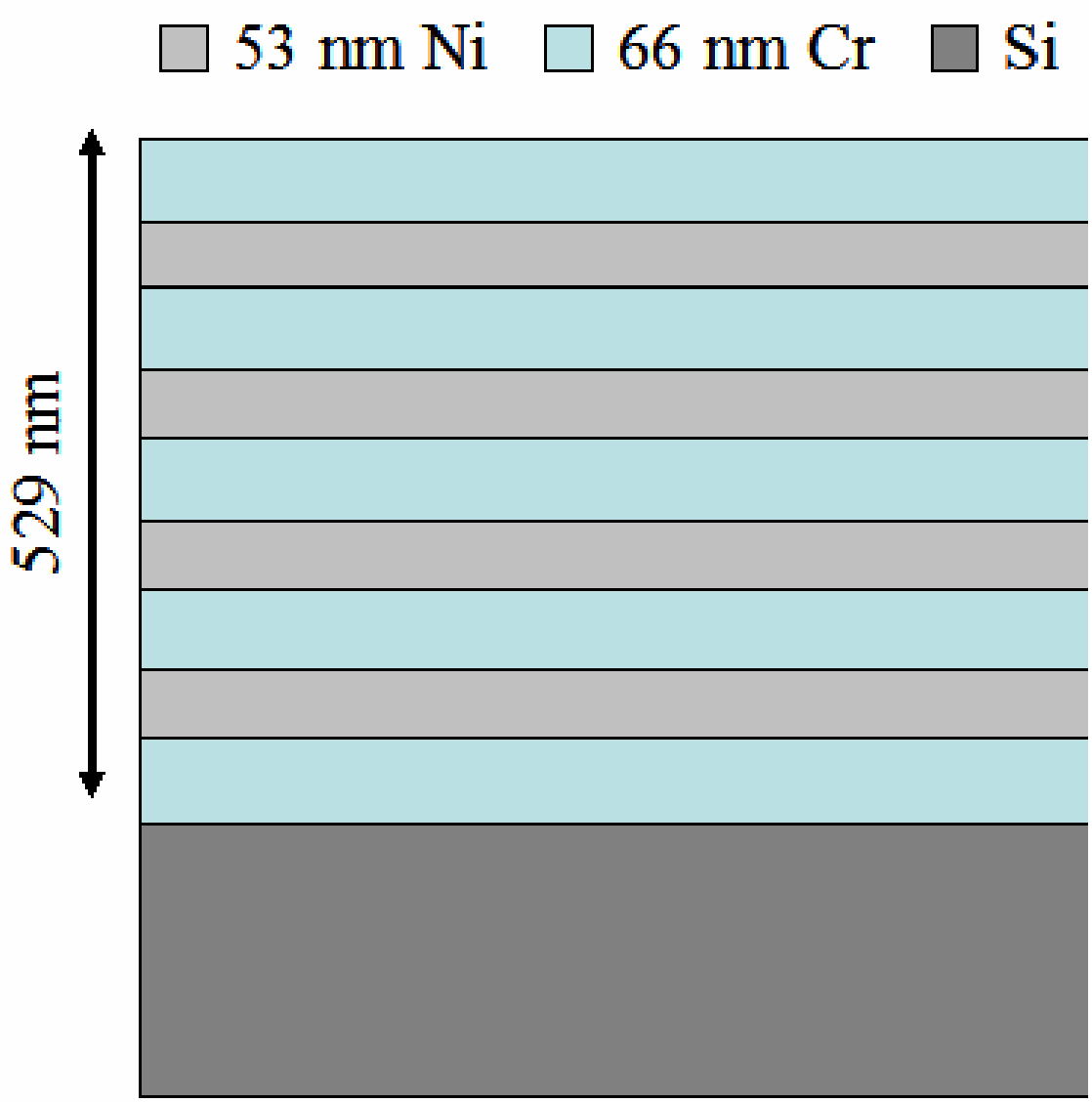

Figure **4-1**: Diagram of Ni:Cr alternating layer stack used in this study.

A Digital Instument Dimension 3100 atomic force microscope (AFM) is used in tapping mode at 1 Hz to study the topography of the eroded crater bottoms after depth profiling. However, it should be noted that some surface roughness via cumulative interlayer mixing and subsequent topographic roughening is expected with a polycrystalline sample such as this one. Different erosion rates in the different grains

lead to a mixture of sputter rates, which are more pronounced after several layers. Hence, some degree of resolving power is lost as a function of eroded depth.

4.2.3 Ni:Cr Results and Discussion

The measured signal intensity integrated over the ^{58}Ni, ^{52}Cr and $^{58}Ni^{52}Cr$ peaks in the mass spectrum of sputtered species as a function of the total ion bombardment time is shown in Figure **4-2**. Although 10, 15, and 20 keV C_{60}^{+} ions are able to profile through the stack and resolve all layers, only the 15 keV profile data are shown here as a representative example. Profile data with respect to energy can be found elsewhere.[3] Erosion with the C_{60}^{+} ion beam clearly resolves all individual layers. Moreover, the apparent depth resolution is maintained without significant degradation throughout the removal of the complete multilayer stack, a total thickness of 529 nm. The NiCr dimer species is only visible in the interfacial regions, since this species can only form when both Ni and Cr are present in the plume of the desorbed particles. These findings are in pronounced contrast with atomic ion erosion where only the first layer is resolved.

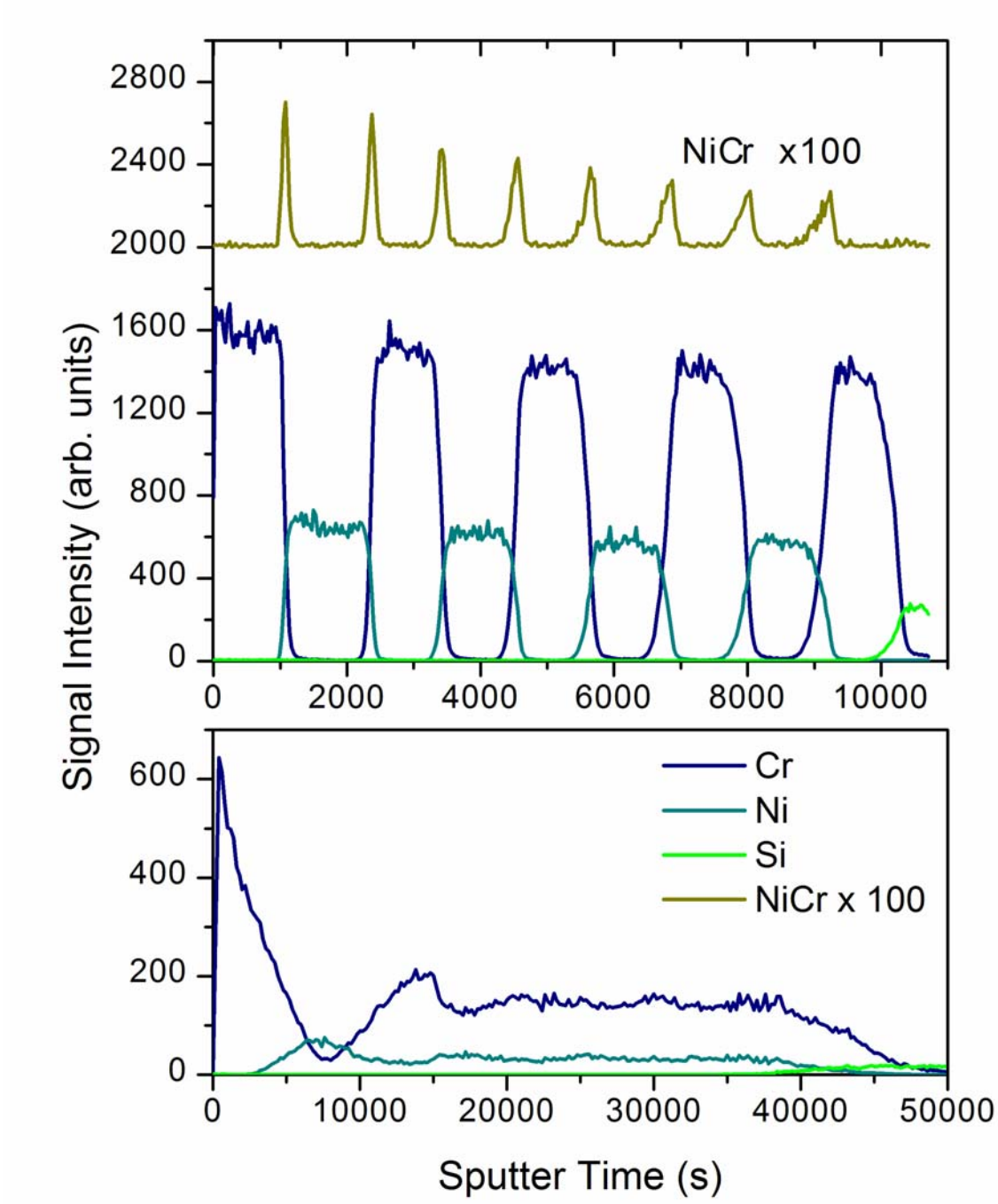

Figure **4-2**: Representative example of integrated signals of neutral atoms vs. sputter time for a nine layer Ni:Cr stack. The top panel shows the behavior under 15 keV C_{60}^{+} bombardment while the bottom panel shows the response to 15 keV Ga^{+} bombardment. The C_{60}^{+} bombardment-induced NiCr dimer signal is displaced upward by 2000 units to enhance visual clarity.

As illustrated in the C_{60}-induced depth profile, the signal intensity from Ni obtained in a Ni layer is about 3-fold lower than that of Cr obtained in a Cr layer. This effect is attributed to a lower postionization probability of the Ni atoms. The total sputtering yield of Ni and Cr layers can be calculated from the known layer thickness and the ion fluence needed to profile across an individual layer. The results show that the sputtering yield of Ni (190) is very similar to that of Cr (165) and that the yield induced by C_{60}^+ is about one order of magnitude higher than that from Ga^+ ion bombardment (~15). Sputtering yield values are reported as the number of metal atoms ejected per incident C_{60} molecule. The reported sputter yield numbers are consistent with similar values reported from polycrystalline Ag surfaces.[8]

In order to assess depth resolution, sputter time is converted to eroded depth by assuming a constant erosion rate throughout the complete multilayer stack. Depth scale calibration is performed by setting the sputtering time needed to remove the nominal total thickness of 529 nm to the point where the Si substrate signal has risen to 50% of its maximum value. Depth resolution is calculated from the interface widths, i.e., the intervals between the two points where the Cr and Ni signals reach 16% and 84% of their steady-state values. The depth resolution obtained at the first interface is 8.7 nm for 20-keV C_{60}^+ bombardment and improves to 5.9 nm and 5.3 nm for 15 and 10 keV bombardment, respectively.

The dependence of the observed interface width as a function of eroded depth is illustrated in Figure **4-3**. Although there is a slight degradation of depth resolution with increasing depth, its magnitude is much less dramatic than for atomic projectiles (represented by the Ga^+ data in Figure **4-2**). Similar interface width values are obtained

using the full widths at half maxima of the NiCr dimer peaks observed at each interface. These values are comparable to other Ni:Cr depth profiling experiments employing low kinetic energy bombardment and sample rotation.[9] For cluster beam depth profiling, a common argument is that the projectiles will dissociate upon collision with the target atoms and the initial kinetic energy will be split between each constituent atom of the impinging cluster. In that sense, the cluster bombardment appears to mimic the use of ultralow-energy atomic primary ion sources, which, as described in section **4.2.1** are known to minimize interlayer mixing effects and thereby provide improved depth resolution. However, additional factors contribute to the ability of cluster ions to maintain depth resolution throughout an eroded depth, such as the characteristics of the bombarded surface.

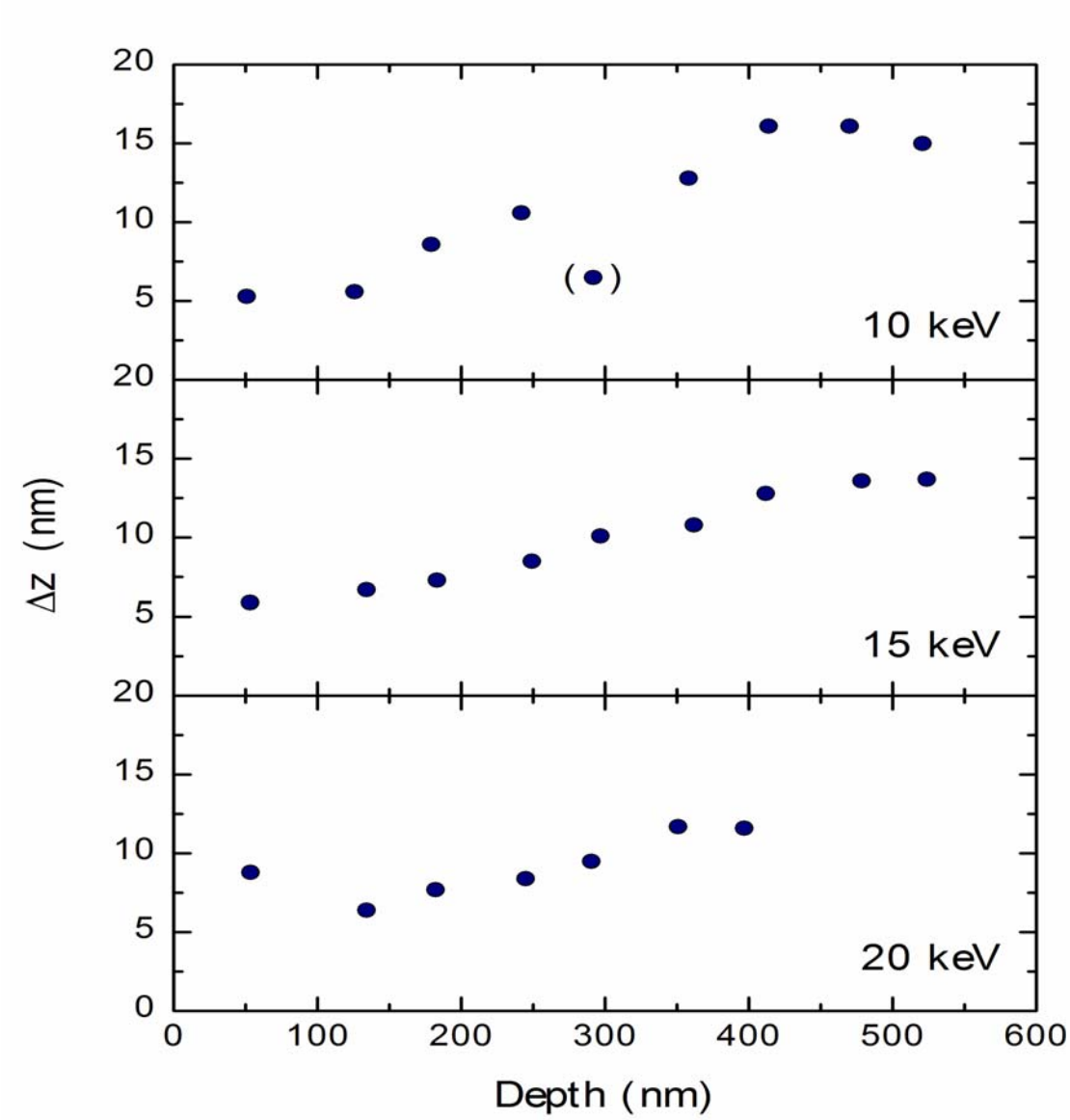

Figure **4-3**: Apparent 84%-16% interface widths as a function of eroded depth for C_{60}^{+} bombardment of 10, 15, and 20 keV energies.

Representative AFM images of the crater bottoms after sputter depth profiling through the Ni:Cr stack to the Si substrate for 20 keV C_{60}^{+} and 15 keV Ga^{+} are displayed in Figure **4-4**. From the image data, the roughness after prolonged 20 keV C_{60}^{+} bombardment is found to be 8 nm (rms). In contrast, Ga^{+} projectiles are found to produce

a much more pronounced topography. To illustrate this effect, the roughness evaluated from AFM images taken at different eroded depths by 15 keV Ga^+ bombardment is depicted in Figure **4-5**. The roughness increases linearly with increasing depth, as is expected if the topography is caused by lateral sputtering yield variations. This observation supports the notion that the large degradation of depth resolution observed for atomic projectile bombardment without sample rotation and oxygen flooding mostly arises from ion bombardment-induced topographic roughening.

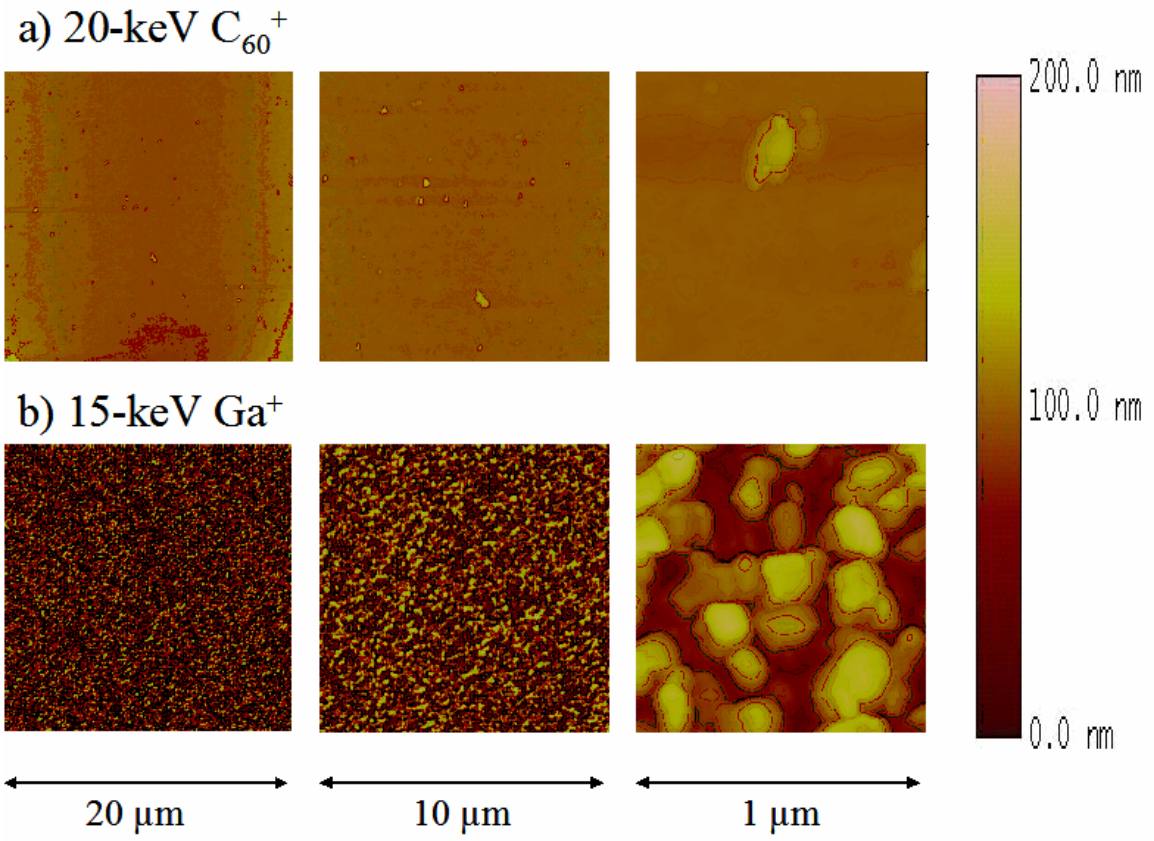

Figure **4-4**: Atomic force microscopy (AFM) images of the crater bottoms after depth profiling through the Ni:Cr stack to the Si substrate for a) 20 keV C_{60}^+ and b) 15 keV Ga^+ primary ions.

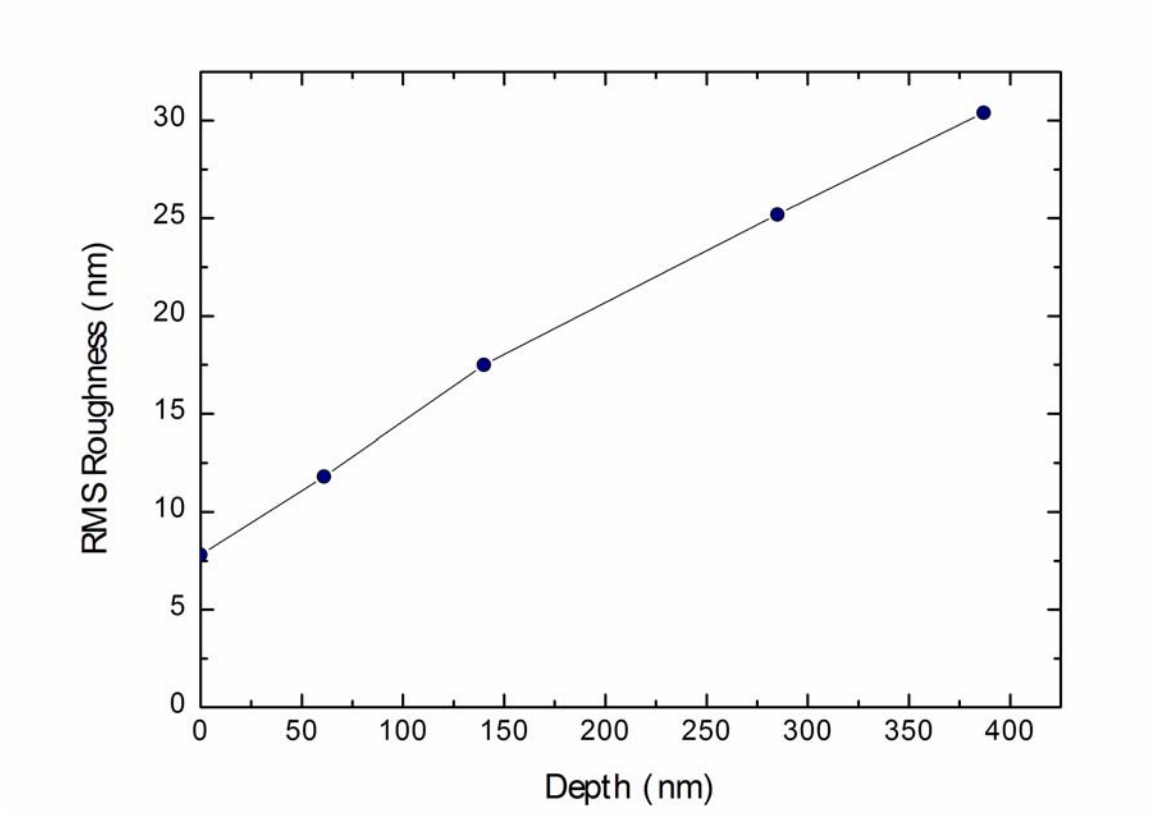

Figure **4-5**: The rms roughness evaluated from AFM images of the 15 keV Ga^+ bombarded crater bottoms within the Ni:Cr multilayer stack as a function of eroded depth.

On the original surface, an intrinsic roughness of ~ 7 nm (rms) is measured as shown in Figure **4-5**. It is of note that this value is practically identical to that determined with 20 keV C_{60}^+ bombardment after erosion through the Ni:Cr stack to the Si substrate. Apparently, the bombardment-induced roughening is virtually absent for cluster projectiles, indicating that the crystallite orientation dependence of the total sputtering yield is much less pronounced than under atomic projectile bombardment. This concept also extends itself to increasing size of the cluster projectile. The C_{60}^+ employed here yields 5.3 nm to 8.7 nm rms roughness values at the crater bottom, compared with

previous reports of 10 nm for SF_5^+ and 65 nm for O_2^+ projectiles.[10] These observations are clarified by molecular dynamics computer simulations that compare the sputtering processes induced by C_{60} and Ga projectiles, respectively.[11] The simulations show that the nature of the collision cascades generated under C_{60} impact are very different from those typically observed for atomic projectiles. Specifically, visualization by molecular dynamics simulations reveals that a C_{60} projectile impact generates a large volume of ejected material, and since the size of the C_{60} molecule is greater than the interatomic spacing of the metal atoms, crystallographic effects are lost.

The simulations also show that C_{60} exhibits a shorter penetration depth and causes less interlayer mixing than Ga. On the other hand, they also indicate that the average escape depth of sputtered particles is larger for C_{60} bombardment. Note that the escape depth limits the intrinsic depth resolution of the ToF SIMS/SNMS technique, which is induced by the (static) data acquisition process and therefore is independent of eroded depth. From the simulation results,[11] one would infer that a single C_{60} impact leads to the removal of material from a crater of about 5 nm lateral diameter and about 1.8 nm depth. This finding suggests that up to 7 atomic layers may contribute to the measured mass spectrometric signal, leading to an intrinsic depth resolution of the order of 1-2 nm. Comparing simulations performed at different impact energies of the C_{60} projectile, it is interesting to note that the lateral extension of the removed volume increases more strongly with increasing energy than its depth.[12] For the impact energy range explored here, the crater depth is estimated to vary between 1.6 nm at 10 keV to 2.1 nm at 20 keV.[12] This finding may explain why we do not observe large differences in depth resolution between these impact energies.

The observed depth resolution when using C_{60}^+ degrades only slightly with increasing depth. The AFM data clearly indicate that ion bombardment-induced topographic roughening can be ruled out as the source of this degradation, unlike the data from Ga^+ bombardment. Because the intrinsic depth resolution of at most 2 nm must be independent of eroded depth, we speculate that cumulative interlayer mixing from varying sputter rates in different crystal grains within the polycrystalline Ni:Cr stack is responsible for the trends observed in Figure **4-3**. Further analysis of these effects awaits results from more advanced computer simulations.

4.3 PMMA Depth Profling System

4.3.1 PMMA Background

When depth profiling molecular solids, the formation of chemical damage associated with the energetic impact of the primary projectile is a major difficulty. With atomic projectiles, organic surfaces are rapidly converted to a graphite-like material and all chemical information is lost to the mass spectrometer. The key parameter for depth profiling of organic species with an ion beam, then, is to generate sputter yields that are high enough to exceed the rate of damage accumulation, while enhancing desired secondary ion signals.

We choose PMMA, poly (methyl methacrylate), as a model polymer for studying the feasibility of using C_{60}^+ for *molecular* depth profiling. This molecule is specifically chosen because previous work by Fuoco and coworkers report the ability to profile

through PMMA films without significant damage accumulation using an SF_5^+ ion source.[13] The SF_5^+ ion is expected to exhibit behavior that is consistent with cluster beams, i.e., minimized damage accumulation, less interlayer mixing, etc. However, because its incident energy is spread only among six atoms (compared to sixty for buckminsterfullerene), it should also retain more atomic beam character, i.e., deposit its energy deeper within the sample, and provide lower depth resolution ability than a larger cluster projectile. The SF_5^+ primary ion has the additional property of implanted F atoms reacting with various carbon species to form volatile products, as mentioned in Chapter 3. This mechanism is often attributed to the enhancements observed with this projectile. Attaining molecular depth profiles with C_{60}^+, a projectile not expected to have a chemical effect from its incident carbon atoms, takes us one step closer to realizing the concept of probing molecular localization within layers of single biological cells, and therefore, extending the applications of SIMS to three-dimensional molecular maps of cellular constituents.

4.3.2 PMMA Experimental

Details of this experiment can be found elsewhere.[14] Briefly, SIMS data are acquired using the BioTof mass spectrometer mentioned in section **4.2.2**. A polished gold-coated QCM (quartz crystal microbalance) substrate is used as a support for the 25.8 nm of spin-coated PMMA, whose thickness was verified by ellipsometry.[15] A diagram of the sample system is provided in Figure **4-6**, showing substrate orientation with respect to the PMMA film and the 20 keV C_{60}^+ and 15 keV Ga^+ primary ion beams used in this

study. A detailed description of the modified QCM assembly used here, its application into the BioTof system, and theory behind its operation can be found in section **3.2.2**.

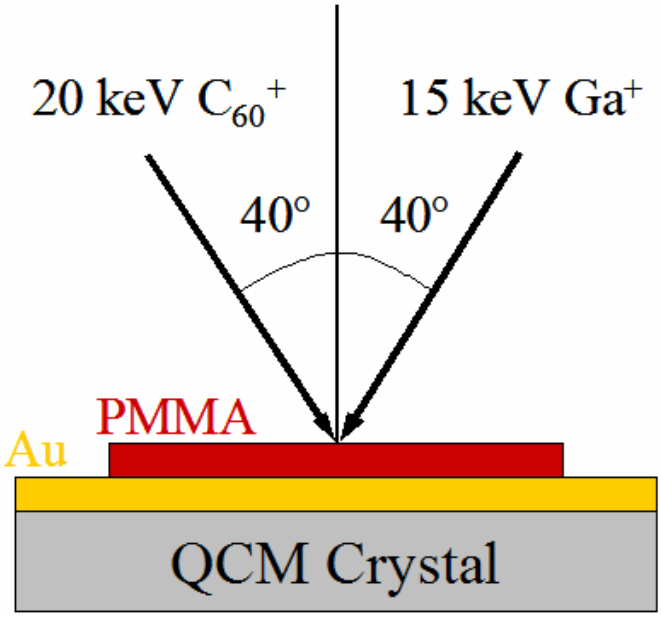

Figure **4-6**: Diagram of substrate orientation with respect to PMMA film and primary ion beams used in this study. The vertical line in the center of the diagram represents the surface normal.

Alternating data acquisition and sputter erosion cycles are employed as in the Ni:Cr experiment, with data acquisition at 1000 x 1000 μm^2 and sputter erosion at 2000 x 2000 μm^2 to avoid crater edge effects.

4.3.3 PMMA Results and Discussion

Raw intensity C_{60}^+ depth profile data for a characteristic PMMA fragment ion at m/z = 69 and the Au substrate ion at m/z = 197 is displayed in Figure **4-7**. The m/z 69 fragment ion is chemically stable and is monitored in order to directly compare to previous data acquired with a SF_5^+ ion source. The general features of this profile are

consistent with those reported using SF_5^+ projectiles,[13] and include 1) an initial signal decay, 2) a steady-state region of constant molecular ion signal, and 3) an interfacial region where molecular ion signals decrease and substrate signal increases as a function of depth.

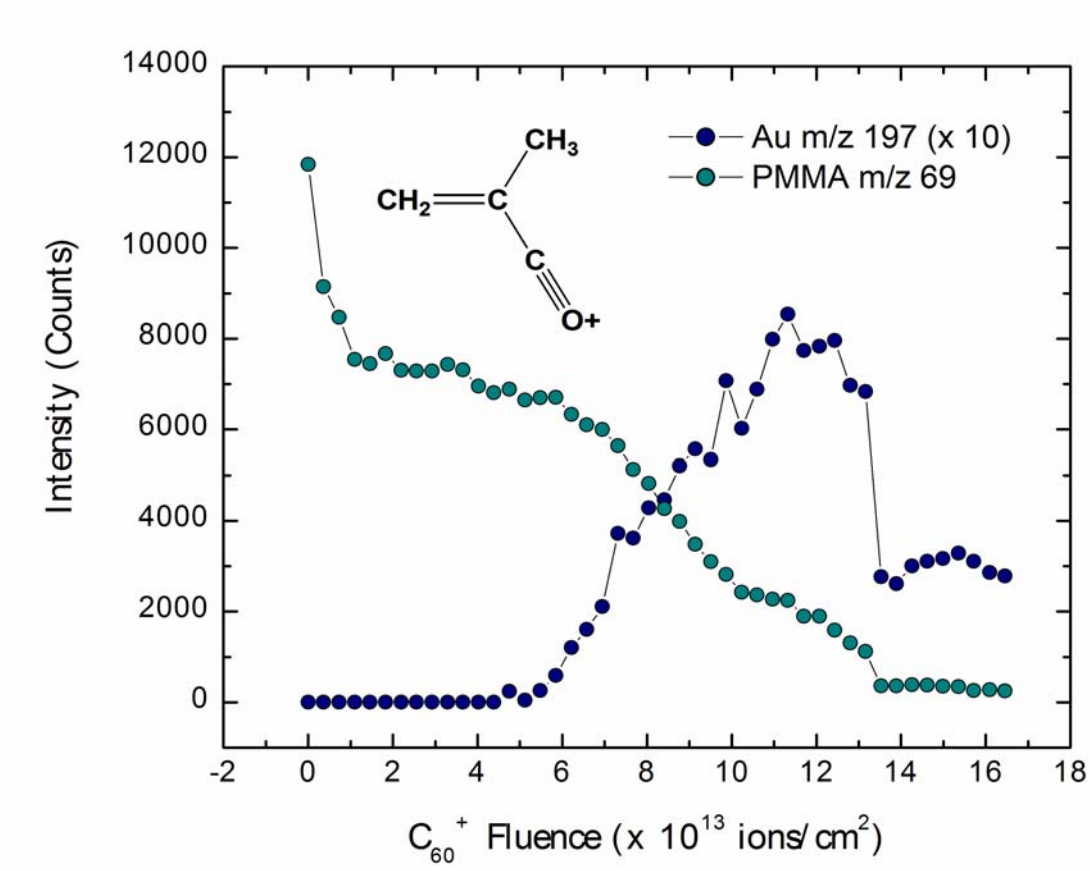

Figure **4-7**: C_{60}^+ raw intensity depth profile data for PMMA fragment ion at m/z = 69 (light green) and Au substrate ion at m/z = 197 (dark blue) with respect to primary ion beam fluence. The chemical structure represents the plotted PMMA fragment ion.

It should be noted that the signal drop of both intensities at a primary ion fluence of just over 1.3 x 10^{14} resulted from a random fluctuation of the C_{60}^+ ion current, and

does not impact the data interpretation. To further illustrate this point and to obtain a clearer picture of the monitored intensities versus eroded depth of the 25.8 nm PMMA film, the normalized PMMA fragment ion and Au substrate ion intensities are shown in Figure **4-8**. Normalization is computed by taking the ratio of a specific ion intensity to the sum of intensities at m/z 69 and m/z 197 at a specified point in time or depth. The x-axis is converted from sputter time, (or fluence), to depth by identifying the point where the substrate intensity reaches 50% of its maximum value and assigning it to the film depth of 25.8 nm. This corresponds to a C_{60}^+ sputter fluence of 8.5 x 10^{13} ions/cm^2, which equals a sputter rate through the PMMA film of 0.215 nm/s. As is shown in Figure **4-8**, the 84%-16% interface width[16] is determined to be 14 nm, once the assumption is made that a constant sputter rate is maintained throughout film erosion. In contrast, it is not possible to erode through the film using the 15 keV Ga^+ probe, nor was it possible for Fuoco and coworkers to erode through a PMMA film of comparable thickness using an Ar^+ primary ion beam.[13]

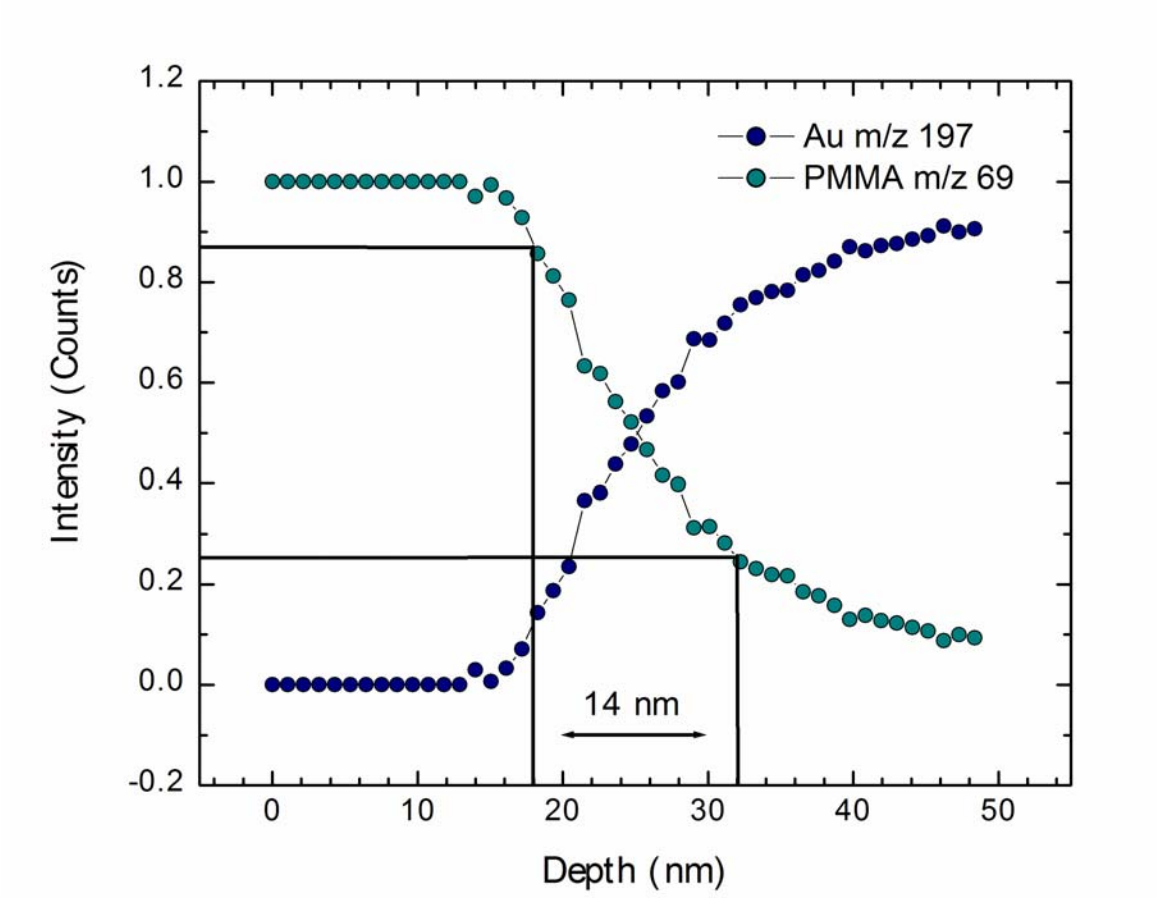

Figure **4-8**: C_{60}^{+} normalized intensity depth profile data for PMMA fragment ion at m/z = 69 (light green) and Au substrate ion at m/z = 197 (dark blue) with respect to eroded film depth. Normalization is computed by taking the ratio of a specific ion intensity to the sum of intensities at m/z 69 and m/z 197 at a specified point in time or depth. The interface width is determined at the 84%-16% intensity values of the PMMA fragment ion.

The QCM is employed to measure removal rates of the PMMA during 15 keV Ga^{+} and 20 keV C_{60}^{+} bombardment, in units of grams removed/cm^2. Absolute sputter yields for the PMMA cannot be determined since the polymer consists of homogeneously mixed, varying molecular weights of PMMA. However, once normalized to primary ion fluence, the ratio of mass of PMMA removed between the two sources can be

determined. We find that the ratio of the 20 keV C_{60}^+ to 15 keV Ga^+ PMMA sputter yields is 11.0 ± 0.6. In comparison to the referenced study of Fuoco and coworkers,[13] the ratio of 5.5 keV SF_5^+ to 5.5 keV Ar^+ PMMA sputter yields is 2.2 ± 0.8.

An interesting, albeit controversial, observation is that the secondary ion intensities for the m/z = 69 PMMA fragment ion are enhanced by about a factor of 40 for 20 keV C_{60}^+ over 15 keV Ga^+. Since the sputter yield is enhanced by just a factor of 11, this suggests that there can be up to a 4-fold increase in ionization efficiency when utilizing the C_{60}^+ source. This is an important finding since it isn't clear whether the spectral enhancements displayed under C_{60}^+ bombardment are due to sputtering enhancements (neutrals), or ionization enhancements (secondary ions). Certainly, the dominant force acting in favor of the C_{60}^+ is the size of the sputter crater and any subsequent sputtering mechanism that differs from the linear cascades that govern atomic ion bombardment. Anywhere from one to three orders of magnitude sputter yield enhancements have been measured, and although the secondary ion signals sometimes increase by additional factors, it appears that for this system, and the Ag system studied in Chapter 3, the sputter yield (neutral) enhancements are the main cause for the higher sensitivities.

Sample charging of insulating materials is a serious problem for many surface analysis techniques when the number of charged particles entering and leaving the sample is not identical. For an insulator, there is no mechanism for this charge to be removed and the potential on the target can reach the kinetic energy of the incident projectile. With C_{60}^+, charging appears to be greatly minimized and is often missing

from the analysis entirely. The yield of secondary ions appears to approach unity for C_{60}^{+} bombardment, minimizing problems due to sample charging.

4.4 Histamine in Water Ice Depth Profiling System

4.4.1 Histamine in Water Ice Background

We next extend the depth profiling protocol to water ice doped with histamine. This construct is an important model system for future bioimaging experiments as water ice is the matrix molecule of freeze-fractured biological cells. Histamine represents an important biomolecule whose detection could have implications for chemical mapping in mast cells. The goal is to examine the feasibility of molecular depth profiling using this more complex material.

4.4.2 Histamine in Water Ice Experimental

Details of this experiment can be found elsewhere.[17] Briefly, SIMS data are acquired using the BioTof mass spectrometer described in section **4.2.2**. Samples are prepared by depositing 2 μL of 1.6 mg/mL aqueous histamine solution onto a silver substrate previously cleaned with HNO_3, rinsed with deionized water and methanol, and nitrogen-dried. One of the benefits of histamine, besides its natural expression within mast cells, is that it dissolves completely in water. Upon being frozen, the histamine stays in solution, and could theoretically form a homogeneous sample target. The freezing method employed here is a "slow freeze" where the silver is already attached to

a copper block, and the entire block + sample system is immersed in liquid nitrogen. It is well-known that freezing aqueous samples in this fashion forms a highly crystalline form of water ice, and this non-uniform cooling can cause solute concentration gradients in what would otherwise be a homogeneous solution.[17] Two other freezing methods were used for experiments on this system, but are not pertinent to the scope of this chapter, and are described elsewhere.[17,18] The latter reference involves a freeze-fracture method similar to the way in which the biological cells are frozen in this laboratory.

Both 20 keV C_{60}^+ and 15 keV Ga^+ ions are used for profiling and data acquisition. The beams are tightly overlapped so as to strike the same area of the ice film, with erosion cycles using a dc beam rastered over an 800 x 800 μm^2 area and data acquisition within a 500 x 500 μm^2 area to avoid crater edge effects. Spectra cannot be acquired with the Ga^+ projectiles unless charge compensation is utilized, and to remain consistent, it is used for the C_{60}^+ projectiles – even though charging is not an issue with this source. Electrons with 20 eV energy and several hundred nA current are directed at the water ice/histamine sample in a pulsed mode during data acquisition and in a dc mode during sputter erosion.

4.4.3 Histamine in Water Ice Results and Discussion

After transferring the histamine/water ice sample to the pre-cooled sample stage, surface mass spectra are acquired with both 15 keV Ga^+ and 20 keV C_{60}^+ as illustrated in Figure **4-9**. Upon initial inspection of the mass spectra, it is observed that both projectiles generate a series of water ice peaks following the pattern $(H_2O)_nH^+$ that

dominate the spectral profile. The histamine $[M+H]^+$ ion at m/z 112 is clearly visible. However, two distinct features of the C_{60}^+ ion-induced spectra are 1) there is a several order of magnitude higher signal for all peaks in the spectrum relative to Ga^+ bombardment (note that the intensity is normalized to primary ion beam current and reported as counts/nC), and 2) there is a second series of peaks that propagate with water clusters based on the form $(H_2O)_nCH_3^+$. The presence of CH_3^+ in the cluster ion series arises either from fragments of the incident C_{60}^+ projectile or fragments of the dissolved histamine molecules as they recombine with H_2O clusters in the post-bombardment plume via a recombination mechanism. The first observation clearly implies that more material is being removed from C_{60}^+ impact than from Ga^+ bombardment, which is understandable given the macroscopic sputter craters with C_{60}^+ that were discussed earlier in this chapter. More detail on the sputtering of water ice and how C_{60}^+ is more than efficient at removing large amounts of water molecules from the ice matrix is discussed in Chapter 6.

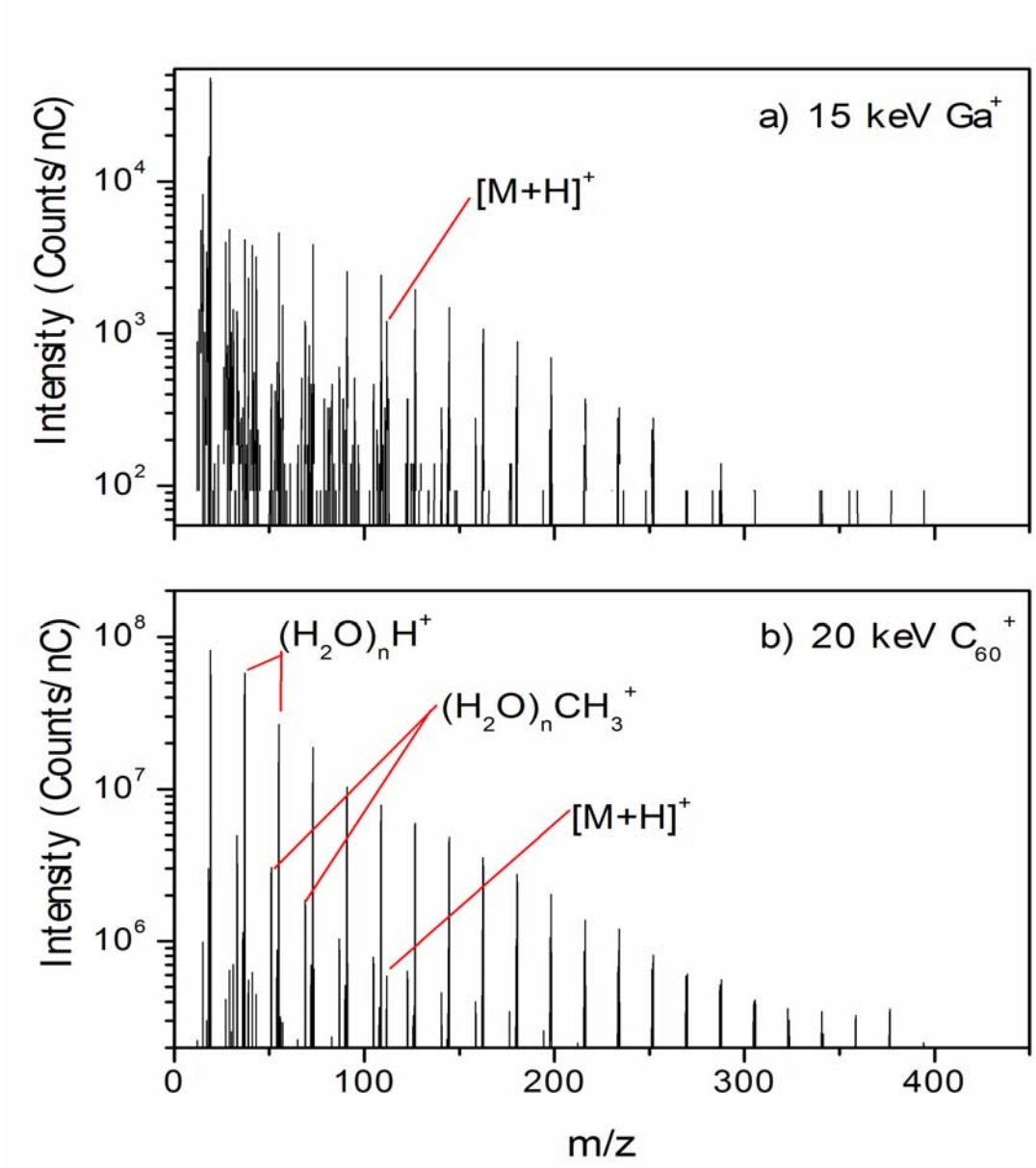

Figure **4-9**: Mass spectra from the surface of the histamine/water ice sample before sputtering, and normalized to primary ion beam currents. a) 15 keV Ga^+ bombardment-induced spectrum showing water ice clusters and the $[M+H]^+$ histamine peak at m/z = 112, b) 20 keV C_{60}^+ bombardment-induced spectrum showing water ice and methyl water ice clusters as well as the $[M+H]^+$ histamine peak.

To immediately test the integrity of the histamine molecular ion peak after C_{60}^+ sputter erosion, a dc beam fluence of 10^{13} ions/cm^2 was directed at the sample target. Since the ion sources were precisely overlapped, spectra could be taken with both sources within the eroded area. The resulting spectra for both ion sources are displayed in Figure **4-10**. The water ice cluster series decreases to the background in both spectra, and they both appear to be representations of almost pure histamine spectra. The molecular ion is present, as are the dimer, trimer, and specific fragments at m/z = 95 ($[M\text{-}NH_2]^+$), and at m/z 83-81 ($[M\text{-}CH_{0\text{-}2}NH_2]^+$). This change in the apparent dominating species from water ice to histamine suggests that there is a segregation of histamine near the surface and that the erosion cycle may indeed represent depth profiling of a concentration gradient of the analyte within a natural water ice environment. Additionally, both ion projectiles can be used to generate similarly meaningful spectra when the sample is controllably eroded with C_{60}^+ projectiles – not the case if Ga^+ projectiles are employed for sputter-depth profiling. This observation opens the possibility for using the better-focused Ga^+ probe for imaging applications: the C_{60}^+ can be used for sputter erosion, and data acquisition can be attained with either projectile, depending upon the lateral resolution required.

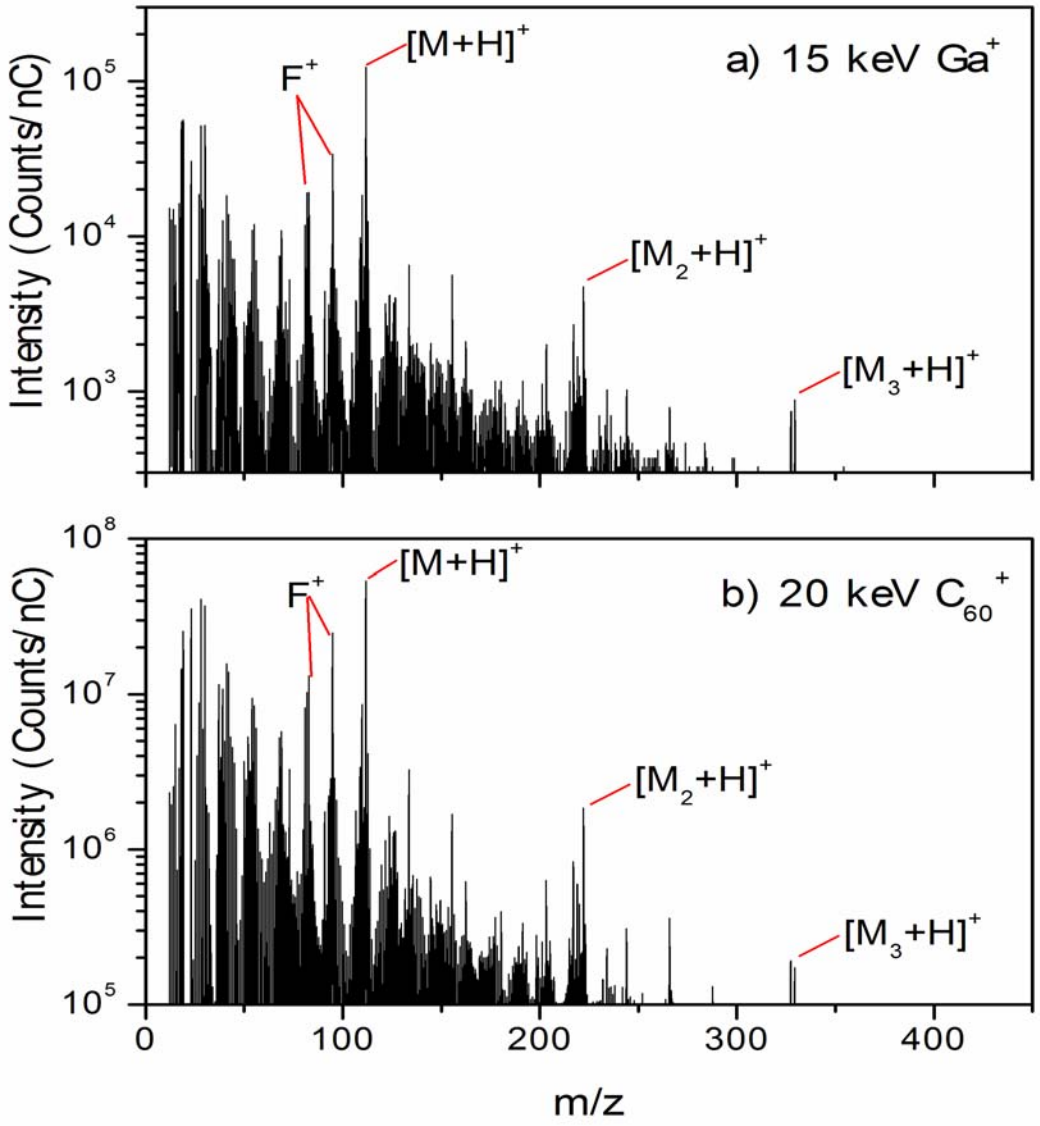

Figure **4-10**: Mass spectra of the histamine/water ice sample after 10^{13} ions/cm^2 C_{60}^+ dc sputter erosion. a) 15 keV Ga^+ bombardment-induced spectrum showing a decrease in the water ice clusters and a prominence of the $[M+H]^+$ histamine peak at m/z = 112 and other characteristic histamine ions, b) 20 keV C_{60}^+ bombardment-induced spectrum showing a decrease in the water ice clusters and a prominence of the $[M+H]^+$ histamine peak and other characteristic histamine ions.

If sputter erosion with C_{60}^+ is allowed to continue until a steady state signal is achieved at a fluence just over 10^{14} ions/cm^2, spectra with both projectiles from within the eroded area produce a water ice-dominated spectrum again, with histamine-specific molecular and fragment ions still present. As is shown in Figure **4-11**, it appears as though sputter erosion through the segregated histamine region is complete, and the spectra are indicative of the bulk histamine/water ice spectrum. Again, both projectiles produce spectra that are qualitatively similar with several orders of magnitude more signal from the C_{60}^+ bombardment-induced spectrum. The combination of the surface spectra, the spectra in the segregated histamine region, and the bulk spectra suggests that the data reflect a true depth profile of the analyte within the natural water ice matrix.

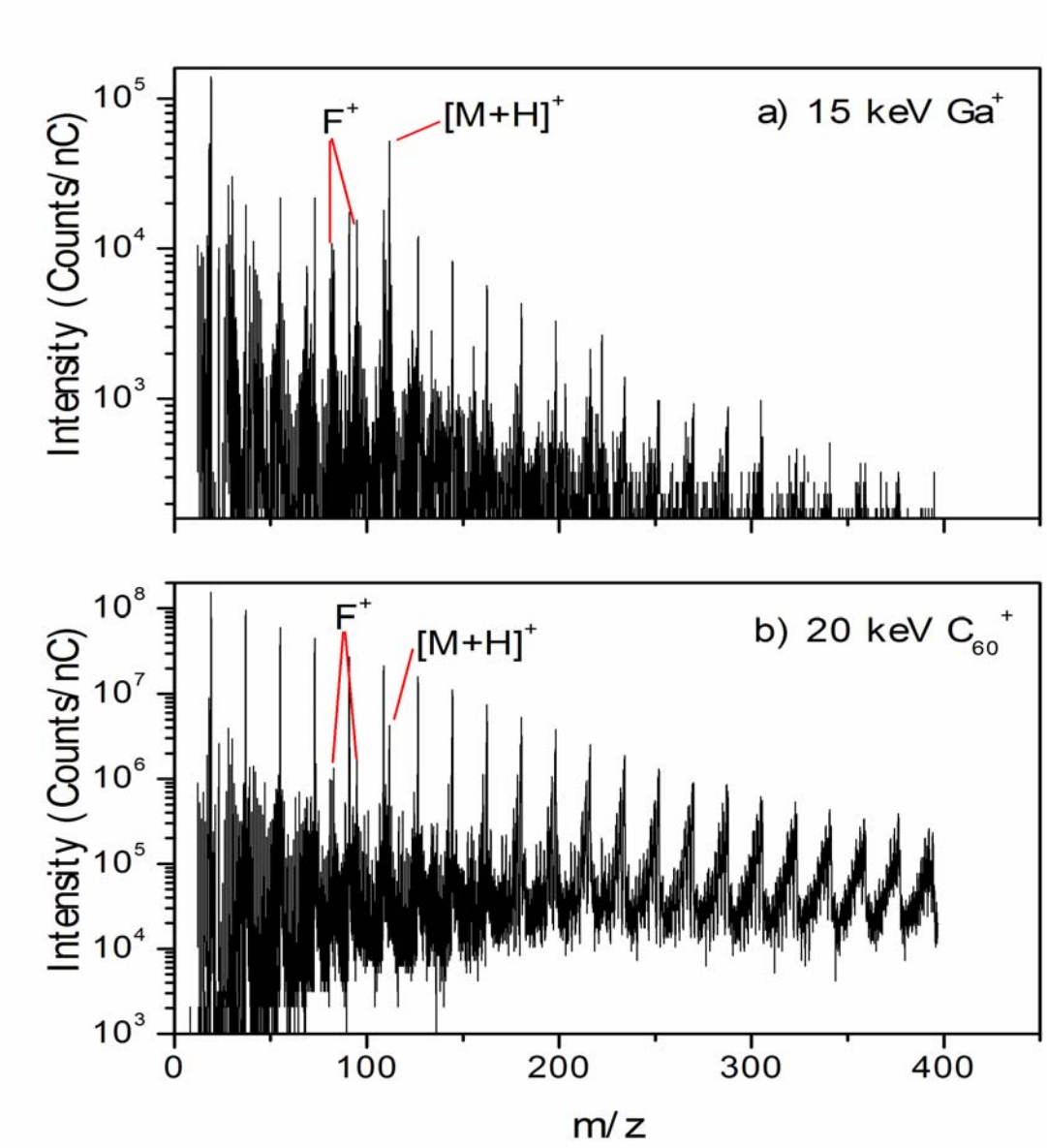

Figure **4-11**: Mass spectra of the histamine/water ice sample after 10^{14} ions/cm^2 C_{60}^+ dc sputter erosion. a) 15 keV Ga^+ bombardment-induced spectrum showing an equilibrium of water ice clusters and histamine-specific ions, b) 20 keV C_{60}^+ bombardment-induced spectrum showing an equilibrium of water ice clusters and histamine-specific ions.

A graphical representation of the water ice ion at m/z = 19 versus the histamine $[M+H]^+$ ion at m/z = 112 is displayed in Figure **4-12**. This plot of intensity versus C_{60}^+ dc ion fluence for both projectiles represents a depth profile through the histamine-segregated region within the water ice matrix. As sputter erosion proceeds, the surface spectrum that was dominated by water ice (presumably from adsorbed water from the sample transfer) becomes a histamine-rich portion of the sample (presumably from the sample preparation method). As the segregated region of solute is sputter-eroded, the equilibrium is eventually reached, but not before the histamine signal decreases with a measurable slope. Presumably, a balance of sputter yield and damage accumulation exists at this state in the profile. The water ice signal increases during this region of the profile, but does the decrease in histamine signal represent a true concentration gradient, or can there be ion beam-induced molecular damage?

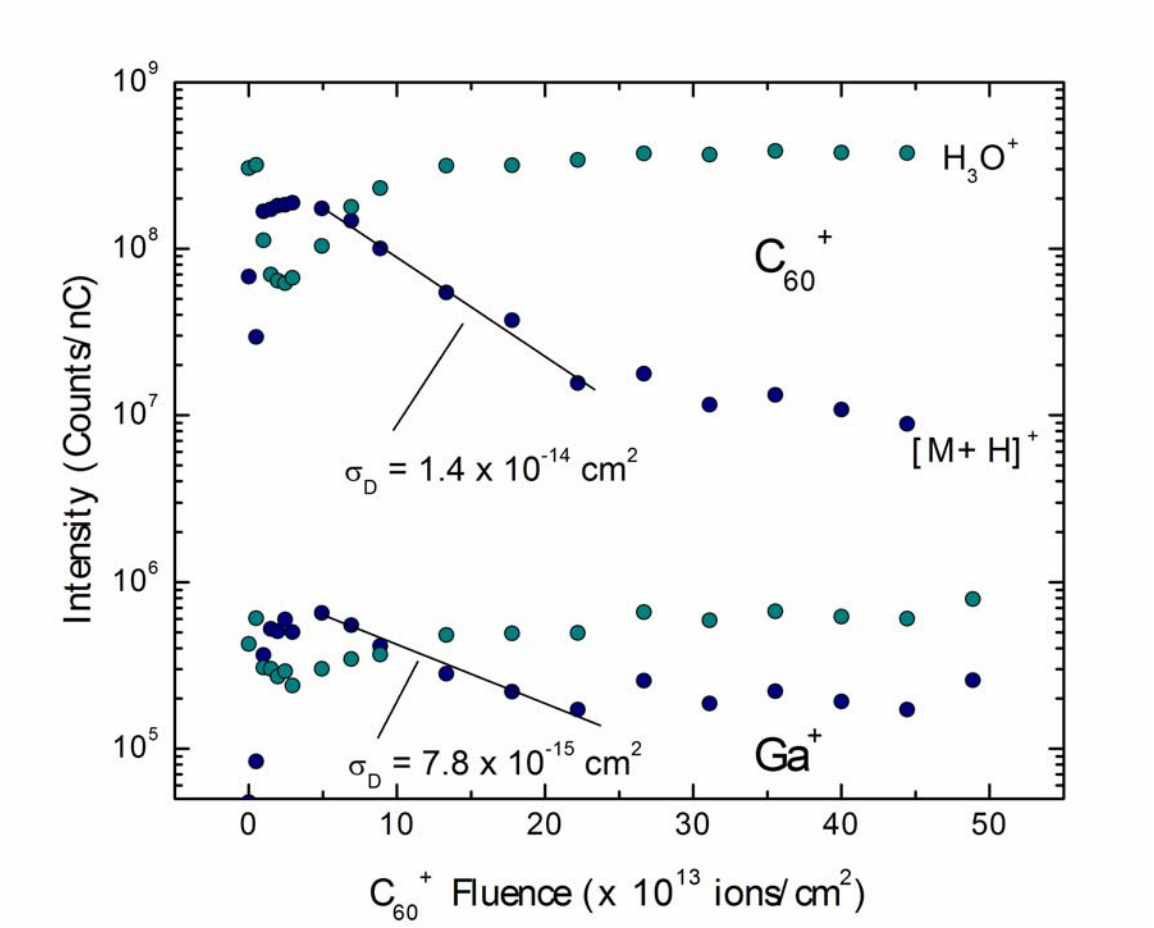

Figure **4-12**: Depth profiles for both 15 keV Ga^+ and 20 keV C_{60}^+ of the water ice H_3O^+ ion at m/z = 19 (light green) and the histamine $[M+H]^+$ ion at m/z = 112 (dark blue) versus C_{60}^+ dc ion fluence. Slopes of the histamine signal decrease for each projectile are displayed to illustrate the comparable data acquisition following a common projectile used for sputter erosion.

Support for the idea that the histamine signal decrease represents a true concentration gradient within the histamine/water ice sample is presented in Figure **4-13**. Here, a profile plot of the histamine molecular ion as well as all fragment ions during C_{60}^+ sputter erosion shows that all species of the molecule decrease at the same rate, indicating a lack of chemical damage. It is expected that if molecular damage was present, that the fragment ions would increase and/or the molecular ion would decrease at

a much faster rate than that of the fragment ions. Since these events do not occur during sputter erosion, we reason that the depth profile represents a true concentration gradient of the histamine molecule within the water ice matrix.

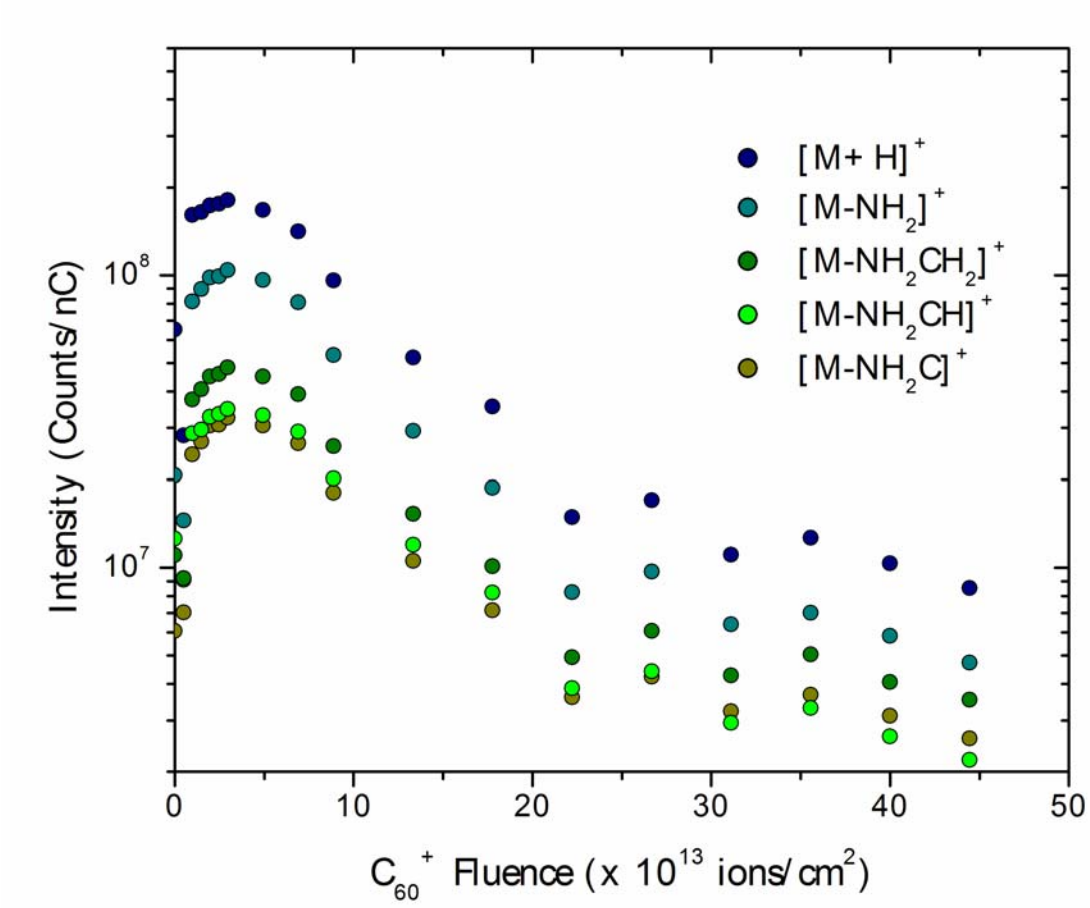

Figure **4-13**: Depth profile plot of C_{60}^+ bombardment-induced histamine molecular and fragment ions with respect to C_{60}^+ dc ion fluence. The similar negative slopes for all ions of the histamine molecule indicate a true concentration gradient of the analyte within the water ice matrix as opposed to signal degradation due to molecular damage.

The concept of the cluster projectile C_{60}^+ sputter-eroding a biological analyte within a water ice matrix is important for the application of depth profiling freeze-fractured cellular species. Just as important, though, is the ability to remove damage

created by an atomic ion projectile if its better lateral resolution is employed for imaging purposes. Figure **4-14** depicts a combination profile of alternating Ga^+ and C_{60}^+ sputter erosion cycles for the histamine/water ice sample after equilibrium has been reached. Notice that if Ga^+ is used as the sputter probe, the molecular ion of histamine decreases even though the water ice signal remains relatively constant. If sputter erosion is switched to the C_{60}^+, the histamine signal rises to an equilibrium value, suggesting removal of any Ga^+ bombardment-induced molecular damage. Switching back to Ga^+ sputter erosion leads to a subsequent decrease in the histamine signal again, at which point the C_{60}^+ can be used again to remove the accumulated damage and restore the spectra to equilibrium values.

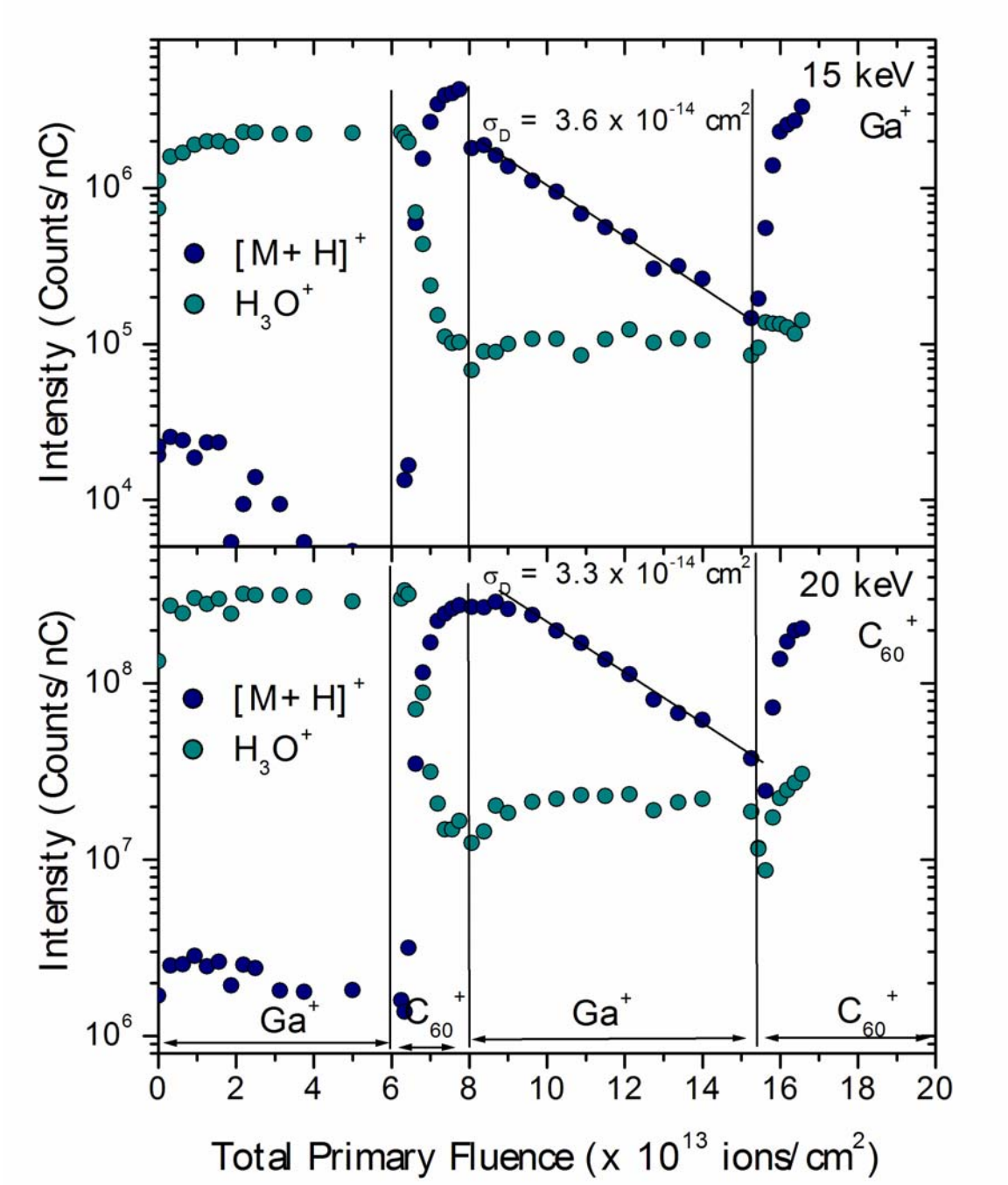

Figure **4-14**: Combined depth profile of histamine/water ice sample after initial equilibrium is reached. Areas are designated where each projectile is used as the sputter probe, and the cumulative fluence is denoted on the x-axis. The top panel is the corresponding Ga^+ bombardment-induced signals and the bottom panel is the corresponding C_{60}^+ bombardment-induced signals. The water ice H_3O^+ ion at m/z = 19 is light green and the histamine $[M+H]^+$ ion is dark blue.

4.5 Conclusions

This work demonstrates the feasibility of the C_{60}^+ ion source to controllably erode through three different sample systems and has provided support for the claim that this projectile can be used for SIMS depth profiling experiments. In contrast to atomic projectiles, prolonged C_{60}^+ bombardment does *not* lead to significant molecular damage accumulation, interlayer mixing, and topographic roughening. Therefore, adequate depth resolution as good as several nm can be achieved even as the eroded depth substantially increases. Additional benefits for using a cluster source such as C_{60}^+ instead of an atomic projectile to depth profile are the ability to obtain the best depth resolution *without* sample rotation and/or oxygen flooding and a lack of sample charging that has been associated with earlier studies of insulating films. The combination of much less beam-induced topographic roughening/interlayer mixing with the higher sputter yields due to C_{60}^+ bombardment make for higher sputter erosion rates and much more useable signal for the SIMS spectra. The highly energetic impact parameters employed here compare with the best depth resolutions achieved with low-energy atomic projectiles for inorganic multilayer samples, but offer the additional benefit of a well-focused beam for imaging applications. These fundamental experiments open the possibility of using the C_{60}^+ projectile for three-dimensional depth profiling experiments, and the dual-beam analysis reported here suggests that the C_{60}^+ probe can be used for sputter erosion while the better-focused Ga^+ or Au_n^+ projectiles can be used for data acquisition.

4.6 References

1. Dowsett, M.G., *Appl. Surf. Sci.*, **2003**, *203-204*, 5.

2. Sun, S., Wucher, A., Szakal, C., Winograd, N., *Appl. Phys. Lett.*, **2004**, *84*, 5177.

3. Sun, S., Szakal, C., Roll, T., Mazarov, P., Wucher, A., Winograd, N., *Surf. Interf. Anal.*, **2004**, *36*, 13667.

4. Braun, R.M., Blenkinsopp, P., Mullock, S.J., Corlett, C., Willey, K.F., Vickerman, J.C., Winograd, N., *Rapid Comm. Mass Spectrom.*, **1998**, *12*, 1246.

5. Weibel, D., Wong, S., Lockyer, N., Blenkinsopp, P., Hill, R., Vickerman, J., *Anal. Chem.*, **2003**, *75*, 1754.

6. Willey, K.F., Vorsa, V., Braun, R.M., Winograd, N., *Rapid Comm. Mass Spectrom.*, **1998**, *12*, 1253.

7. Ni:Cr multilayer stack sample similar to the NIST standard reference material SRM 2135a supplied by Greg Gillen from NIST.

8. Sun, S., Szakal, C., Wucher, A., Winograd, N., *J. Am. Soc. Mass Spectrom.*, **2005,** *16,* 1677.

9. Hofmann, S., Zalar, A., Cirlin, E.H., Vajo, J.J., Mathieu, J.H., Panjan, P., *Surf. Interf. Anal.*, **1993**, *20*, 621.

10. Gillen, G., Walker, M., Thompson, P., Bennett, J., *J. Vac. Sci. Technol. A*, **2000**, *18*, 503.

11. Postawa, Z., Czerwinski, B., Szewczyk, M., Smiley, E.J., Winograd, N., Garrison, B.J., *Anal. Chem.*, **2003**, *75*, 4402.

12. Postawa, Z., Czerwinski, B., Szewczyk, M., Smiley, E.J., Winograd, N., Garrison, B.J., *J. Phys. Chem. B.*, **2004**, *108*, 7831.

13. Fuoco, E.R., Gillen, G., Wijesundara, M.B.J., Wallace, W.E., Hanley, L., *J. Phys. Chem. B*, **2001**, *105*, 3950.

14. Szakal, C., Sun, S., Wucher, A., Winograd, N., *Appl. Surf. Sci.*, **2004**, *231-232*, 183.

15. We thank Matt Dixon for spin-coating the PMMA and for ellipsometry depth verification data.

16. Wagner, M.S., *Anal. Chem.*, **2005**, *77*, 911.

17. Wucher, A., Sun, S., Szakal, C., Winograd, N., *Anal. Chem.*, **2004**, *76*, 7234.

18. Sun, S., Ph.D. Thesis, *The Pennsylvania State University*, **2004**, 115.

Chapter 5

Secondary Ion Emission from Water Ice

This chapter is adapted from: Wojciechowski, I.A., Sun, S., Szakal, C., Winograd, N., Garrison, B.J., *J. Phys. Chem. A*, **2004**, *108*, 2993, with permission. and Wojciechowski, I.A., Kutliev, U., Sun, S., Szakal, C., Winograd, N., Garrison, B.J., *Appl. Surf. Sci.*, **2004**, *231-232*, 72, with permission.

5.1 Introduction

Ion emission from condensed phases under non-equilibrium conditions is important in a number of desorption techniques including SIMS,[1] matrix-assisted laser desorption/ionization (MALDI),[2] and electrospray ionization.[3] For the special matrix of water ice, the formation mechanism and structure of ionic water clusters is of interest to many researchers.[4] Ion emission from frozen samples bombarded by energetic ions is a commonly considered method for production of cluster ions of volatile liquids.[5]

Here we consider the ion emission process due to energetic particle bombardment as in SIMS experiments. Although some studies of ion emission were performed two decades ago on relatively simple systems,[6,7] no systematic efforts have been made to understand ionization in organic and biological systems. There are many stages in the bombardment event that can conceivably control the ultimate emission of ions. Namely,

ions can be pre-formed in the original sample,[8] energetic collisions or electronic processes can create ions, ions can then be neutralized as they depart the substrate and, of course, the ion stability is important. The influence of the matrix structure and the interactions among the ion and matrix molecules in the original sample on the emission dynamics is unknown. The challenges of tackling the ionization problem either experimentally or theoretically are daunting.

This study presents an initial step of the detailed experimental and theoretical investigation of ionization in molecular systems. We consider attachment of ions already present in the sample to parent molecules. This mechanism appears to be a universal way of forming secondary ions, almost independent of the molecule being investigated.[9] The parent molecules can associate with ions of both charges, positive ions such as, Na^+, K^+, or Cs^+, and negative ions such as F^-, Cl^-, or I^-. It has been proposed that an increase of ion concentration in the sample solution can promote the yields of charged components.[10] This connection, however, is not straightforward because the probability for an ion to emit and to be attached to the molecule(s) is determined by complex movement of ions in the collision cascade region and recombination of oppositely charged ions, thus reducing the number of emitted ions. We start our investigation of ionization with this study of the movement of simple ions in a molecular system to answer the question of how readily these ions eject and attach to the parent molecules. The influence of ion charge and concentration on the ion yield has not been systematically studied to the best of our knowledge.

As a realistic model system for experimental and theoretical studies, water ice is chosen for investigation. This material is an important matrix for SIMS experiments on

frozen-hydrated biological cells.[11] Ions of the type $(H_3O)^+(H_2O)_n$, $(H_2O)^+(H_2O)_n$ and $OH^-(H_2O)_n$ are observed,[11, 12, 13] although the intensity and cluster size distribution defy simple patterns. Pre-formed ions can be made by adding simple salts, in which case the mass spectra exhibit peaks corresponding to clusters such as $Na^+(H_2O)_n$. These ions probably form by a mechanism similar to the ions observed for organic and biological samples. Thus, we believe that the water ice system is a good model system for the investigations.

Group I salts in a water ice matrix are selected as targets to be bombarded by C_{60}^+ ions. Solutions of NaCl, NaBr, NaI, KI, and CsI were analyzed over four orders of magnitude in concentration. Specifically, we monitor $A^{\pm}(H_2O)_n$ secondary ion signals, where $A^{\pm}$ denotes positive or negative ions of the above salts. To complement the experimental results, a molecular dynamics (MD) method to study the mechanism of attachment of simple cations or anions to water molecules ejected from an ice matrix is provided. (*Note: MD simulations were performed by Dr. Igor Wojciechowski, who occupied a postdoctoral position with Dr. Barbara Garrison at the time these experiments were conducted.*) This approach has been shown to be effective in describing the motion of the atoms in energetic particle bombardment experiments.[14] Interaction potentials for water and ions with water, an essential input to the MD approach, are well established.[15]

For the molecular dynamics calculations, the same ionic water clusters of the form $A^{\pm}(H_2O)_n$, are studied, where $A^{\pm}$ represents Li^+, Na^+, Cs^+, F^-, Cl^-, and I^-, within an amorphous ice film deposited on a Au{111} surface, under bombardment by 300 eV Ar atoms. To cover the broad concentration range used in this study, the ice film containing

a single ion within 2-3 layers of the surface as well as a sample with eight Na^+ and Cl^- ions are explored in the calculations.

Qualitatively, much larger signals of positive ion-water clusters are observed than their negative counterparts – a finding supported by the theoretical data. Different solvation structures of cations and anions in water are shown to lead to larger absolute yield of cationic $A^+(H_2O)_n$ clusters as compared to anionic $A^-(H_2O)_n$ clusters. An effect of salt concentration in the original sample on the experimental ion yield is discussed in terms of ion pairing and clustering in concentrated solutions.

5.2 Experimental

Positive and negative SIMS spectra were acquired with the BioTof time-of-flight secondary ion mass spectrometer described in detail elsewhere.[16] The samples were prepared by taking 2 μL of each salt solution and spreading onto individual silver substrates. The sample and substrate were quickly immersed into liquid nitrogen while affixed to a copper sample block and subsequently transferred to a LN_2-cooled analysis stage. Samples of NaCl, NaBr, NaI, KI, and CsI were investigated at 0.0001M, 0.01M, and 1M concentrations. The samples were placed in the spectrometer at the same time and the data were taken on the same day. In principle, to compare quantitatively with the calculations, the experiments should be performed with the Ga^+ ion source with low incident energies. The Ga^+ source, however, causes considerable sample charging and reliable spectra cannot be obtained, despite the attempted use of an electron flood gun to solve this problem. The C_{60}^+ beam does not produce as much surface charging as atomic

projectiles because it seems to result in a more electrically balanced surface after C_{60}^+ bombardment in comparison to the atomic projectile bombardment. Thus, the C_{60}^+ ion source,[17] described in Chapter 2, was used at 20 keV kinetic energy. A total time of 10 to 20 s of primary beam etching at 0.6 nA dc current was needed to remove a water overlayer acquired from the sample transfer, and to expose a fresh surface for analysis. Charge compensation using low energy electrons was needed to detect signal for negative SIMS spectra. Although the nature of the collision cascades generated by low energy atomic beams and high energy C_{60}^+ beams are qualitatively different,[18] we present arguments below that the observed ion signals are strongly influenced by the ion-water interaction. Hence, it is the structure of the solid rather than the specifics of the dynamics of the collision cascade that lead to the observable cluster yields, and therefore, the 20 keV C_{60}^+ used in this experiment *can* compare with the 300 eV Ar projectiles used in the simulations.

5.3 MD Simulations

A detailed explanation of the MD simulations, performed by Dr. Igor Wojciechowski and Dr. Barbara Garrison, and presented here can be found elsewhere.[19] Briefly, the system investigated is a film of water ice adsorbed on a Au{111} substrate. The metal substrate is included in order to assist in confining the projectile energy in the surface region and reflecting this energy toward the vacuum.[20,21] All details of the H_2O-H_2O, H_2O-Au and Au-Au interaction potentials including the potential parameters have been described earlier.[22-24]

In the majority of calculations, the target included an amorphous ice film at 77K consisting of 1056 water molecules with one ion near the surface, representing infinite dilution, and comparing with the 0.0001M salt solutions employed in the experiment. A total of 8 Na^+ and 8 Cl^- ions were incorporated for the 1 M NaCl calculation. The water film was placed on the {111} surface of a 9-layer crystallite of 1980 Au atoms. For each ion, 450 trajectories were performed. Each trajectory lasted for more than 7 ps, sufficient time for the sputter yield to reach a constant value. All emitted clusters, however, were monitored over the next 250 ps to allow the clusters to undergo unimolecular decomposition.

5.4 Results and Discussion

Three general trends are manifested in the experimental data: 1) For the same salt solutions in water ice, cations and their corresponding water clusters of the form $A^+(H_2O)_n$ are emitted more favorably than the associated anions and corresponding water clusters of the form $A^-(H_2O)_n$. This is evidenced by A) higher secondary ion signals for a particular water cluster + ion within the series and B) the series extending further in water cluster number for cations than anions; 2) The secondary ion signals for a specific salt in water ice do not increase linearly with concentration; 3) Signals of $A^{\pm}(H_2O)_n$ for a given species "A" are not similar if the corresponding counterion changes.

This work will provide insights into the above phenomena that impact SIMS sputtering processes with simulations helping to explain the experimental data. Ion pairing and clustering in the original mixture and during atomic bombardment is

proposed to be responsible for a much slower than linear increase in ion yield as a function of salt concentration as well as for the effective emission of bare ions from concentrated solutions as observed in the experimental data.

5.4.1 Cation vs. Anion Effect

For the simplest experimental example, we present an "infinitely dilute" salt solution in a water ice matrix. NaI at 0.0001M concentration within water ice was prepared as indicated in section **5.2**. An example of more favorable cation emission compared to anions is illustrated in Figure **5-1**. Here, we analyze the amount of bare Na^+ and I^- ions emitted as well as corresponding ion-water clusters of the form $A^{\pm}(H_2O)_n$. Some intriguing observations of this data can be made including A) much higher secondary ion signals of $A^+(H_2O)_n$ are emitted and/or detected compared to $A^-(H_2O)_n$, B) the cationic water clusters extend to further "n" than the anionic water clusters, and C) almost no bare Na^+ is emitted from this infinitely dilute NaI in water ice system.

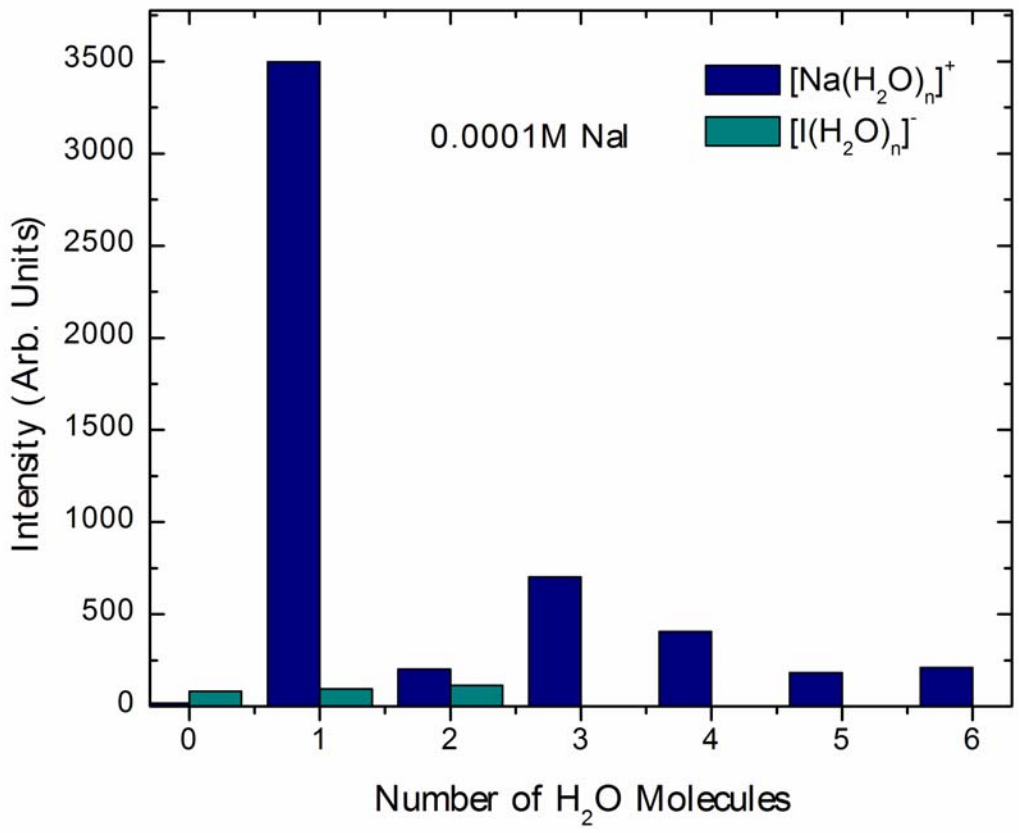

Figure **5-1**: Comparisons of secondary cations and corresponding ion-water clusters relative to anions and their corresponding ion-water clusters for 0.0001M NaI in water ice.

It is helpful to now shift attention to the MD simulations to try and explain these observed phenomena. The total sputter yields and numbers of ionic clusters emitted from infinite dilution samples by 300 eV Ar projectiles are given in Table **5-1**. The main observation is that cationic water clusters are emitted more effectively than the anionic water clusters, just as in the experimental results.

Table **5-1**: Sputtering yields and numbers of ionic water clusters ejected in 450 trajectories of 300 eV Ar atoms bombarding the water ice film with one ion (data includes bare ions as well as water-solvated ions).[19]

Ions	Total Sputtering Yield	Total Number of Sputtered Ions
Li^+	0.22	97
Na^+	0.21	95
Cs^+	0.18	83
F^-	0.04	18
I^-	0.04	16
Cl^-	0.02	8

The more effective emission of cation water clusters as compared to anion clusters can be explained by the different solvation structure of positive and negative ions in water. Both MD and *ab initio* calculations of the ion solvation structure in bulk water and at the liquid-vapor interface indicate that cations interact strongly with neighboring water molecules via cation-oxygen attraction, while the interaction of an anion with nearest water molecules is weaker.[25,26] The cation-oxygen interaction results in re-orientation of water dipoles in the vicinity of the ion, thus disrupting the hydrogen bond network. Consequently, the local structure can be characterized as an almost pre-formed solvated ion with weak bonding to the remaining liquid. The preferred orientation of water molecules around a central anion, however, is similar to the orientation around a central water molecule, i.e., the anion in water does not introduce a large perturbation and the hydrogen bond network retains its structural identity near the anion.[26] The net effect is that even though the interaction of the anion with water is locally weaker than the cation with water, the interaction of the anion and its solvation structure with the whole medium is stronger than that for cations.

This feature of the ion-water interactions is illustrated in Figure **5-2**, where the interaction of the sphere of a given radius, including the sodium or chloride ion in the center of the surrounding water molecules, is calculated as a function of the radius. The ion position is 2-3 Å below the water surface. The symbols for the smallest radii correspond to the interaction of the bare ion with water. The next radius corresponds to the first solvation shell of water molecules around the Na^+ or Cl^- ion. The interaction energy of the Na^+-water complexes with the remaining system is weaker than that for the Cl^--water complexes, while the bare Na^+ is more strongly bonded to the solution than the Cl^- ion.

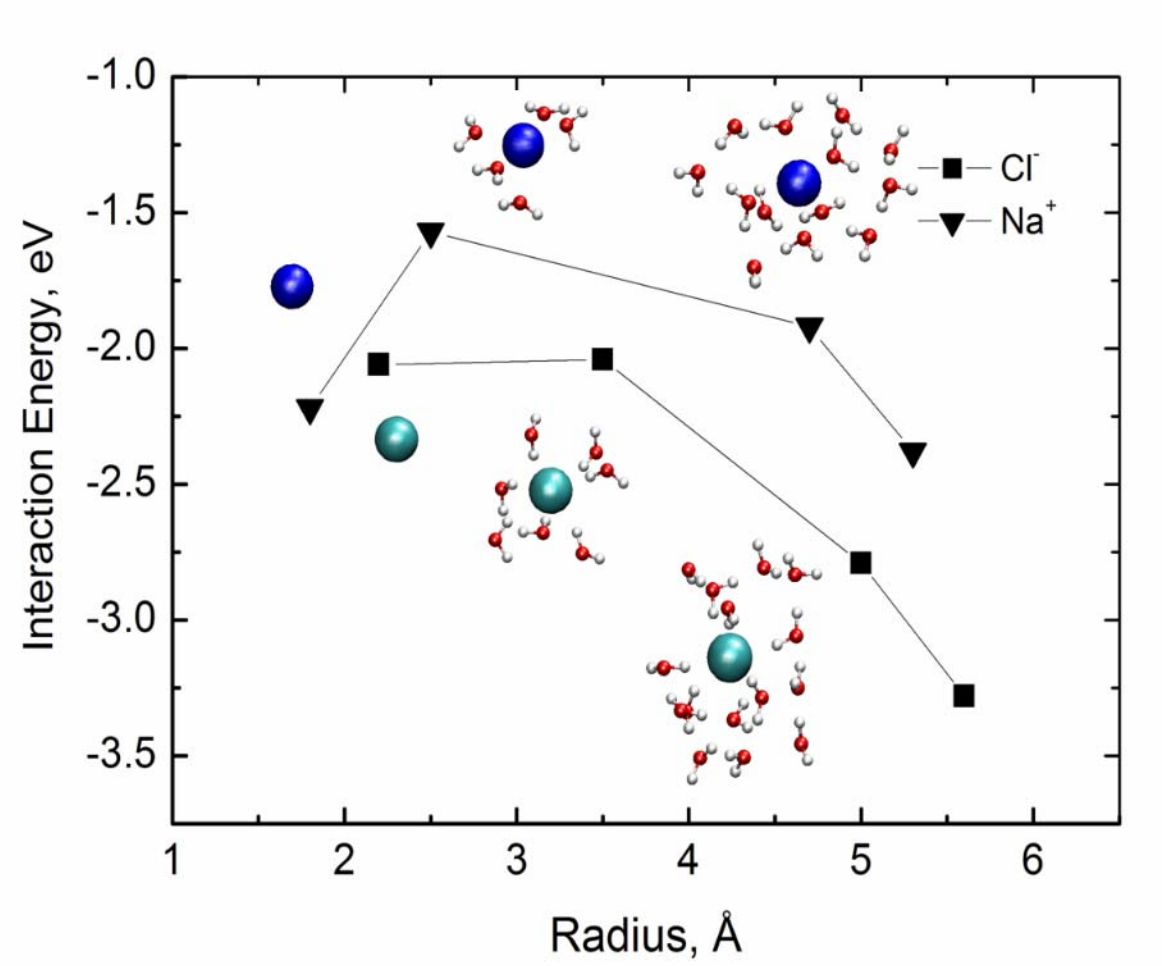

Figure **5-2**: The interaction energies of the sphere, with the ion in the center of the surrounding waters forming a solvation shell, as a function of the sphere radius.

Desorption of a cation along with its first solvation shell requires, therefore, less energy than desorption of an anion with its solvation shell. The detailed analysis of sputtering trajectories shows that the water molecules initially adjacent to the cations mainly accompany them in the ejection event. Therefore, the contribution of bare cations to the ion yield at low concentrations should also be smaller when compared to that of cluster ions.

5.4.2 Concentration Effect

It is well-known that SIMS is not a natively quantitative analysis technique and that SIMS matrix effects can seriously alter the operable linear dynamic range (LDR) for analyte concentration within a given sample. However, it is not intuitive that within a system containing only salt and frozen water, that the secondary ion signals do not follow linearly with salt concentration. Figure **5-3** and Figure **5-4** are representative of the concentration effect observed for these sample systems. Na^+, K^+, and I^- secondary ions and their corresponding ion-water clusters are analyzed at 1M, 0.01M, and 0.0001M concentrations. Interesting observations include A) all secondary ion data between < 1 and < 2 orders of magnitude despite the salt concentrations spanning four orders of magnitude, and B) the 1M and 0.01M concentrations exhibit exponential decays of the secondary ion signals with respect to "n" ion-water clusters, while the infinitely dilute 0.0001M samples exhibit non-trending flat profiles for the same variables. This seems to suggest that a relatively large number of bare ions are emitted for the highest concentrations, in comparison to the more dilute solutions – a notion supported by the simulations in the previous section.

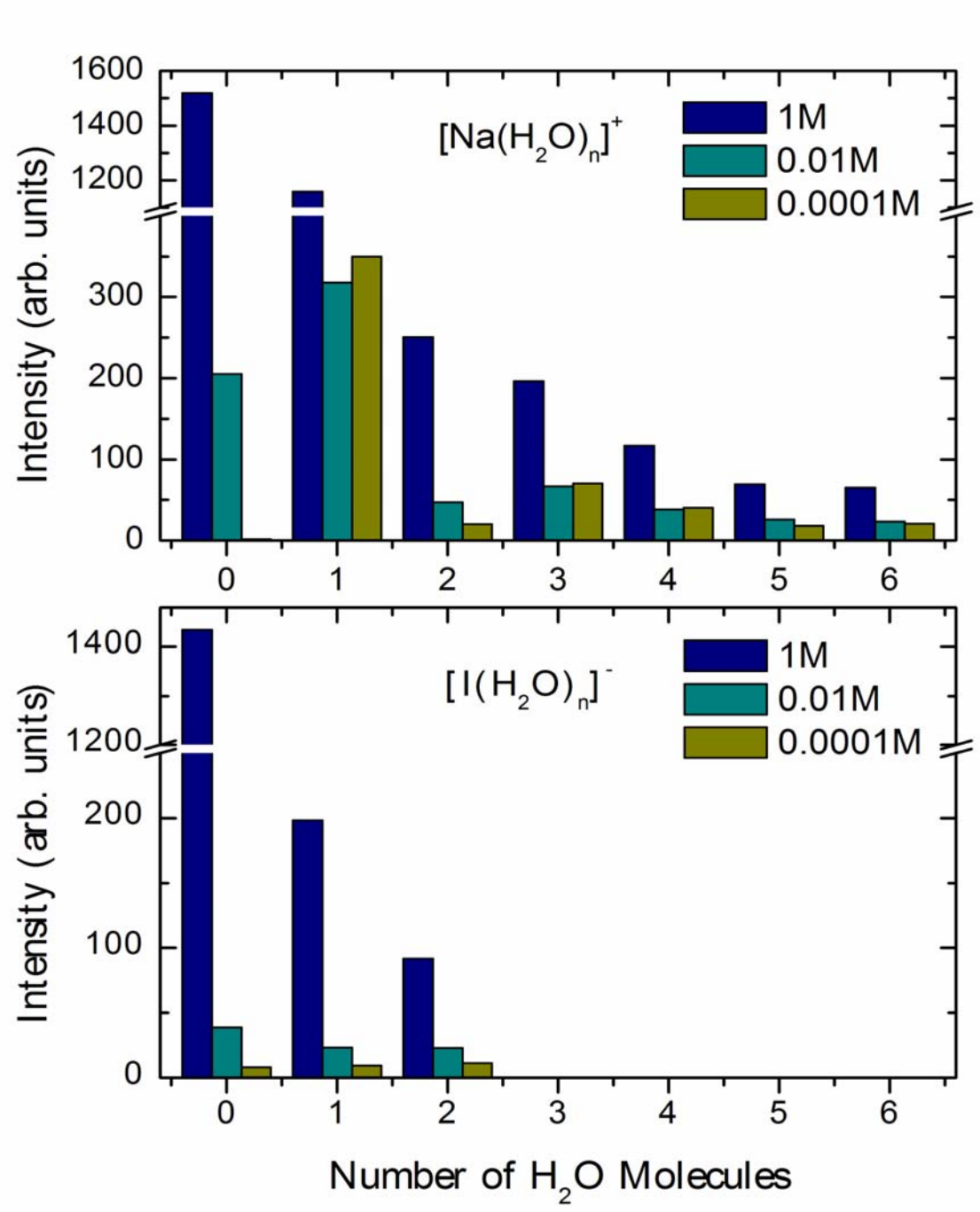

Figure **5-3**: Comparisons of secondary cations, anions, and corresponding ion-water clusters for 1M, 0.01M, and 0.0001M NaI in water ice.

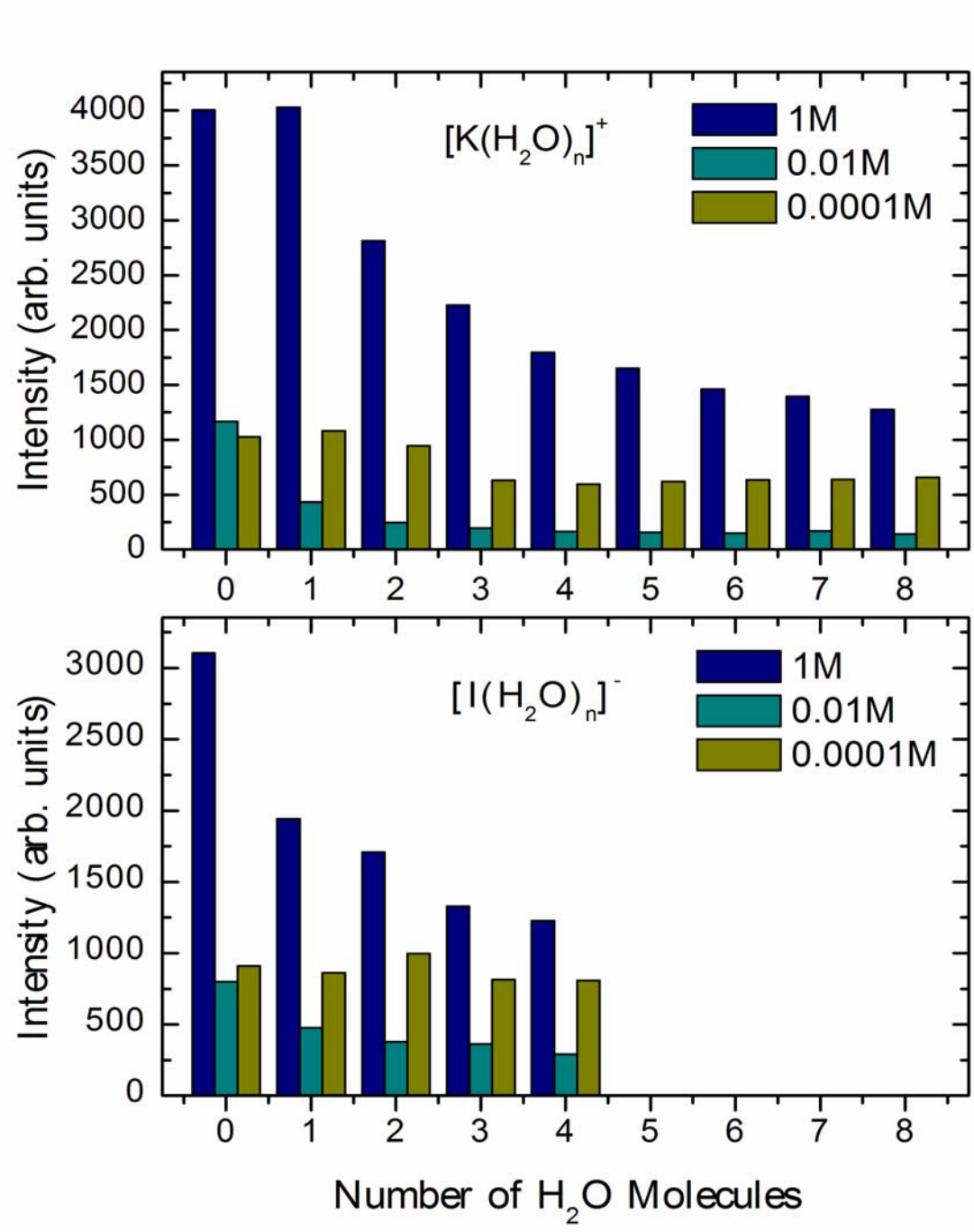

Figure **5-4**: Comparisons of secondary cations, anions, and corresponding ion-water clusters for 1M, 0.01M, and 0.0001M KI in water ice.

The observation of a relatively large number of bare ions for the 1 M solutions relative to the lower concentration solutions is consistent among the various systems studied experimentally. The presence of clusters of ions without full solvation shells for each ion in the initial solution could result in more bare ions being ejected or at least shifting the distribution towards smaller clusters. In order to investigate the concentration effect, MD simulations are presented for a model system consisting of eight Na^+ and eight Cl^- ions in the water sample, a concentration that is approximately 1 M. The yields of species ejected are given in Table **5-2**. The most abundant cluster is the one with one cation and one anion, that is, a neutral species that would not be detected. In total there are 52 charged clusters of which 11 (21%) are bare ions. For the isolated ion calculations, the bare ions only contribute 1-3% to the total yield. Thus, the calculations confirm the experimental finding that there are a relatively large number of bare ions. The mechanistic reasons for the large number of bare ions as well as for the deficiency in ion yields for the higher concentrations relates to there being: like-ion pairs stabilized within the ice film that then repel to form bare ions upon emission, and counterion pairs that emit as neutral species and don't get detected, respectively.

Table **5-2**: Numbers of ion-containing clusters for 300 trajectories of 300 eV Ar atoms bombarding the 1M solution of NaCl. Numbers in the left column, *n, m, x,* indicate the amounts of Na^+ (n), Cl^- (m) and H_2O (x) species in the emitted clusters.[19]

$Na_n^+Cl_m^-(H_2O)_x$	Total Number of Ejected Clusters	Cluster Charge
1,0,0	8	+1
0,1,0	3	-1
1,0,>0	21	+1
0,1,>0	4	-1
1,1,≥0	35	0
1,2,≥0	3	-1
2,1,≥0	10	+1
2,2,≥0	6	0
3,2,≥0	2	+1
2,4,≥0	1	2

For 1 M NaCl solutions at room temperature, simulations show quite clearly that there is considerable clustering of ions in the water.[27-31] One prediction at room temperature is that 16% of the total ions are clustered as neutral NaCl dimers, 19% as singly charged trimers, 2% as neutral tetramers and the remaining 63% of the ions are in similar environments as the dilute solution.[28] According to other data,[29] the concentration of the complexes with two or more ions of the same charge in close vicinity of one another can reach 0.2 M for the 1 M solution. These ion clusters can and do have intervening water molecules but are recognizable as localized entities. As the density of the liquid decreases, a situation that occurs during the particle emission in the bombardment event, the amount of clustering of ions increases because there is less water to stabilize individual solute ions. In opposite charge complexes, the ions form neutral species that cannot be detected. In the like charge complexes, the ions repel each other in the lower density conditions and eject as bare ions.

The above discussion explains the presence of the bare ions at high concentration in terms of the initial film structure and a minimal collision cascade caused by 300 eV Ar bombardment. The C_{60}^+ bombardment event leads to numerous overlapping collision cascades that create a highly disordered region in a short time leading to a dense liquid-like region.[18] These motions should further enhance pairing of opposite-charged species and repulsion of like-charged species. Thus, at high concentrations, the number of ions that reach the detector is not proportional to the initial concentration in the film.

5.4.3 Counterion Effect

We take the situation where the previously mentioned sample systems giving highest secondary ion signals are for emitted cations at 1M concentration. A logical extension when determining sputter properties of solvated salts is how these systems behave for a constant cation with different anions. Figure **5-5** shows the secondary ion response of bare Na^+ ions and their corresponding ion-water clusters for 1M NaCl, NaBr, and NaI. The expectation based on the cation vs. anion effect and the concentration effect is that the signals of the form $A^+(H_2O)_n$ would be relatively similar, regardless of counterion. However, as is observed in the figure, greater than one order of magnitude intensity range is expressed for the three salts studied where NaI signals > NaBr > NaCl. Despite the exponential signal response being observed as before, this plot is certainly puzzling.

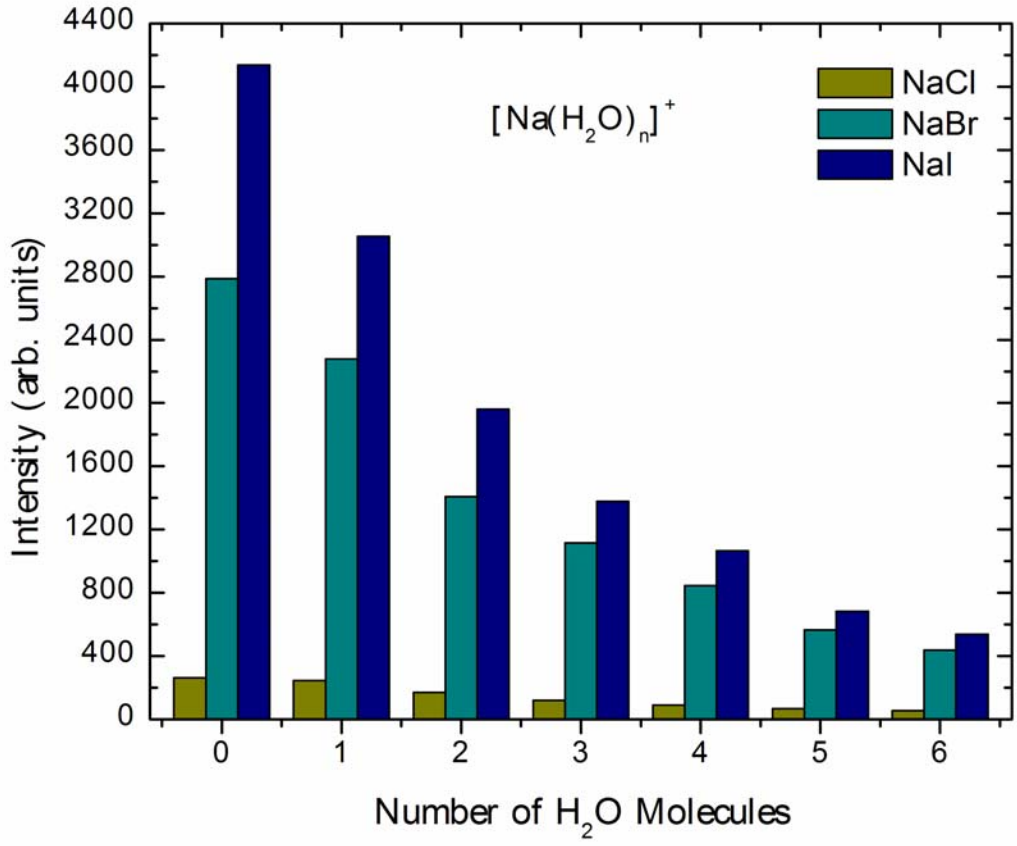

Figure 5-5: Comparisons of secondary cations and corresponding ion-water clusters for 1M solutions of NaCl, NaBr, and NaI in water ice.

If we examine the effect of anion size on the hydrogen bond network in water ice, the larger anions would certainly disrupt the natural order more. One potential impact of this is that more water molecules are needed to surround a given anion, leaving a higher chance of Na^+ ions producing pairs, which as stated earlier, would repel strongly upon being emitted, and lead to higher bare sodium secondary ion signal. The same result can be reasoned if we look at the thermodynamics for the heat of solvation. For gaseous salts being solvated by water, it is more energetically favorable to solvate a smaller sodium

salt like NaCl than NaBr or NaI. If solvation increases, the number of neutral pairs decreases, leaving more like ions together and higher sodium signals.

Figure **5-6** shows the opposite approach where the anion is kept constant and the cations varied. Besides the signals being lower than the cationic counterparts as observed earlier, nothing here seems to present a trend. The secondary signals are highest for KI, then NaI, and finally CsI – the latter having only bare I^- ions emitted with no cluster forms. It appears that cation size is not playing a role in the signal trends as can be the case for the anions studied. Similarly, no trend exists within the thermodynamic data for explanation.

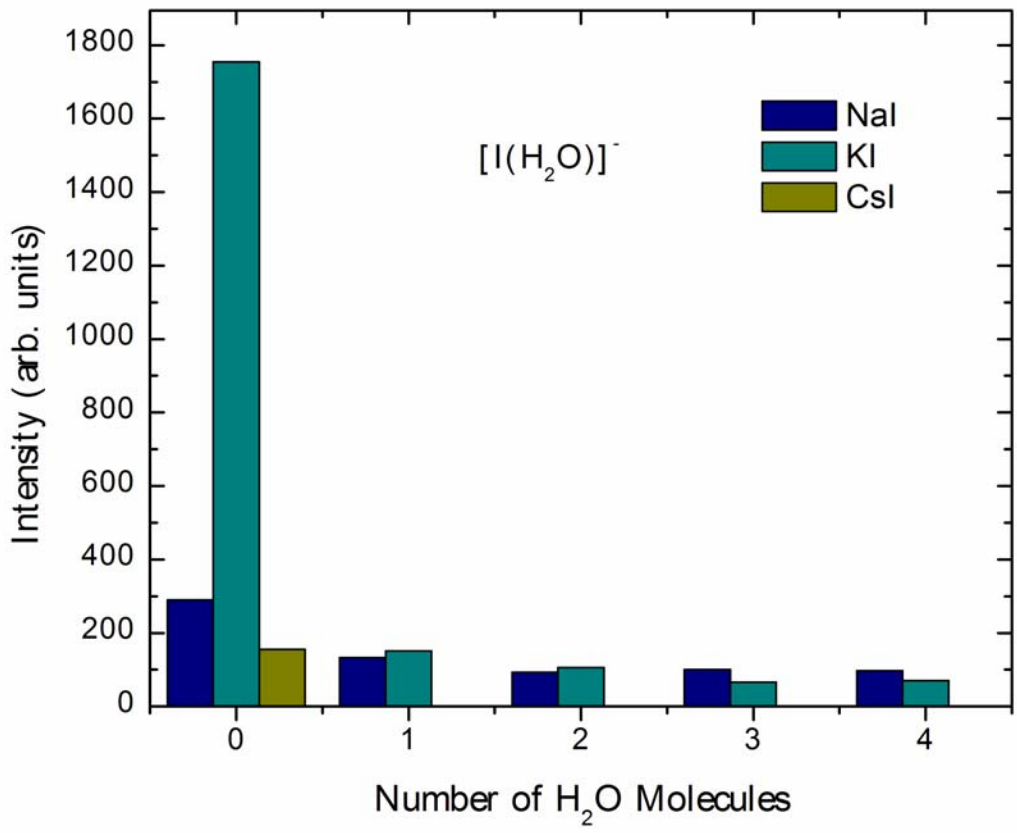

Figure **5-6**: Comparisons of secondary anions and corresponding ion-water clusters for 1M solutions of NaI, KI, and CsI in water ice.

5.5 Conclusions

This combined experimental and calculation study of the ejection of pre-formed ions in keV particle bombardment elucidates several important features of the emission process. First, we observe significantly more cations than anions in the spectra for the low initial concentrations of ions. From a microscopic viewpoint, the anions do not disrupt the hydrogen bond network in the water, thus the anions are trapped inside the

matrix and do not readily eject. The cations, on the other hand, establish a preformed complex that breaks down the hydrogen-bonded network, thus allowing the cluster to eject more easily. The concept that ions (or other species) can destabilize the original matrix and thus alter the ejection properties in SIMS experiments is new and has potential general applicability to other matrices besides water ice.

The experiments show that signals are not linear with concentration, as evidenced by NaI and KI secondary in signals varying by less than two orders of magnitude for concentration ranges spanning four orders of magnitude. This concentration effect in SIMS can be qualitatively explained using MD calculations for a 1M solution of NaCl. Ion recombination, stemming from the collision cascade, limits the ion yield. Complexes of like ions, such as Na^+-Na^+, which can exist in water, become unstable during the emission. As a result, bare ions can more readily be emitted from these environments. In the experiments, this helps to explain the exponential signal response with respect to ion-water cluster number. Additionally, we observe that the initial distribution of ions in the solution influences the yield at high concentrations. The original solution has regions of ions of opposite charge in close proximity. These ions tend to neutralize each other, thus the yield of detected ions is not proportional to the initial concentration. There are also configurations of nearby ions of the same charge. These configurations are destabilized during the bombardment event and bare ions tend to be ejected. Certainly, there can be association of ions of opposite charges during the sputtering event, especially with the C_{60} bombardment at 20 keV. It is also conceivable that the bombardment event causes ions of like charges to interact and repel each other. Although these dynamic events can be important, the pairing of ions of opposite and like charges in the initial film can

explain the major features of the concentration effect. Neutralization of charges of opposite sign should be ubiquitous in all SIMS experiments with pre-formed ions.

The counterion effect, however, represents a phenomenon that cannot be clearly explained. For 1M solutions of the same cation and different anions, there is a clear trend that higher cation and cation-water clusters are emitted from the salts with the largest anions. Potential explanations with regard to anion size and the thermodynamics related to salt solvation are presented, but have not been studied enough in the simulations to gain insight into the chemistry taking place in these frozen solutions. For 1M solutions of the same anion and different cations, no clear trend is evident at this time. Additional experiments, possibly with different anion and cation sets, need to be performed before a reasonable explanation can be deduced from this particular data.

5.6 References

1. See, for example, *ToF-SIMS: Surface Analysis by Mass Spectrometry*; Vickerman, J. C., Briggs, D., Eds.; IM Publications and Surface Spectra Limited: Manchester and Chichester, **2001**.

2. See, for example, Hillenkamp, F, Karas, M., Beavis, R. C., Chait, B. T., *Anal. Chem.*, **1991**, *63*, 1193A.

3. See, for example, Whitehouse, C. A., Dreyer, R. N., Yamashita, M., Fenn, J. B., *Anal. Chem.*, **1985**, *57*, 675.

4. Zhou, J., Lu, X., Wang, Y., Shi, J., *Fluid Phase Equilibria*, **2002**, *194-197,* 257.

5. Boryak, O. A., Stepanov, I. O., Kosevich, M. V., Shelkovsky, V. S., Orlov, V. V., Blagoy, Yu. P., *Eur. Mass Spectrom.*, **1996**, *2,* 329.

6. Williams, P., *Surf. Sci.*, **1979,** *90*, 588.

7. Yu, M. L., Lang, N. D., *Nucl. Instrum. Methods Phys. Res. B*, **1986**, *14*, 403.

8. Pachuta, S. J., Cooks, R. G., *Chem. Rev.*, **1987**, *87*, 647.

9. Hagenhoff, B., In *ToF-SIMS: Surface Analysis by Mass Spectrometry*; Vickerman, J. C., Briggs, D., Eds.; IM Publications and Surface Spectra Limited: Manchester and Chichester, **2001**; pp. 285.

10. Gusev, A. I., Choi, B.K., Hercules, D.M., *J. Mass. Spectrom.*, **1998**, *33*, 480.

11. Roddy, T. P., Cannon, D. M. Jr., Meserole, C. A., Winograd, N., Ewing, A. G., *Anal. Chem.*, **2002**, *74*, 4011.

12. Lancaster, G. M., Honda, F., Fukuda, Y., Rabalais, J. W., *J. Am. Chem. Soc.*, **1979**, *101,* 1951.

13. Donsig, H. A., Vickerman, J. C., *J. Chem. Soc. Faraday*, **1998,** *93,* 2755.

14. Garrison, B. J., In *ToF-SIMS: Surface Analysis by Mass Spectrometry*; Vickerman, J. C., Briggs, D., Eds.; IM Publications and Surface Spectra Limited: Manchester and Chichester, **2001**; p. 223.

15. Koneshan, S., Rasaiah, J. C., Dang, L. X., *J. Chem. Phys.*, **2001**, *114,* 7544.

16. Braun, R. M., Blenkinsopp, P., Mullock, S. J., Corlett, C., Willey, K. F., Vickerman, J. C., Winograd, N., *Rapid Commun. Mass Spectrom.*, **1998**, *12,* 1246.

17. Weibel, D., Wong, S., Lockyer, N., Blenkinsopp, P., Hill, R., Vickerman, J.C., *Anal. Chem.*, **2003**, *75*, 1754.

18. Postawa, Z., Czerwinski, B., Szewczyk, M., Smiley, E.J., Winograd, N., Garrison, B.J., *Anal. Chem.*, **2003**, *75*, 4402.

19. Wojciechowski, I.A., Sun, S., Szakal, C., Winograd, N., Garrison, B.J., *J. Phys. Chem. A*, **2004**, *108*, 2993.

20. Delcorte, A., Vanden Eynde, X., Bertrand, P., Vickerman, J.C., Garrison, B.J., *J. Phys. Chem. B*, **2000**, *104*, 2673.

21. Delcorte, A., Garrison, B.J., *J. Phys. Chem. B*, **2000**, *104*, 6785.

22. Dou, Y., Zhigilei, L.V., Winograd, N., Garrison, B.J., *J. Phys. Chem. A*, **2001**, *105*, 2748.

23. Berendsen, H.J.C., Postma, J.P.M., van Gunsteren, V.F., Hermans, J., In *Intermolecular Forces*; Pullman B., Ed., Reidel: Dordrecht, **1981**.

24. Spohr, E., *J. Mol. Liq.*, **1995**, *64*, 91.

25. Dang, L.X., *J. Phys. Chem. B*, **2002**, *106*, 10388.

26. Ayala, R., Martinez, J.M., Pappalardo, R.R., Marcos, E.S., *J. Phys. Chem. A*, **2000**, *104*, 2799.

27. Oelkers, E.H., Helgeson, H.C., *Science*, **1993**, *261*, 888.

28. Driesner, T., Seward, T.M., Tironi, I.G., *Geochimica et Cosmochimica Acta*, **1998**, *62*, 3095.

29. Degève, L., da Silva, F.L.B., *J. Mol. Liq.*, **2000**, *87*, 217.

30. Sherman, D.M., Collings, M.D., *Geochem. Trans.*, **2002**, *3*, 102.

31. Chialvo, A.A., Cummings, P.T., Simonson, J.M., Mesmer, R.E., *J. Mol. Liq.*, **1997**, *73-74*, 361.

Chapter 6

Using Water Ice to Examine Cluster Ion Surface Sensitivity

This chapter is adapted from: Szakal, C., Kozole, J., Winograd, N., *Appl. Surf. Sci.*, **2006**, *252*, 6526, with permission. Copyright is retained by Elsevier, B.V.; and Szakal, C., Kozole, J., Russo Jr., M.F., Garrison, B.J., Winograd, N., *Phys. Rev. Lett.*, **2006**, *96*, 216104, with permission. Copyright is retained by the American Physical Society.

6.1 Introduction

The landscape of the field of SIMS has changed dramatically with the introduction of cluster ion projectiles to initiate sputtering and depth profiling.[1-3] Polyatomic primary projectiles such as C_{60}^+, SF_5^+, Au_n^+, and Bi_n^+ have become commonplace for a variety of SIMS analyses. Since each atom in the cluster contains a proportionately smaller kinetic energy than those in an atomic projectile, the incident energy is deposited in a concentrated region near the sample surface. This effect has lead to a number of new observations including the formation of mesoscale craters of several nm in diameter,[4] reduced physical damage in the vicinity of the crater walls,[5] and the observation that molecular ions of thermally labile biomolecules can be desorbed intact with orders of magnitude greater efficiency than with atomic projectiles.[6,7] Clusters such as C_{60} yield particularly intriguing physical phenomena during collisions with surfaces

and have opened the door to smoothing of surfaces,[8] thin film synthesis,[9,10] SIMS molecular depth profiling,[11-15] and most recently, SIMS bioimaging.[16-19]

For atomic bombardment, many of the details of the energy deposition process are understood, with molecular dynamics computer simulations and collision cascade theory providing the insight. The new physical properties associated with cluster bombardment still present a number of challenges which are important to resolve in order to maximize the value of the emerging applications noted above. An interesting dichotomy lies in the relationship between the degree of surface damage and interlayer mixing and the range of deposited energy. For example, a 15 keV Ga projectile penetrates about 7 nm into a Ag substrate before coming to rest, whereas a C_{60} molecule with the same energy stops within about 2 nm of the Ag surface.[5] Yet, for Ag, about 80% of the sputtered atoms originate from the top one layer of Ag when bombarded by an atomic projectile such as Ga^+ or Au^+, but for bombardment by C_{60} with the shallower energy deposition range, about 80% of the particles originate from the top three-layers.[5] Even though the particle flux removed by an atomic projectile appears to be more sensitive to the surface composition, the depth resolution achieved during depth profiling experiments is dramatically improved when using cluster projectiles at comparable total kinetic energy.[11,13]

Here, we report on a method of studying the sputtering properties of water ice, including the yields of sputtered water molecule equivalents for different primary projectiles, and the escape depths of silver ions from an underlying sample layer. A similar approach was first used to study the yields of water ice by atomic ion bombardment,[20] but in comparison, the current methodology improves the accuracy of

the reported water ice film thickness measurement by two orders of magnitude. The ice system is chosen as a model since it has a low cohesive energy comparable to many molecular solids of practical interest and it is the matrix within and surrounding targeted biological cells in bioimaging experiments.

To elucidate the basis for the aforementioned contradictory behavior, we examine experimentally the response of a Ag substrate covered with water ice overlayers of 5 to 225 Å that is bombarded by 25 keV Au^+, Au_2^+, Au_3^+ and 20 keV C_{60}^+. Additionally, we show sputter yields of water ice for these projectiles at various energies to range from 100 to 10,000 water molecule equivalents. A discussion is provided that relates these data to an enhanced SIMS surface sensitivity for cluster projectiles, and in particular, C_{60}^+, when compared to traditionally employed atomic projectiles. Molecular dynamics computer simulations are included to aide in the interpretation of the information.

6.2 Experimental

6.2.1 Sample Preparation

Ice samples are prepared on an Ag-coated, modified QCM (quartz crystal microbalance) assembly from Maxtek, Inc., as illustrated in Figure **6-1**. Briefly, a polished standard 6 MHz AT-cut quartz crystal of 13 mm diameter is coated in gold, and 50 nm of Cr and 500 nm of Ag are vapor-deposited, respectively. The Cr acts as a buffer layer between the Ag and Au to prevent alloy formation. The crystal is mounted in such a way as to expose only the mass-sensitive area of the top crystal (the center 6.6 mm

diameter, or the size of the bottom electrode superimposed upwards) to the vacuum chamber. Before ice deposition, the sample device is cooled to about 100 K by liquid nitrogen and allowed to equilibrate since temperature fluctuations cause drifts in QCM measurements. In this experiment, we take advantage of the intrinsic property of the AT-cut quartz having a frequency change sensitivity that is independent of the temperature of the analysis, once a constant temperature is achieved. Astrophysics experiments where water ice was deposited onto a QCM apparatus revealed that between 80 and 130 K, the water ice forms in an amorphous manner, whereas above 130 K, the ice is crystalline, and below 80 K, different forms of ice begin to form.[21]

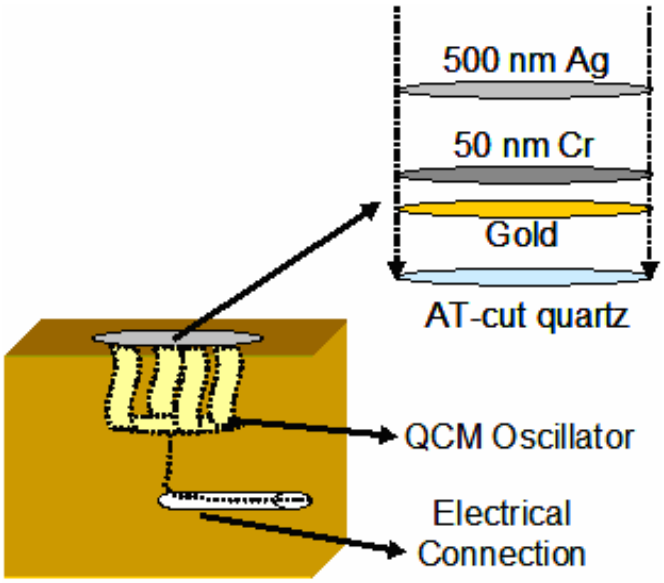

Figure **6-1**: Schematic diagram of a modified QCM assembly. The oscillator is embedded into a copper holder with proper insulation for the electrical connection. Only the mass-sensitive area of the crystal is exposed at the top of the holder.

Water vapor is bled into the analysis chamber with a base pressure of 1 x 10^{-9} torr at any desired time using a Varian variable leak valve. The vapor is formed on the other side of the leak valve by first placing liquid water into a reservoir and cooling to liquid

nitrogen temperature, pumping on the system, and finally letting the system thaw after vacuum isolation. When the valve is opened again, vapor enters a side chamber for first-stage control of pressure, and when a stable leak rate is established, the valve between the side chamber and analysis chamber is opened to achieve localized pressures of 2×10^{-6} torr and 2×10^{-7} torr, respectively. A residual gas analyzer, (RGA, model 100C from UTI, Sunnyvale, CA) is used to monitor the components of the vacuum before, during, and after ice deposition.

A Maxtek TM-400 thickness monitor is used to measure the amount of ice deposited onto the silver-coated QCM crystal before, during, and after the planned deposition period. The measured frequency change is related to the mass of deposited material. From the known density of amorphous ice of 0.92 g/cm^3, and knowledge about the active area of the quartz crystal, it is possible to directly measure the change in film thickness as a function of time. Details of this procedure are reported in section **4.2.2**. Before the deposition, no change in frequency is observed, and therefore, there is no change in the mass of species on the crystal surface. During the deposition, a rate of approximately 0.15 Å/sec is measured – a value that is consistent for the pressures indicated above over the multiple iterations of water ice deposition and for values deposited ranging from 5 Å to 150 nm. After the deposition interval, the rate immediately changes to zero again. This series of observations, along with the RGA data listed above, proves that only water is being deposited and/or measured during the deposition events, meaning that all mass change on the crystal that induces a change in frequency can be attributed to water ice.

6.2.2 Sample Analysis

The BioTof time-of-flight secondary ion mass spectrometer[22] is used to monitor the water and ^{107}Ag ion signals with respect to primary ion sputter time. For this study, C_{60} ions are used from 10 keV to 120 keV, and Au_n^+ projectiles are employed at energies from 10 keV to 25 keV. For energies less than 20 keV, C_{60}^+ ions are formed in the 20 keV buckminsterfullerene source described in chapter 2. For 20 keV to 120 keV C_{60} ions, a new buckminsterfullerene source is used that is similar in design to that in chapter 2, except that it is equipped with a Wien filter for mass selection of the C_{60} ions.

6.2.3 MD Simulations

Note: Michael Russo, Jr. is responsible for the computer simulations presented in this chapter. His work helps to complete the understanding of the experimental data.
The molecular dynamics (MD) scheme utilized here is described elsewhere.[23] Simulations are performed using Au, Au_2, Au_3, and C_{60} projectiles to bombard a substrate of 25 Å of amorphous water ice on a Ag microcrystallite that measures 278 x 278 x 100 Å. The sample requires 432,048 Ag atoms and 62,780 water molecules to contain all of the relevant motion. The forces among the atoms within the substrate are described by a mix of several different empirical potential functions with water molecules constrained to be rigid through the use of the RATTLE algorithm. The descriptions of these potentials along with their parameters are described elsewhere.[24] By fitting to electronic structure calculations,[25] parameters for the Ag-O Morse interaction are determined to be $D_e = 0.0868$ eV, $r_e = 2.28$ Å and $\alpha = 1.3$ Å^{-1}. The Ag-H interaction is purely repulsive

with V(r) = 2000 eV*exp(-17 $Å^{-1}$*r). For the incident clusters, all interactions with substrate constituents are modeled using a Molière potential. For the Ag-Ag and Au-Au interactions, an Embedded Atom Method many-body potential is employed,[26] and for C-C the REBO potential is used.[27]

Integration of the equations of motion for very energetic collisions of a projectile with a rigid water molecule is numerically challenging. Consequently, an initial kinetic energy of 15 keV is chosen for the simulations, which represents a balance of maintaining an energy close to the experimental value and one that is numerically tractable. The particles are directed at an angle of 40° with respect to the surface normal and are randomly oriented. Two different trajectories are performed for the cluster projectiles Au_3 and C_{60}, each extending to 20 ps. Ten different trajectories are required for Au and Au_2 since the course of the trajectory depends upon the coordinates of the projectile/surface collision. For these studies, there is only a weak dependence of the dynamics of the water overlayer subsequent to impact. The nature of the Au-Ag dynamics depends more strongly upon the impact point.

6.3 Results and Discussion

The integrated peak intensity of the $^{107}Ag^+$ secondary ions are recorded after each incremental water ice deposition of 5 or 10 Å, utilizing a primary ion fluence of approximately $10^8/cm^2$ in each spectrum to avoid observable beam-induced damage. Log/linear plots of the $^{107}Ag^+$ secondary ion integrated peak intensity vs. deposited film thickness for each primary projectile are summarized in Figure **6-2**. These data show that

regardless of projectile type, there is a region where the $^{107}Ag^{+}$ ion yield decreases exponentially with increasing ice film thickness. This dependence suggests that the overlaying water film attenuates the $^{107}Ag^{+}$ ion intensity according to a simple relation $\exp(-z/\lambda)$, where z is the ice film thickness, and λ is a decay length parameter reported in Table **6-1** and is dependent upon the nature of the incident projectile and the overlayer material.

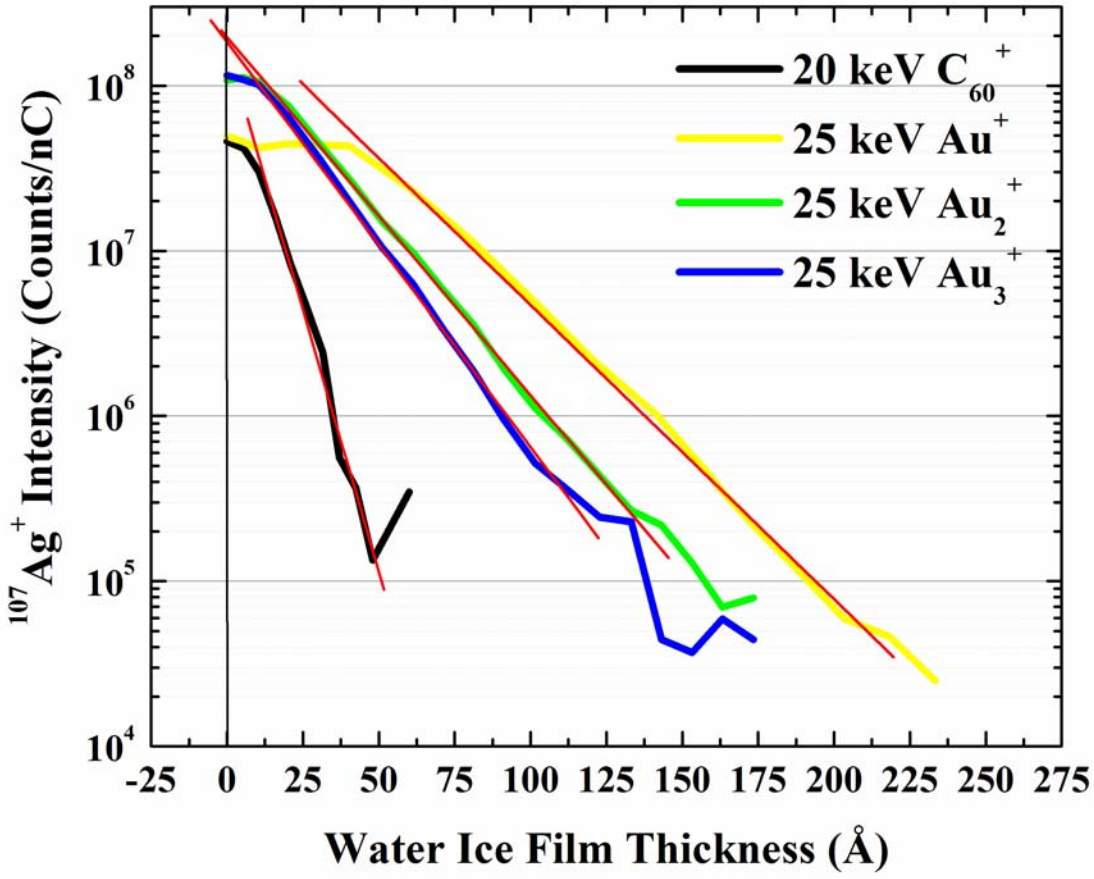

Figure **6-2**: Integrated peak intensity values for $^{107}Ag^{+}$ vs. water ice film thickness for the four primary projectiles being studied. Linear regression lines are included to show the data used for determining the λ values.

Table **6-1**: Characteristic depths of projectile energy loss, λ, in the water ice film as measured by the $^{107}Ag^{+}$ intensity. Y_{eq} represents the number of removed water molecule equivalents for each projectile at a specified incident energy. The energy loss in the water ice overlayer is determined from the MD simulations. Standard deviations are included for the Au and Au_2 projectiles since the energy loss is dependent upon the incident trajectory.

	Au	Au_2	Au_3	C_{60}
λ (Å)	24	20	18	7.0
Y_{eq}				
10 keV			630	820
15 keV			910	1350
20 keV				1830
25 keV	94	570	1200	
40 keV ($^{+}$)				4040
40 keV ($^{++}$)				3610
80 keV				8070
120 keV				10,100
Energy Loss (keV)	4.7 ± 1.8	4.8 ± 1.8	7.3	14.5

These results are striking since the data show it is possible for Ag^{+} ions to eject from the surface initially covered with a water ice overlayer of up to 225 Å. Moreover, the amount of Ag signal attenuation is considerably greater for C_{60} than for any of the other projectiles, suggesting it is most sensitive to the presence of water overlayers. The MD simulations provide a definitive explanation. Shown in Figure **6-3** are time snapshots at 1, 3 and 5 ps of the simulations of Au_3 and C_{60} bombardment of a 25 Å ice film on Ag. The simulations clearly show that in 1 to 3 ps after the projectile impact, most of the water molecules near the impact point have been removed from the Ag substrate for both projectiles. This configuration opens an unimpeded ejection pathway for Ag atoms that have acquired sufficient kinetic energy from the incident projectile to eject. Similar behavior is observed for the Au and Au_2 simulations (data not shown).

Hence, the experimental value of λ is a direct measure of the ability of the overlayer ice film to absorb the incident ion energy. In effect, it is the characteristic depth of projectile energy loss and provides a measure of the relative depth of origin of Ag atoms from within this specific multilayer structure.

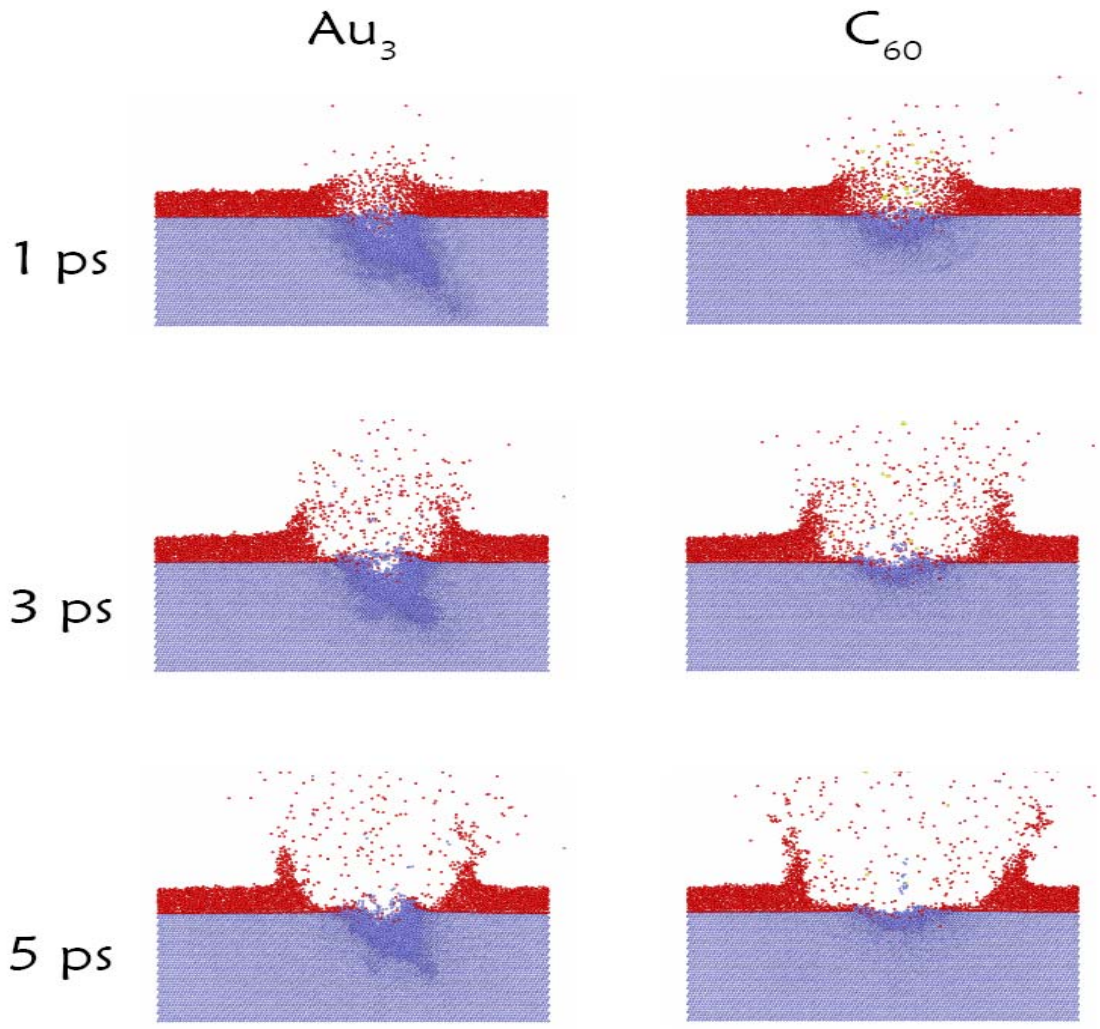

Figure **6-3**: Snapshots of the atom positions for Au_3 and C_{60} bombardment of a 25 Å ice film (red atoms) on Ag (blue atoms). The incident particle impinges from the left with 15 keV of energy at an angle of 40º with respect to the surface normal. The time snapshots are at 1, 3, and 5 ps for the frames from top to bottom, respectively.

These results are consistent with MD simulations of C_{60} and Au_3 bombardment at 5 keV of a bulk water ice substrate.[28] Within the first ps, both projectiles deposit all of their kinetic energy into the top 40 Å and top 100 Å, respectively. In both cases, crater formation and ejection of material from within the crater are predicted. Similarly, MD simulations of 15 keV Ga and C_{60} bombardment of three layers of benzene on Ag result in nearly complete removal of benzene molecules from the Ag surface near the point of impact.[29] However, as reported in Table **6-1**, additional simulations show that C_{60} deposits 97% of its incident energy in the 25 Å water ice overlayer, while Au_3 deposits just 49%, Au_2 – 32%, and Au – 31%. These values further illustrate the surface sensitivity of the water ice/Ag system when interrogated by each of the four projectiles as shown in Figure **6-2**. From Figure **6-3** and Table **6-1**, it is clear that the water ice film is most effective at stopping the C_{60} projectile and there is little displacement of Ag atoms in the Ag substrate relative to the Au_x projectiles. The C_{60} cluster, with the lowest energy per particle and the best mass match with the water ice molecules, most efficiently loses its energy in the overlayer, as is shown by the results in Figure **6-2** and Table **6-1**.

The observation of metal atoms ejecting in the presence of a thick organic layer is not unprecedented.[30] Bolbach *et al*. deposited Cd stearate Langmuir-Blodgett layers on Au and Ag substrates and measured the substrate ion signal due to 21 keV Cs^+ bombardment as a function of coverage.[31] They found that there is a measurable Ag^+ ion signal to 8 layers or about 200 Å. Wong *et al*. measured the emission of Au^-, Au_2^- and Au_3^- from thiolate layers adsorbed on a Au substrate due to 25 keV Ga^+ bombardment.[32] For the Au^- emission, they find a depth of origin of 70 Å and see emission of all three ions up to a depth of 10 layers or 160 Å. These values are comparable to those found in

this study as shown in Figure **6-2**. Moreover, the mechanism presented here suggests that the metal ions are not ejecting through the organic overlayer but rather the overlayer is swept away providing an unimpeded path for ejection.

This picture of cluster bombardment provides insight into related phenomena. Experimentally, it is possible to determine the number of water molecule equivalents that are desorbed from a thick film of water ice per incident projectile, Y_{eq}, as described in section **6.2**. Water ice films of 150 nm thickness are deposited on the Ag surface, and each projectile is used to controllably erode the overlayer material. Resulting profiles are displayed in Figure **6-4**.

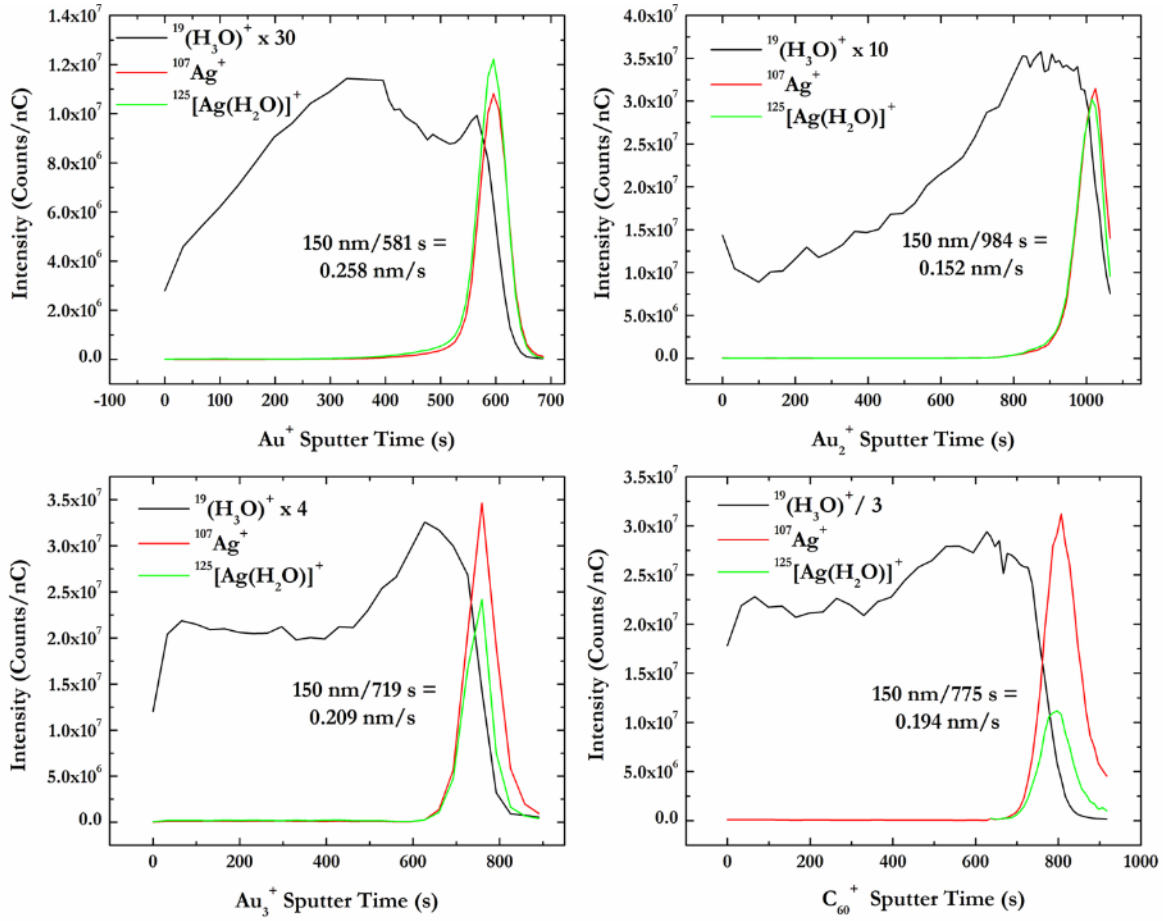

Figure **6-4**: Representative depth profile plots through 150 nm of water ice film on a silver-coated, modified QCM assembly for the four primary projectiles being studied. a.) Au^+ profile, b.) Au_2^+ profile, c.) Au_3^+ profile, and d.) C_{60}^+ profile. Sputter times to reveal 50 % of the ^{107}Ag signal intensity for each primary projectile, as well as the corresponding sputter rates, are shown for clarification.

Sputter rates are measured in terms of the time needed to sputter through the overlayer ice films, with the ice/silver interface determined to be the point at which the Ag signal reaches half of its maximum value. The sputter rates are converted to water ice yields using the following relationship:

$$Y_{H_2O} = \frac{S_R A \rho}{I_\rho} \qquad (1)$$

where S_R is the sputter rate (cm/s), A is the sputtered area of the sample (cm^2), ρ is the molecular density of water ice (3.075×10^{22} molecules/cm^3), and I_p is the number of primary ions per second irradiating the sample .

An examination of the representative profile data in Figure **6-4** reveals that all projectiles studied can erode through the water ice overlayer to reach the ice/silver interface. Additionally, the ^{107}Ag signals are approximately equal for all projectiles after being normalized to primary ion current (counts/nC). However, the ratio of water ice signal to Ag signal is highest for C_{60}^+, followed by $Au_3^+ > Au_2^+ > Au^+$. The ratio of the Ag water cluster at m/z 125 over the ^{107}Ag signal follows the inverse trend, which may indicate that the atomic projectiles, with their larger proportion of incident energy being deposited into the substrate, are embedding H_2O molecules into the silver. When the interface is probed, the larger concentration of water molecules within the sub-surface region of the silver substrate may lead to more efficient recombination with silver atoms to form the Ag-H_2O cluster.

Water ice signals are highest at the substrate interface due to the well-known SIMS matrix effect, where surface adsorbates increase the ionization efficiency of species within the interface region. This same effect is illustrated with the rise and fall of the silver species signals in the depth profiles. The projectiles erode away the material near the interface, and the ionization efficiency of the silver decreases to a steady state value in the bulk of the material.

The water ice yields that are calculated from the sputter rates in the profile plots are reported in Table **6-1** for a range of projectile energies. It is observed that the yields span two orders of magnitude for the projectiles studied, with the cluster ions of Au_3 and

C_{60} sputtering much more material than Au_2 and Au – data that are consistent with the water ice intensities in the depth profile plots in Figure **6-4**. A more detailed examination reveals that the water ice yields for C_{60} bombardment are linear to 80 keV, with a slight deviation from linearity for the 120 keV projectile. A similar trend is exemplified for Au_3 bombardment, where water ice yields increase linearly to 20 keV, with a slight deviation from linearity for the 25 keV projectile. The linearity of the increased yields for the cluster projectiles with respect to incident energy is expected.[33,34]

The effect of projectile charge seems to be negligible as the isoenergetic projectiles 20 keV C_{60}^{++} and 40 keV C_{60}^{+} give water ice yields that are similar within 10 %. Other internal studies in this laboratory indicate for other systems that the yields can actually be higher for the doubly charged species at equal energy, which indicates that the discrepancy between the values in Table **6-1** is most likely within statistical error.

A comparison of the data in Table **6-1** reveals an inverse relationship between Y_{eq} and λ and a direct relationship between Y_{eq} and energy loss of the projectile. When the energy loss to the overlayer is highest, Y_{eq} is also highest. Hence, the C_{60} beam is most sensitive for removing material closest to the surface while also removing the most total material. Mass spectra for the four projectiles in Figure **6-5** and Figure **6-6** for 10 Å and 20 Å of water ice film on Ag, respectively, are shown to illustrate this surface sensitivity.

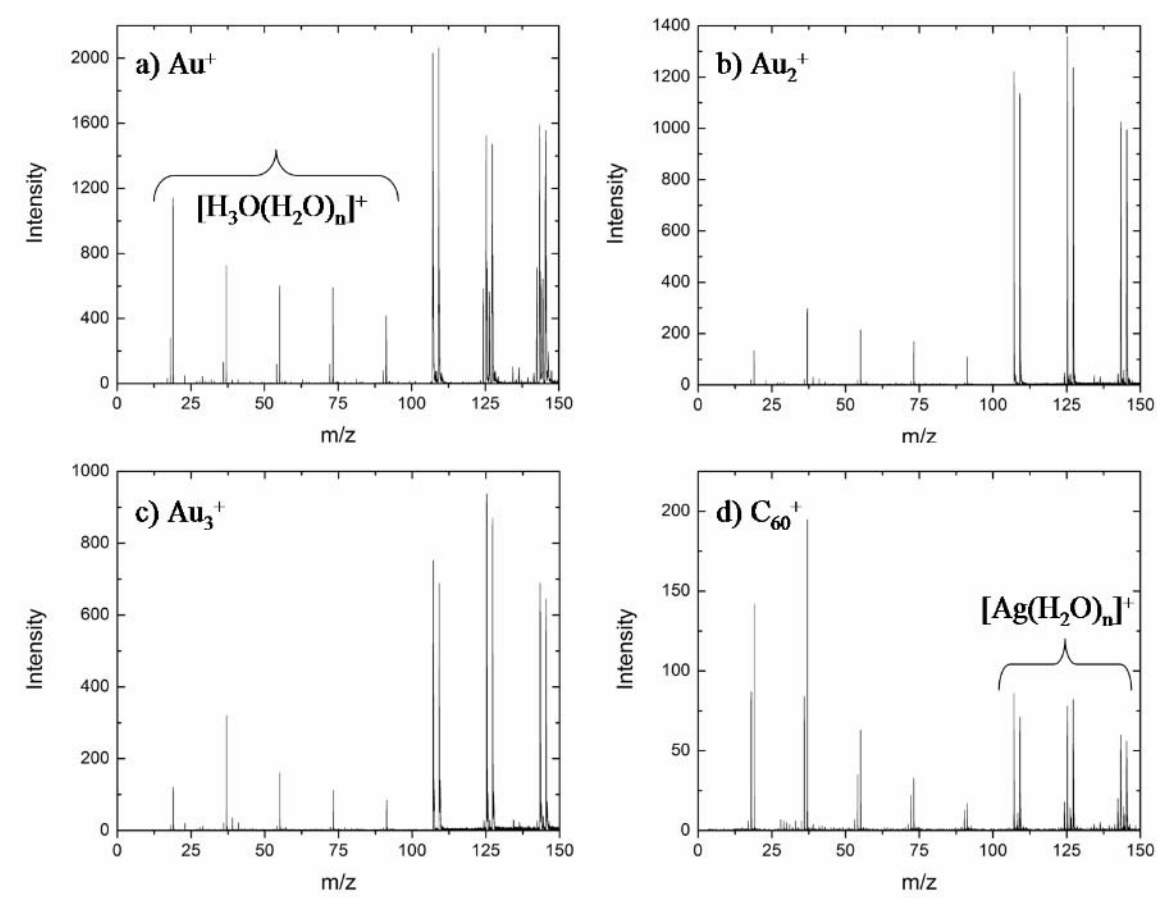

Figure **6-5**: Spectra of water ice film and underlying sputter-cleaned silver at 10 Å of ice thickness, for all four primary projectiles being studied: a.) Au^+, b.) Au_2^+, c.) Au_3^+, and d.) C_{60}^+. Raw integrated peak intensity values were plotted against the m/z axis. Regions of water clusters and Ag-water clusters are identified.

The spectra clearly show differences for the projectiles studied. With 10 Å of water ice deposited on Ag, signals of species related to silver dominate the mass spectra acquired using Au^+, Au_2^+, and Au_3^+ projectiles. The spectrum recorded with C_{60}^+, however, shows water ice signals that already dominate the spectrum, despite such a small layer of deposited ice. With 20 Å of deposited water ice, the spectra acquired using Au^+ and Au_2^+ primary ions are almost unchanged. However, the water ice signals in the spectrum recorded with Au_3^+ are approaching equal intensity with those signals related to

silver. In the spectrum acquired by C_{60}^{+} primary ions, the spectrum is close to resembling a pure water ice spectrum, with small amounts of silver species being detected. These spectra, along with the data presented for characteristic depths of primary energy loss, water ice yields, and MD simulations, support the notion that cluster ions are more surface-sensitive than atomic projectiles. In addition, it is possible to tune the surface sensitivity to a desired value by selecting a particular projectile.

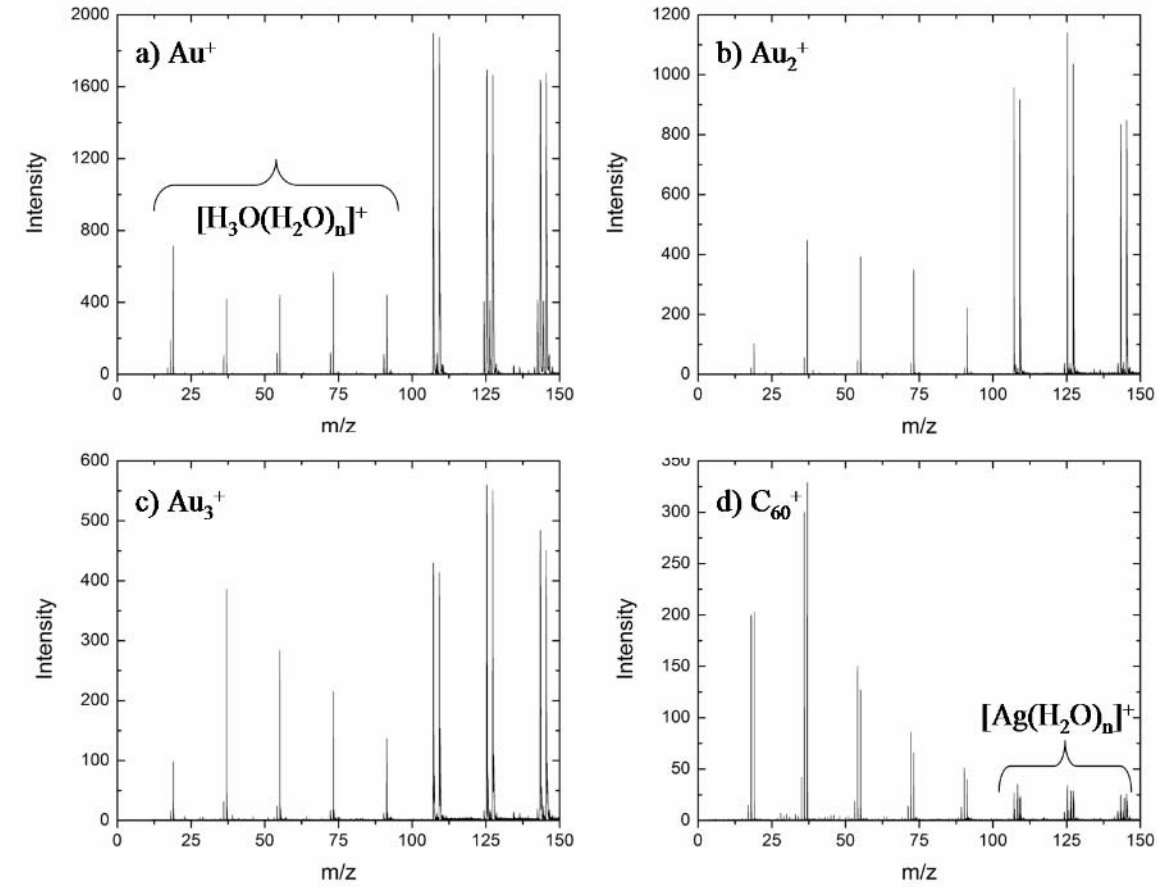

Figure **6-6**: Spectra of water ice film and underlying sputter-cleaned silver at 20 Å of ice thickness, for all four primary projectiles being studied: a.) Au^{+}, b.) Au_2^{+}, c.) Au_3^{+}, and d.) C_{60}^{+}. Raw integrated peak intensity values were plotted against the m/z axis. Regions of water clusters and Ag-water clusters are identified.

With the data presented here, it is not surprising that a projectile such as C_{60} provides depth resolution of a few nm during depth profiling of metal multilayer structures. Moreover, since the energy confinement of the cluster ions also applies to weakly bound molecular systems, it is reasonable to expect there will be little damage accumulation during bombardment and that residual damage will be removed during the impact event. Hence, the observation that molecular depth profiling is feasible with cluster sources, but not atomic projectiles, seems reasonable. The water ice/silver system may be contrasted with a strongly bound material such as a clean Ag crystal. For cluster bombardment, the crater formation process appears to be quite similar to that found for water ice, with Ag atoms ejecting from layers extending to near the bottom of the crater, or about 2 nm.[5] For atomic bombardment, a crater is not generally formed for target materials with higher binding energies like Ag, thereby restricting the depth of origin of sputtered atoms essentially to the first layer.

6.4 Conclusions

This work shows from a combined experimental and theoretical study that when cluster projectiles are employed for surface analysis, particularly when studying weakly bound overlayers, the characteristic depths of projectile energy loss are smaller than for their atomic counterparts, resulting in higher yields of the overlayer material and a higher surface sensitivity. Specifically, C_{60} exhibits the highest yields and lowest characteristic depth of primary projectile energy loss, making it most effective for maintaining adequate depth resolution during depth profiling of multilayer systems. Moreover, we

find that substrate particles eject from a previously unreported mechanism whereby the overlayer is swept away, providing an easy escape route for the substrate particles. This mechanism is in sharp contrast to a mechanism in which the ejected substrate particles would have to travel through the overlayer through a series of collisions that ultimately lead to desorption.

6.5 References

1. Applehans, A.D., Delmore, J.E., *Anal. Chem.*, **1989**, *61*, 1087.

2. Davies, N., Weibel, D.E., Blenkinsopp, P., Lockyer, N., Hill, R., Vickerman, J.C., *Appl. Surf. Sci.*, **2003**, *203*, 223.

3. Wong, S.C.C., Hill, R., Blenkinsopp, P., Lockyer, N.P., Weibel, D.E., Vickerman, J.C., *Appl. Surf. Sci.*, **2003**, *203-204*, 219.

4. Takeuchi, D., Seki, T., Aoki, T., Matsuo, J., Yamada, I., *Mater. Chem. Phys.*, **1998**, *54*, 76.

5. Postawa, Z., Czerwinski, B., Szewczyk, M., Smiley, E.J., Winograd, N., Garrison, B.J., *J. Phys. Chem. B*, **2004**, *108*, 7831.

6. Weibel, D., Wong, S., Lockyer, N., Blenkinsopp, P., Hill, R., Vickerman, J.C., *Anal. Chem.*, **2003**, *75*, 1754.

7. Weibel, D.E., Locker, N., Vickerman, J.C., *Appl. Surf. Sci.*, **2004**, *231-232*, 146.

8. Insepov, Z., Yamada, I., Sosnowski, M., *Mater. Chem. Phys.*, **1998**, *54*, 234.

9. Binns, C., *Surf. Sci. Rep.*, **2001**, *44*, 1.

10. Jensen, P., *Rev. Mod. Phys.*, **1998**, *71*, 1695.

11. Sun, S., Wucher, A., Szakal, C., Winograd, N., *Appl. Phys. Lett.*, **2004**, *84*, 5177.

12. Wucher, A., Sun, S., Szakal, C., Winograd, N., *Anal. Chem.*, **2004**, *76*, 7234.

13. Szakal, C., Sun, S., Wucher, A., Winograd, N., *Appl. Surf. Sci.*, **2004**, *231-232*, 183.

14. Mahoney, C.M., Roberson, S.V., Gillen, G., *Anal. Chem.*, **2004**, *76*, 3199.

15. Wagner, M.S., *Anal. Chem.*, **2005**, *77*, 911.

16. Xu, J.Y., Szakal, C.W., Martin, S.E., Peterson, B.R., Wucher, A., Winograd, N., *J. Am. Chem. Soc.*, **2004**, *126*, 3902.

17. Ostrowski, S.G., Szakal, C., Kozole, J., Roddy, T.P., Xu, J.Y., Ewing, A.G., Winograd, N., *Anal. Chem.*, **2005**, *77*, 6190.

18. Monroe, E.B., Jurchen, J.C., Lee, J., Rubakhin, S.S., Sweedler, J.V., *J. Am. Chem. Soc.*, **2005**, *127*, 12152.

19. Touboul, D., Kollmer, F., Niehuis, E., Brunelle, A., Laprevote, O., *J. Am. Soc. Mass Spectrom.*, **2005**, *16*, 1608.

20. Christiansen, J.W., Delli Carpini, D., Tsong, I.S.T., *Nucl. Instrum. Meth.*, **1986**, 218.

21. Fraser, H.J., Collings, M.P., McCoustra, M.R.S., *Rev. Sci. Instrum.*, **2002**, *73*, 2161.

22. Braun, R.M., Blenkinsopp, P., Mullock, S.J., Corlett, C., Willey, K.F., Vickerman, J.C., Winograd, N., *Rapid Commun. Mass Spectrom.*, **1998**, *12*, 1246.

23. Garrison, B.J., in *ToF-SIMS: Surface Analysis by Mass Spectrometry*, Vickerman, J.C., Briggs, D., eds.; Surface Spectra, Ltd. and IM Publications: Manchester, U.K., **2001**, p. 223.

24. Dou, Y.S., Zhigilei, L.V., Winograd, N., Garrison, B.J., *J. Phys. Chem. A*, **2001**, *105*, 2748.

25. Izvekov, S., Voth, G.A., *J. Chem. Phys.*, **2001**, *115*, 7196.

26. Foiles, S.M., Baskes, M.I., Daw, M.S., *Phys. Rev. B*, **1986**, *33*, 7983.

27. Brenner, D.W., Shenderova, O.A., Harrison, J.A., Stuart, S.J., Ni, B., Sinnott, S.B., *J. Phys. Condens. Matter*, **2002**, *14*, 783.

28. Russo, Jr., M.F., Wojciechowski, I.A., Garrison, B.J., *Appl. Surf. Sci.*, **2006**, *252*, 6423.

29. Postawa, Z., Czerwinski, B., Wiongrad, N., Garrison, B.J., *J. Phys. Chem. B*, **2005**, *109*, 11973.

30. Delorte, A., in *ToF-SIMS: Surface Analysis by Mass Spectrometry*, Vickerman, J.C., Briggs, D., eds.; Surface Spectra, Ltd. and IM Publications: Manchester, U.K., **2001**, p. 161.

31. Bolbach, G., Beavis, R., Della-Negra, S., Deprun, C., Ens, W., Le Beyec, Y., Main, D.E., Schueler, B., Standing, K.G., *Nucl. Instrum. Meth. Phys. Res.*, **1988**, *30*, 74.

32. Wong, S.C.C., Lockyer, N.P., Vickerman, J.C., *Surf. Interf. Anal.*, **2005**, *37*, 721.

33. Andersen, H.H., Brunelle, A., Della-Negra, S., Depauw, J., Jacquet, D., Le Beyec, Y., *Phys. Rev. Lett.*, **1998**, *80*, 5433.

34. Bouneau, S., Brunelle, A., Della-Negra, S., Depauw, J., Jacquet, D., Le Beyec, Y., Pautrat, M., Fallavier, M., Poizat, J.C., Andersen, H.H., *Phys. Rev. B*, **2002**, *65*, 144106.

Chapter 7

Application of the Buckminsterfullerene Projectile to SIMS Imaging

This chapter is adapted from: Xu, J., Ostrowski, S.G., Szakal, C, Ewing, A.G., Winograd, N., *Appl. Surf. Sci.*, **2004**, *231-232*, 159, with permission. Copyright is retained by Elsevier, B.V.; and Ostrowski, S.G., Szakal, C., Kozole, J., Roddy, T.P., Xu, J., Ewing, A.G., Winograd, N., *Anal. Chem.,* **2005**, *77*, 6190, with permission. Copyright is retained by the American Chemical Society.

7.1 Introduction

Earlier chapters make reference to the potential gains for SIMS imaging that appear possible when employing a C_{60}^+ projectile instead of an atomic projectile. Specifically, the ability of biological molecules such as histamine to retain strong secondary ion signals after prolonged C_{60}^+ bombardment and the high sputter yields as noted for water ice are indicative that improved biological SIMS experiments are possible. Despite the fact that atomic probes may be focused to a smaller probe size, effective lateral resolution can be better with cluster sources because of high signal contrast in adjacent pixels. Because of these properties, the SIMS community is rapidly moving towards widespread implementation of cluster projectiles.

A cell model system consisting of a sucrose-doped "cytoplasm" and a phospolipid "membrane" enclosure is reported elsewhere by Kozole, Szakal, and coworkers.[1] The

authors describe the ability of 20 keV C_{60}^+ ions to controllably erode through the outer lipid layer and probe the encapsulated sucrose signal without damage accumulation of either molecule. The work represents an important step in the prospects of cluster sources being used for biological SIMS experiments.

This work builds on the information learned in the previous study and examines the preliminary biological imaging capabilities of a 20 keV C_{60}^+ projectile for two different types of systems: lipid films in picoliter-volume vials, and individual freeze-dried *Tetrahymena* and *Spirostomum* cells. In each case, strong enhancements are observed in the secondary ion signals, resulting in improved lateral resolution in comparison to that following bombardment by In^+ and Au^+. Based on this preliminary work, it appears feasible to use cluster ion sources for biological SIMS imaging.

7.2 Lipid Films in Picoliter Vials

7.2.1 Lipid Films in Picoliter Vials Background

Lipid heterogeneity in cellular membranes is thought to provide the basis for several intercellular and intracellular events that need further understanding, including exocytosis. Chemical imaging of lipids within cellular membranes can yield insight into the mechanisms responsible for biological functions. Fluorescence imaging is often employed to monitor lipid heterogeneity,[2-4] but lacks the chemical specificity to go along with its high spatial resolution. Recently, ToF-SIMS using an In^+ primary ion source has been used to image the lipid heterogeneity in mating *Tetrahymena*, where the

phosphatidylcholine (PC) headgroup signal is shown to decrease at the mating junction.[5] Concurrently, an increase of highly curved lipids is expected at the mating region, but enhanced signals are needed to assign the presence of non-PC lipids.

This work focuses on attaining control imaging data for four different lipids relevant to SIMS analysis of cellular membranes. In collaboration with Dr. Sara Ostrowski, the lipids are imaged while contained in picoliter-volume vials and secondary ion enhancements stemming from C_{60}^+ bombardment relative to In^+ are reported.

7.2.2 Lipid Films in Picoliter Vials Experimental

The BioTof time-of-flight secondary ion mass spectrometer used for these imaging experiments is described elsewhere.[6] Primary ions of 15 keV In^+ and 20 keV C_{60}^+ ions are employed for imaging, with the In^+ ions being formed in a liquid metal ion gun (FEI, Beaverton, OR) installed on a Kratos Prism ToF-SIMS instrument (Manchester, UK). *Note: Images created by In^+ bombardment were acquired by Dr. Sara Ostrowski*. The atomic source is focused to sub-μm probe sizes, while the C_{60}^+ ions formed in the source described in Chapter 2 are focused to about 10 to 20 μm.

Details of this experiment are described elsewhere.[7] Briefly, a nanofabricated picoliter vial array[8] in silicon was used as the substrate for four different lipids, whose structures are depicted in Figure **7-1**. The lipids phosphatidylcholine (PC), phosphatidylglycerol (PG), sulfatide, and cholesterol were added one at a time into adjacent picoliter vials using a General Valve Picospritzer equipped with a microliter syringe.

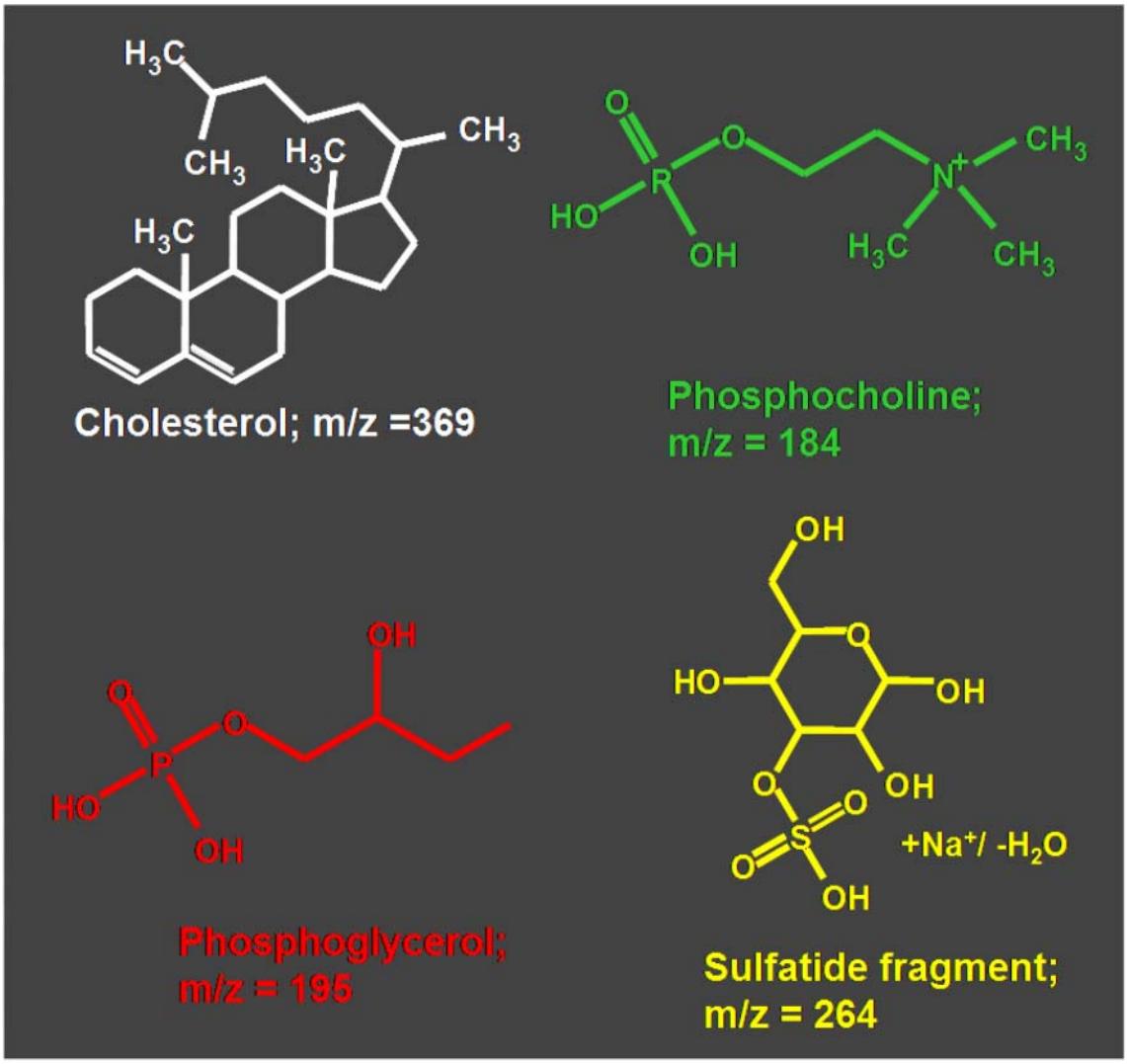

Figure **7-1**: Structures and positive ion target spectral masses for the lipids injected into picoliter vials. Structures are color-coded to the molecule-specific positive ion SIMS images.

7.2.3 Lipid Films in Picoliter Vials Results and Discussion

Molecule-specific images for the four lipids studied using In^+ and C_{60}^+ primary ions are shown in Figure **7-2**. The image created by In^+ projectiles shows excellent lateral resolution of the vials themselves, with little signal of the individual lipids being detected. The image created with C_{60}^+ primary ions exhibits poorer lateral resolution of the substrate topography, but clearly desorbs more lipid material for each analyte studied. A signal increase between one and three orders of magnitude is observed for the various lipids when using C_{60}^+, which translates well for the prospects of detecting these molecules in biological cells with improved sensitivity over past endeavors.

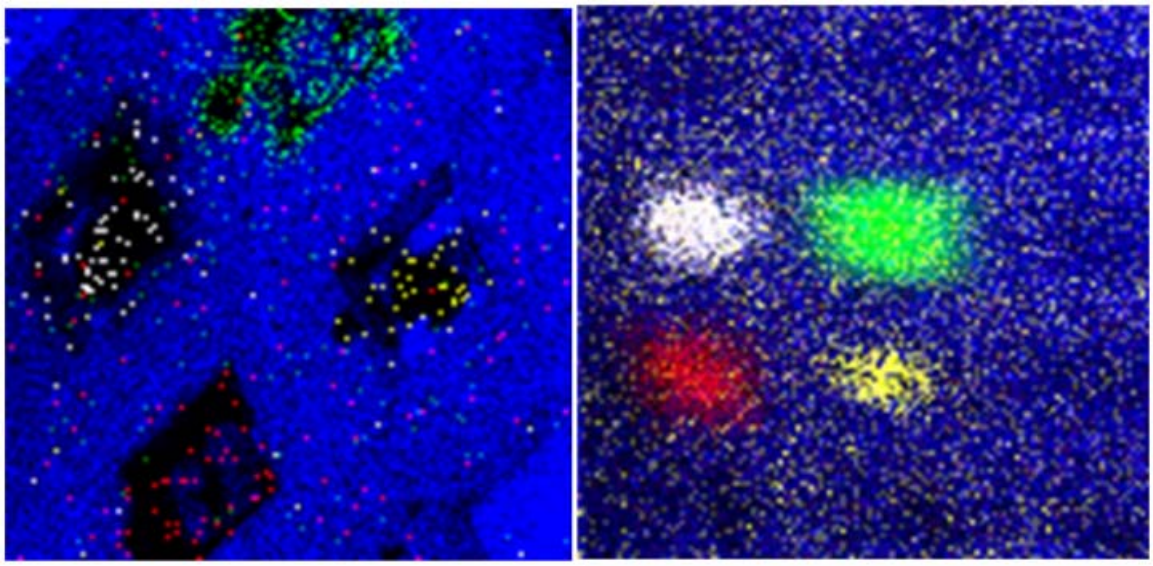

Figure **7-2**: Molecule-specific positive ion SIMS images of the four lipids studied in picoliter vials for the primary ions: In^+ (left, 256 x 256 pixels at 300 μm^2 area, 64 pulses/pixel), and C_{60}^+ (right, 128 x 128 pixels at 1,000 μm^2 area, 64 pulses/pixel). Silicon ions at m/z 28 are represented in blue, cholesterol at m/z 369 in white, PC headgroup at m/z 184 in green, PG at m/z 195 in red, and sulfatide at m/z 264 in yellow. Note that the incidence angles of the instruments were different, resulting in what looks like an out-of-plane image on the left. *The In^+ image was acquired by Dr. Sara Ostrowski*.

7.3 Single Cell Imaging

7.3.1 Single Cell Imaging Background

Atomic ion sources have been employed for single cell imaging in this lab and others over the past decade.[9-12] However, sensitivity to biomolecules has been problematic, whether the cells are prepared by freeze-fracture or by freeze-drying. Elemental species such as sodium and potassium are easily detected from the cells and surrounding environments, but molecular spectral signal intensities decrease with increasing mass. The signal of the phosphocholine (PC) lipid headgroup is often the only biomolecule detected in or around the cells with atomic ion sources, and there is a clear need for increased signal of this molecule, as well as the ability to detect other biomolecules - many of which are in lower concentrations than PC in cells. If cluster sources can provide signal enhancements, better effective lateral resolution, and offer detection of other molecules besides PC, then the employment of SIMS to studying small molecules in cells such as neurotransmitters can ensue – perhaps leading to imaging single cell events such as exocytosis. The *Tetrahymena* image induced by C_{60}^+ bombardment is the first image of a biological cell using 20 keV buckminsterfullerene and the *Spirostomum* cell images are from the first attempted depth profiling studies of a single cell using C_{60}^+ primary ions.

7.3.2 Single Cell Imaging Experimental

The BioTof and Kratos instruments employed in the previous section and mentioned in **7.2.2** are both used for imaging single cells. Primary ions of 15 keV In^+, 15 keV Au^+, and 20 keV C_{60}^+ ions are employed for cell imaging, with the In^+ ions being formed in the Kratos instrument as described earlier and the Au^+ and C_{60}^+ ions being formed in two different BioTof instruments. *Note: Images created by In^+ bombardment were acquired by Dr. Sara Ostrowski and the image created by Au^+ bombardment was acquired by Dr. Brendan Haynie.*

For *Tetrahymena* and *Spirostomum* cells, samples are prepared by rapid freezing of the cells in liquid propane/ethane, followed by a slow freeze drying in ultrahigh vacuum while the samples were attached to a cryogenically cooled sample arm. The same samples are used for comparing images in each of the instruments, and when possible, the same cells are imaged using multiple ion beams. All images were acquired using less than 1 x 10^{12} ions/cm^2 primary ion fluences so as to avoid sample damage. Samples are analyzed with In^+ ions first, followed by C_{60}^+ projectiles, and lastly Au^+ ions (when applicable). Specifics of each image are given in the image captions.

7.3.3 Single Cell Imaging Results and Discussion

Freeze-dried *Tetrahymena* cells are imaged by In^+, Au^+, and C_{60}^+ projectiles, with comparisons provided in Figure **7-3**. Here, molecule-specific images of the outer membrane lipid headgroup of phosphocholine (PC) at m/z 184 are shown for each projectile. In all cases, more than one cell is within the 500 μm analysis area. It is clear

that higher signals of the PC lipid head group are detected when C_{60}^+ projectiles are employed instead of the traditionally used atomic projectiles. The C_{60}^+ ion current is about an order of magnitude less than that of the atomic sources, making the overall signal enhancement per pixel at least two orders of magnitude higher. With information from earlier chapters, this improvement is most likely due to large increases in sputter yields of the biological molecules, especially when immobilized on "softer" targets such as cellular materials, although increases in ionization yield may also be contributing to the enhancement. The ionization efficiency may also be affected by the presence of frozen water ice, where protons are formed following cluster ion bombardment.[13]

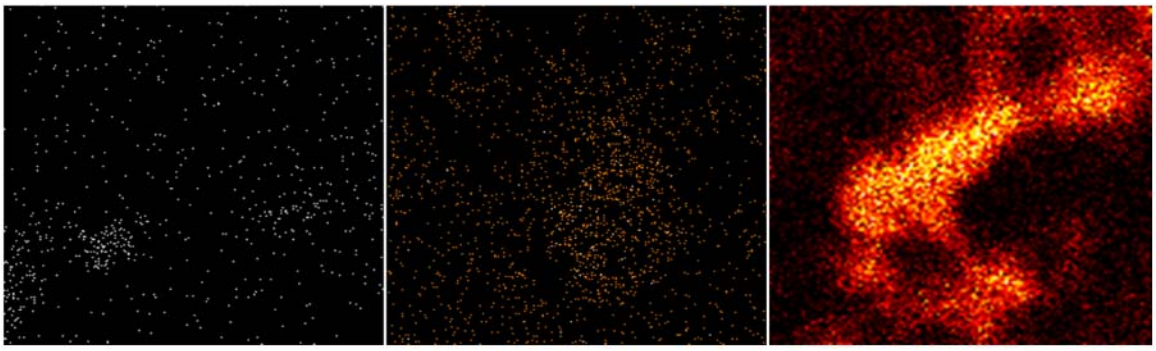

Figure **7-3**: SIMS positive ion molecule-specific images at 500 μm^2 of the outer membrane lipid headgroup phosphocholine (PC) at m/z 184 in *Tetrahymena* cells for bombardment by the primary ions: 15 keV Au^+ (left, 10 pulses/pixel), 15 keV In^+ (middle, 16 pulses/pixel), and 20 keV C_{60}^+ (right, 15 pulses/pixel). All images are 128 x 128 pixels. *The Au^+ image was acquired by Dr. Brendan Haynie and the In^+ image was acquired by Dr. Sara Ostrowski.*

At this preliminary stage, no other biologically relevant molecules besides PC are found that localize to the cells, even for the high signals generated by C_{60}^+ bombardment. Whether this result is due to a sample preparation issue or low concentrations of other analytes is unclear. However, it is believed that since such low ion fluences are used for

these images, information from beneath the surface and into the bulk of the cell where the majority of biomolecules reside is not probed. Discussions in previous chapters suggest the possibilities of depth profiling into and even through cells because of the high surface sensitivities of cluster ions, reduced beam-induced accumulation of chemical damage and interlayer mixing, and the high yields needed to sputter material faster than damage can accumulate.

To acquire better-defined images, and to ease the process of locating a target cell in different instruments, cells with larger size are utilized. *Spirostomum* cells grow to over 1 mm in length, as pictured in an optical image in Figure **7-4**. These cells are known for their ability to shrink to ¼ their size in just a few milliseconds, faster than any other single-celled organism, when they are under a type of stress.

Figure **7-4**: Optical image of two *Spirostomum* cells.

The first approach with these cells is to duplicate the type of experiment performed with the *Tetrahymena*. As is shown in Figure **7-5**, the total ion images of a single *Spirostomum* cell are strikingly different when acquired using In^+ and C_{60}^+ bombardment. The In^+-induced image appears to exhibit higher lateral resolution. This advantage is somewhat misleading, however, since the image resulting from C_{60}^+ bombardment exhibits much higher overall intensity of all ions throughout the spectrum, giving higher signals at each pixel. A look at the molecule-specific images, illustrates the power of the large cluster source to provide high-quality biological SIMS images. Image overlays of the Cu substrate signal at m/z 63 and the PC headgroup at m/z 184 are shown in Figure **7-6**. The outer membrane signal is considerably stronger for the C_{60}^+-induced image compared to that obtained by In^+. In the C_{60}^+ image, three *Paramecia* also appear in the imaging area, showing that the C_{60}^+ can resolve smaller cells on the order of 40 to 50 μm as well.

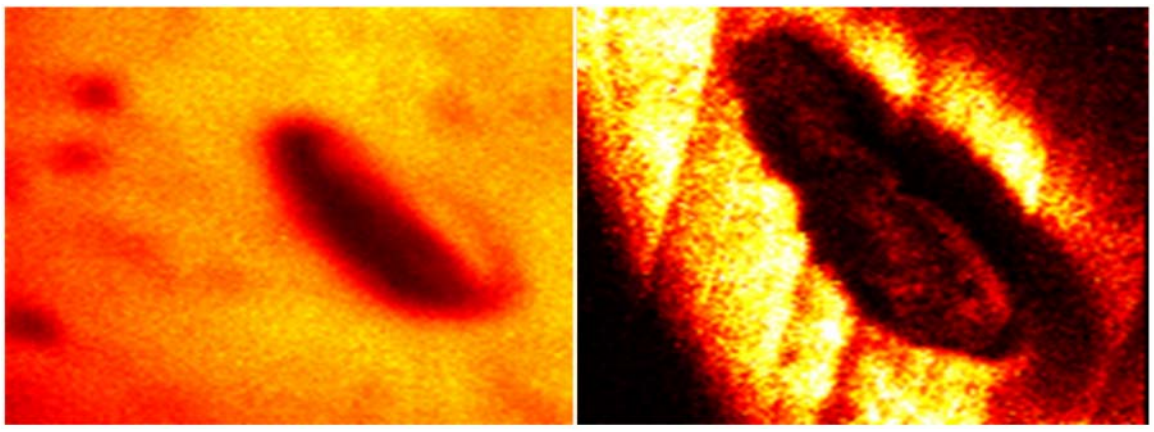

Figure **7-5**: SIMS positive total ion images of a *Spirostomum* cell on a copper substrate for the primary ions: 20 keV C_{60}^+ (left, 700 μm^2, 128 x 128 pixels, 60 pulses/pixel), and 15 keV In^+ (right, 384 μm^2, 128 x 128 pixels, 71 pulses/pixel). *The In^+ image was acquired by Dr. Sara Ostrowski.*

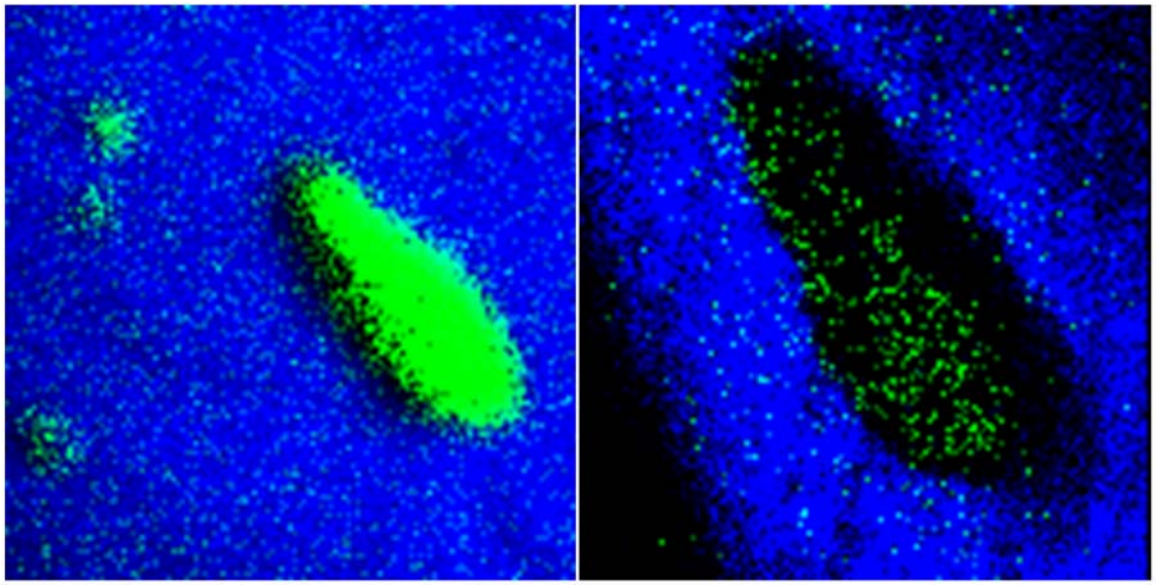

Figure **7-6**: SIMS positive ion molecule-specific images of a *Spirostomum* cell on a copper substrate for the primary ions: 20 keV C_{60}^+ (left, 700 μm^2, 128 x 128 pixels, 60 pulses/pixel), and 15 keV In^+ (right, 384 μm^2, 128 x 128 pixels, 71 pulses/pixel). Blue represents copper signal at m/z 63 and green represents the PC headgroup at m/z 184. Also visible in the C_{60}^+ image are three *Paramecia* that were present in this particular sample. *The In^+ image was acquired by Dr. Sara Ostrowski.* These images are published elsewhere[14] and are duplicated with permission. Copyright is retained by the American Chemical Society.

To explore the depth profiling prospects of cluster sources for biological cells, a dc C_{60}^+ ion fluence of 1.2 x 10^{12} ions/cm^2 is irradiated onto the sample. Positive SIMS molecule-specific images before and after sputtering are displayed in Figure **7-7** for the PC headgroup at m/z 184, sodium at m/z 23, and potassium at m/z 39. The fluence is sufficient to remove the cell membrane material and expose the inner portion of the *Spirostomum*. Potassium signal is displayed from within the cell after sputtering while sodium is present only in the areas surrounding the cell – both observations being indicative of natural inorganic ion distributions. Although these localizations appear visible before sputtering as well, the effect after sputtering seems to be more pronounced.

This preliminary depth profiling experiment shows promise for being able to probe the chemistry beyond the lipid membrane and from within the cytoplasm. However, more research is needed to identify the reasons for low organic secondary ion signals from within a cell after sputtering. Three phenomena that are being investigated as the cause of lost signals in cells after sputtering include, but are not limited to: 1) localized beam-induced sample charging on/in the cells, 2) lack of molecule ionization – especially with no water ice present to provide protons for $[M+H]^+$ detection, and 3) challenging concentrations of biological molecules inside of the cells that may be below the detection limits.

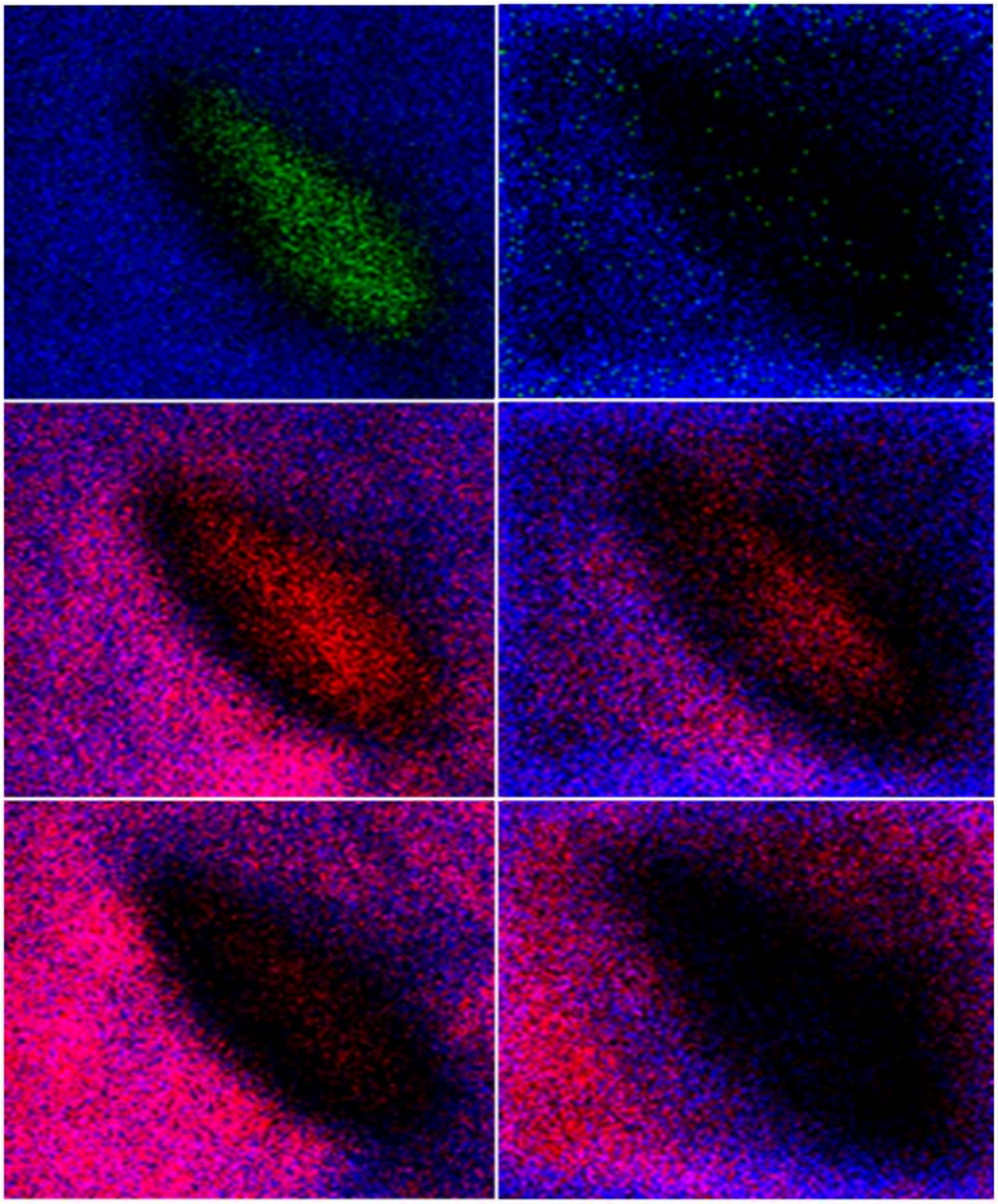

Figure **7-7**: SIMS positive ion molecule-specific image overlays at 300 μm^2 after 1.2 x 10^{12} fluence of 20 keV dc C_{60}^+. Left column is before sputtering and right column is after sputtering. Top row: Copper at m/z 63 in blue and PC headgroup at m/z 184 in green, Middle row: Copper in blue and potassium at m/z 39 in red, Bottom row: Copper in blue and sodium at m/z 23 in red. All images are 128 x 128 pixels and 20 pulses/pixel.

7.4 Conclusions

The secondary ion signals of lipid membrane molecules are enhanced by one to three orders of magnitude for C_{60}^+ projectiles relative to In^+ primary ions. These enhancements are manifested in the ability of SIMS images created by C_{60}^+ to provide better effective lateral resolution of single biological cells – owing to higher signal contrast in adjacent pixels. The preliminary experiments presented here represent a foundation for molecular depth profiling through cells and cellular materials, and also outline difficulties that must be overcome in future endeavors. However, no biologically relevant molecules have been probed beneath the cell membrane surface. Experiments are ongoing by others in this laboratory to obtain biomolecule signals after sputtering into cells.

7.5 References

1. Kozole, J., Szakal, C., Kurczy, M., Winograd, N., *Appl. Surf. Sci.*, **2006**, *252*, 6789.

2. Hao, M.M., Mukherjee, S., Maxfield, F.R., *Proc. Natl. Acad. Sci. U.S.A.*, **2001**, *98*, 13072.

3. Hwang, J., Gheber, L.A., Margoilis, L., Edidin, M., *Biophys. J.*, **1998**, *74*, 2184.

4. Forstner, M.B., Martin, D.S., Navar, A.M., Kas, J.A., *Langmuir*, **2003**, *19*, 4876.

5. Ostrowski, S.G., Van Bell, C.T., Winograd, N., Ewing, A.G., *Science*, **2004**, *305*, 71.

6. Braun, R.M., Blenkinsopp, P., Mullock, S.J., Corlett, C., Willey, K.F., Vickerman, J.C., Winograd, N., *Rapid Comm. Mass Spectrom.*, **1998**, *12*, 1246.

7. Ostrowski, S.G., Szakal, C., Kozole, J., Roddy, T.P., Xu, J., Ewing, A.G., Winograd, N., *Anal. Chem.*, **2005**, *77*, 6190.

8. Braun, R.M., Beyder, A., Xu, J.Y., Wood, M.C., Ewing, A.G., Winograd, N., *Anal. Chem.*, **1999**, *71*, 3318.

9. Roddy, T.M., Cannon Jr., D.M., Ostrowski, S.G., Winograd, N., Ewing, A.G., *Anal. Chem.*, **2002**, *74*, 4020.

10. Roddy, T.M., Ostrowski, S.G., Cannon Jr., D.M., Ewing, A.G., Winograd, N., *J. Amer. Soc. Mass Spectrom.*, **2002**, *13*, 1S.

11. Sjovall, P., Lausmaa, J., Nygren, H., Carlsson, L., Malmberg, P., *Anal. Chem.*., **2003**, *75*, 3429.

12. Parry, S., Winograd, N., *Anal. Chem.*, **2005**, *77*, 7950.

13. Conlan, X.A., Lockyer, N.P., Vickerman, J.C., *Rapid Commun. Mass Spectrom.*, **2006**, *20*, 1327.

14. Winograd, N., *Anal. Chem.*, **2005**, *77*, 142A.

Chapter 8

Conclusions and Future Directions

8.1 Instrumentation

In this dissertation, the implementation of a prototype 20 keV C_{60}^+ ion source (Ionotika, Ltd.) to a BioTof time-of-flight secondary ion mass spectrometer is described. Specifically, a detailed examination of the working principles and operational procedures of this ion source are provided, along with a comprehensive maintenance regimen. An emphasis is placed on the balance between the quality of SIMS data and the lifetime of ion source components. The guidelines presented here allow for the 20 keV C_{60}^+ ion source to operate for greater than 1000 hours, or at least six months, while providing high surface sputter rates and mass spectral signals.

8.2 Fundamentals

A prototype ion source comes with ambiguities regarding the types of characteristics that can be exploited for improving experiments. The bulk of the material in this dissertation is related to the characterization of the sputtering properties of the 20 keV C_{60}^+ ion source and to providing insight into the types of experiments best-suited for the C_{60}^+ projectile.

Results presented in this thesis work show that the large enhancements of secondary ion signals due to C_{60}^+ bombardment compared to atomic projectile

bombardment are due to substantial increases in the sputter yields of the target materials. These yields often are enhanced by two to three orders of magnitude when compared to traditionally employed primary ions such as Ga^+, In^+, and Au^+. The extraordinarily high sputter yields allow for any damaged molecules from a C_{60}^+ impact to be removed at a rate that is higher than the accumulation of such damage. Due to the combination of high sputter yields and minimal damage accumulation, the sample following C_{60}^+ impact is relatively void of topographic roughness, beam-induced interlayer mixing, and sub-surface molecular damage. These properties of the C_{60}^+ projectile can be exploited to controllably erode through layers of material in both inorganic and organic sample systems to provide a depth profile of chemical species within a sample.

Additional experiments demonstrate that a remarkably high percentage of incident C_{60}^+ energy is deposited within just a few layers of the surface. The result is a dense region of energy deposition that maximizes sputtering yield, leaves little energy to penetrate into the sub-surface material, and provides the highest mass spectral surface sensitivity of the projectiles studied. The radically different physical properties of cluster ion bombardment in relation to atomic ion bombardment lend to creating new applications for SIMS, including the prospects for three-dimensional chemical mapping of biological materials.

8.3 Application to SIMS Bioimaging

A model lipid system and two single-celled organisms are examined with the 20 keV C_{60}^+ ion source to evaluate the prospects of utilizing the unique properties of cluster

ion bombardment for imaging biological materials. Signal enhancements of relevant lipid molecules are large enough to increase effective SIMS lateral resolution compared to the more focused atomic ion beams by increasing signals in adjacent pixels. However, these imaging experiments are preliminary, and further study is needed to determine why signals of targeted biomolecules within the cells are currently low. Fundamental studies may concentrate on labeling different organelles within cells with dye molecules to aide in mass spectral interpretation. The concept of differential sputtering within cells can be examined by controllably sputter-eroding cellular material and acquiring atomic force microscope (AFM) images at pre-determined distances within the cell. The recent addition of a 40 keV C_{60}^{+} ion source should increase yields of biomolecules further while providing better lateral resolution due to its better beam focusing. Lastly, a concerted effort needs to be aimed at identifying biological systems where chemical heterogeneity at appropriate analyte concentrations can be studied using imaging cluster SIMS.

VITA

Christopher Wayne Szakal

Christopher Szakal, son of Wayne and Joan Szakal, was born in Scranton, PA, and raised in nearby Duryea, PA. A valedictorian of Pittston Area High School in 1997, he matriculated at Muhlenberg College in Allentown, PA, where he earned a Bachelor of Science degree in Chemistry and graduated Summa Cum Laude in 2001. He proceeded to The Pennsylvania State University in the summer of 2001 to conduct graduate research in the area of Analytical Chemistry with Professor Nicholas Winograd, and attained his Ph.D. in Chemistry in the fall of 2006.